

POLITECNICO DI TORINO

Master's degree in Civil Engineering

Master's Thesis

## Degradation of rockfall barriers



**Supervisor:**

Prof. Valerio De Biagi

**Co-Supervisor:**

Dott. Maddalena Marchelli

Ing. Francesco Pimpinella

**Student**

Marco Pizzolante

December 2025

# Index

<b>ABSTRACT .....</b>	<b>3</b>
<b>1 INTRODUCTION .....</b>	<b>4</b>
<b>2 ROCKFALL PHENOMENON: NATURE AND DAMAGE ANALYSIS.....</b>	<b>6</b>
2.1 DEFINITION OF FALLING ROCK PHENOMENA: FACTORS AND CLASSIFICATION .....	6
2.2 ROCKFALL RISK ANALISYS PROCEDURE .....	11
2.2.1 Identification of the danger .....	12
2.2.2 Scenario definitions .....	12
2.2.3 Propagation analysis and hazard evaluation .....	12
2.2.4 Evaluation of the elements at risk: value and vulnerability .....	14
2.3 RISK MITIGATION STRATEGIES.....	15
<b>3 ROCKFALL BARRIER.....</b>	<b>20</b>
3.1 COMPONENTS OF ROCKFALL BARRIERS .....	20
3.1.1 Net fences .....	21
3.1.2 Posts.....	23
3.1.3 Posts base system.....	23
3.1.4 Ropes anchorages .....	26
3.1.5 Energy dissipation devices.....	29
<b>4 ROCKFALL BARRIER DESIGN PROCEDURE.....</b>	<b>34</b>
4.1 DATA COLLECTION AND PRELIMINARY ANALYSIS .....	37
4.2 DESIGN AND DIMENSIONING CRITERIA: DIFFERENT STANDARD APPROACH.....	40
4.2.1 ONR 24810.....	40
4.2.2 Eurocode 7 .....	47
4.2.3 Design parameters for verification analysis.....	48
4.2.4 Performance evaluation of the product through real scale test: codified impact tests .....	51
4.2.5 CE marking.....	54
4.3 CONSIDERATION FOR EXTREMELY HIGH LOAD CASE .....	55
4.4 ROCKFALL SIMULATION WITH NUMERICAL SOFTWARE.....	57
<b>5 DEGRADATION OF ROCKFALL BARRIER .....</b>	<b>67</b>
5.1 CORROSIVITY OF ATMOSPHERE .....	69
5.1.1 Evaluation of corrosivity through corrosion rate of standard specimens.....	70
5.1.2 Corrosivity estimation based on environmental information: dose-response function.....	70
5.1.3 Estimation of the corrosivity category based on knowledge of the local environment situation.....	72
5.1.4 Corrosivity categories .....	73
5.2 CORROSION OF METAL AND ALLOYS .....	74
5.2.1 Environments effect.....	75
5.2.2 Corrosion test in artificial atmosphere.....	76
5.3 CORROSION OF ROCKFALL BARRIER COMPONENTS.....	79
5.3.1 Net corrosion and effects .....	79
5.3.2 Rope and rope anchor corrosion .....	80
5.3.3 Strength reduction due to corrosion.....	80
5.4 PROTECTION PROCEDURE: ZINC COATING .....	84
5.4.1 Zinc coating reduction due to environmental parameters .....	86

<b>6</b>	<b>STUDY CASES.....</b>	<b>91</b>
6.1	GEOGRAFICAL IDENTIFICATION OF THE CASE STUDY .....	91
6.2	PHOTOGRAFIC DOCUMENTATION.....	93
6.3	ENVIRONMENTAL CLASS OF THE STUDY CASES IN ACCORDANCE WITH ISO 9223:2012.....	97
6.3.1	Relative Humidity.....	98
6.3.2	Average temperature.....	100
6.3.3	SO <sub>2</sub> deposition .....	102
6.3.4	Cl <sup>-</sup> deposition.....	103
6.3.5	Corrosivity category computation .....	105
6.3.6	Maximum and minimum values of zinc corrosion: SO <sub>2</sub> statistical analysis.....	106
6.4	CORROSION RATE OF THE ZINC COATING WITH A LIFE PREDICTOR PROGRAM ....	108
6.5	DISCUSSION ON THE OBSERVED DEGRADATIONS .....	109
<b>7</b>	<b>CONCLUSION AND FINAL CONSIDERATIONS.....</b>	<b>116</b>
	<b>REFERENCES .....</b>	<b>118</b>

# ABSTRACT

Rockfall protection barriers play a crucial role in mitigating the risk associated with rockfall events in mountainous areas. However, their long-term performance can be significantly affected by material degradation due to environmental exposure, mechanical stress, and corrosion processes. This thesis investigates the degradation mechanisms that compromise the structural integrity and efficiency of rockfall barriers over time. A comprehensive review of existing studies and degradation models is provided, highlighting current limitations in predicting long-term behavior, in addition an overview on the principal's protection solution, zinc coatings, is presented. To support the analysis, a series of photographic real-world case study of safety devices are presented, aimed at illustrating the visible manifestations of material degradation. For each site, the environmental corrosivity class was identified in accordance with ISO 9223:2012 "Corrosion of metals and alloys - Corrosivity of atmospheres - Classification, determination and estimation". Based on this classification, the corrosion rate of the zinc coating was estimated to assess the expected material loss over time. The analysis provides valuable insight into the correlation between environmental exposure and the observed deterioration patterns, emphasizing the importance of considering site-specific atmospheric conditions in the durability assessment and maintenance planning of rockfall protection system.



# 1 INTRODUCTION

This thesis addresses the issue of corrosion and degradation affecting protection and prevention systems against landslides and rockfalls, with particular attention to the various processes impacting rockfall barriers across highly different territorial contexts. To support the discussion, a series of different cases are exposed, including inland and seaside highlighting the different corrosion processes that can affect the protection system. For a clearer understanding and identification of the problem, Chapter 2 provides general background information concerning the rockfall phenomenon.

The Italian territory exhibits a high degree of vulnerability to hydrogeological instability, resulting from the combined impact of natural and anthropogenic factors. Indeed, the young and unstable geomorphological conformation, coupled with extreme meteorological events and high population density, makes Italy particularly prone to landslides and floods.

As reported by the Chamber of Deputies on 5 July 2025 (Servizio Studi, 2025): “In the report containing the indication of the interventions under the responsibility of the Government Commissioners for the mitigation of hydrogeological risk and their implementation status as of 31 December 2023 (Doc. CCXXVIII, no. 2), it is highlighted that 93.9% of Italian municipalities (7,423) are exposed to hydrogeological risks such as landslides, floods, or coastal erosion. Moreover, 1.3 million people are exposed to landslide risk, while 6.8 million are exposed to hydraulic risk. Out of a total of over 14.5 million buildings, 3.9% are located in areas with high and very high landslide hazard, whereas 10.7% are located in flood-prone areas.” For these reasons, it is considered essential to outline, as precisely as possible, the corrosive processes affecting the systems designed to mitigate such disasters, with the aim of ensuring proper monitoring and adequate maintenance.

The objective of this study is to provide an adequate understanding of the prevention systems against hydrogeological hazards that most frequently affect Italy. In particular, the research focuses on rockfall barriers, examining their components, functionality, and operating mechanisms. Special attention is given to the corrosive processes that impact these systems, with an analysis of their critical aspects as well as the relevant regulatory framework.

For the purposes of this thesis, it was deemed necessary to begin with an in-depth study and review of the existing literature concerning the various topics that define the research. Accordingly, a range of articles and books were examined, addressing subjects such as the geology and geomorphology of the Italian territory, prevention and safety devices against hydrogeological hazards, the processing and corrosion of steel, as well as the relevant national and international regulations.

This thesis is structured in two phases. The first is theoretical, with the aim of providing readers with all the tools necessary to understand the subject of this work, which is related to rockfall barriers and the corrosion they can host in the various territorial contexts that our country offers. The second phase highlights, through a photographic collection, the corrosive processes that affect and have affected protection systems in operation.



## 2 ROCKFALL PHENOMENON: NATURE AND DAMAGE ANALYSIS

This chapter addresses the issue of rockfall, outlining the origin of the phenomenon and describing it from both physical and mechanical perspectives, while identifying the geological causes that give rise to such catastrophic events. In addition, the flow of the analysis needed to compute the possible damage of the event is reported.

As mentioned in the introduction, hydrogeological hazards result from the concurrence of natural and anthropogenic activities. The following section will therefore illustrate the natural processes involved, in order to better understand their dynamics, as well as the circumstances under which human activity becomes detrimental to the stability of the terrain.

### 2.1 DEFINITION OF FALLING ROCK PHENOMENA: FACTORS AND CLASSIFICATION

Landslide phenomena are triggered by intense erosive activity, which may result in rockfall when occurring on fractured stone masses or detrital deposits, or in surface runoff when affecting fine sediments. A first classification on landslide can be based on the difference between mass movements and mass transport.

- Mass movements: the displacement of masses of material along the Earth's surface, occurring primarily as a result of gravitational forces. These processes are characterized by a non-selective nature and generally involve limited transport distances, thus resulting in a short span between the area of erosion (detachment) and the area of deposition (accumulation).
- Mass transport: the movement of material masses primarily driven by surface running water. These processes are characterized by a selective nature, conditioned by grain size, and may involve transport over considerable distances.

The predisposition makes a slope susceptible to landslides, but this only occurs when the following aspects are present:

1. Preparatory or predisposing causes: intrinsic instability factors essentially related to the lithological, structural, textural, and stratigraphic characteristics of the materials forming the slope.
2. Triggering causes: factors acting on a slope that is generally already intrinsically unstable. They are defined as such because they initiate landslide movement (e.g., intense rainfall, seismic activity, etc.).

Landslide phenomena can be divided according to their type of movement:

1. topple: a forward rotation of rock or soil out of a slope around a pivot point, leading to its overturning;
2. slide: a downslope movement of material occurring along one or more well-defined shear surfaces;
3. lateral spreads: a horizontal extension and fracturing of ground, often triggered by liquefaction or loss of strength in underlying layers;
4. flow: a continuous, fluid-like movement of soil, debris, or mud in which particles move independently;
5. fall: a sudden, free or bounding descent of rock or soil detached from a steep slope or cliff.

The one analyzed in this work is the fall, particularly the rockfall. This phenomenon (Figure 1) is a gravitational slope instability process, involving the detachment and fall of rock materials from cliffs or steep faces. It is triggered by the loss of static equilibrium of blocks or rock portions due to predisposing factors (fracturing,

lithological and structural discontinuities, weathering, thermo-hygrometric variations) and triggering factors (earthquakes, intense rainfall, load variations, anthropogenic actions), which lead to the loss of cohesion between exposed lithological elements and the failure of mechanical bonds within the rock mass. From a kinematic perspective, the movement of blocks primarily occurs through free fall, rebound, sliding, rolling, or combinations thereof, along trajectories controlled by geomorphological characteristics and slope angle. Detachment can occur because of tensile or shear failure of the rock. Rockfall represents a type of rapid movement, generally of limited spatial scale, but with high kinetic energy, capable of producing significant impacts on infrastructure, settlements, and natural systems located downslope. The kinetic energy associated with motion, which varies depending on the mass, velocity, and trajectory type, is a fundamental parameter for the design and verification of protective structures, such as rockfall barriers. During free fall, the potential energy of the rock is converted into kinetic energy. Rarely does a rock move purely by rolling; in most cases, motion occurs through a close sequence of rebounds, generating parabolic trajectories of modest height (Volta, 2011).

(Hoek & Bray, 1981) exhibit the characteristics of this phenomenon that are numerous and makes its analysis complex and challenging. However, it can be stated that two aspects primarily distinguish rockfall from other types of landslide movements:

- The detachment and subsequent fall of a rock, or multiples rocks, involve a single portion of the rock mass, while the dynamic behavior of each individual portion is largely independent of the others.
- The size of the moving rock element is generally small in comparison with other geometric characteristics of the problem, such as the vertical drop or the length of the fall trajectory.

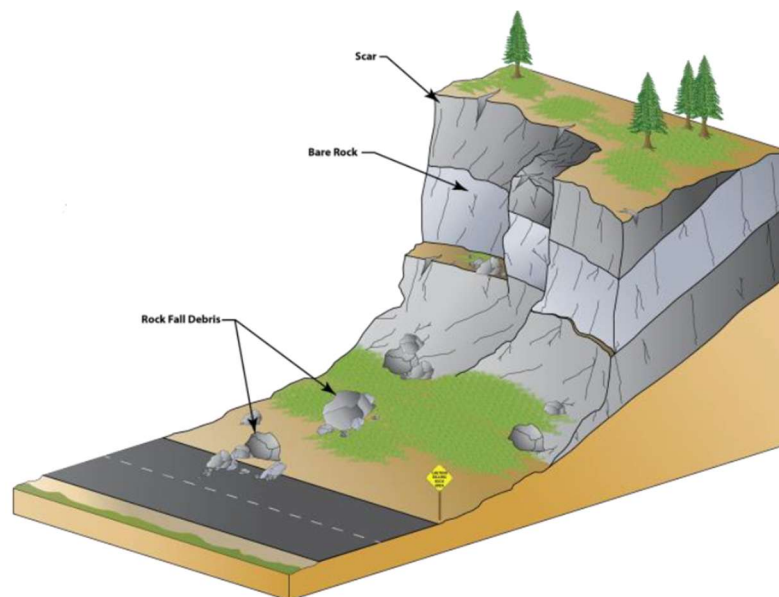


*Figure 1: Rockfall scheme (Fanti, 2015)*

The susceptibility of a slope to rockfall is closely related to a set of geomorphological and geological factors that influence both its initiation and evolution. From a geomorphological perspective, slope angle is the primary parameter: steep slopes ( $>40-45^\circ$ ) promote gravitational instability and reduce the frictional mechanisms that counteract detachment (Varnes, 1978). The overall morphology of the relief also plays a significant role: near-vertical cliffs, buttresses, gullies, and detachment niches represent preferential zones for stress accumulation and the release of rock blocks. The presence of debris deposits at the base, the depth of

colluvium, and the channeling conditions of blocks along the slope strongly affect the trajectory and run-out distance of the mobilized material (Agliardi & Crosta, 2003).

From a geological perspective, lithology and mechanical properties are decisive for slope stability. Compact and coherent rocks, despite their high intrinsic strength, are susceptible to fracturing and sudden detachment along discontinuity planes. Stratified rocks, on the other hand, show vulnerability related to the orientation of bedding planes relative to the slope: when the bedding dips downslope at an angle similar to the slope, the risk of collapse significantly increases (Hoek & Bray, 1981). Similarly, fracture systems, joints, faults, and schistosity planes constitute the main zones of weakness, serving as preferential detachment surfaces and reducing the cohesion of the rock mass (Cruden & Varnes, 1996).

Lithological weathering and weather-climatic degradation processes constitute additional predisposing factors. Freeze–thaw cycles, daily and seasonal thermal variations, and chemical weathering processes promote the widening of fractures and progressive weakening of rock blocks, facilitating their detachment (Matsuoka & Sakai, 1998). Water infiltration increases pore pressure and reduces the mechanical strength of materials, particularly in porous rocks or areas affected by open discontinuities (Hungr, Leroueil, & Picarelli, 2014).

Overall, the combination of geological setting (lithology and tectonic structures) and slope morphology defines the degree of predisposition of a site to rockfall. These elements, together with dynamic climatic and seismic factors, must be carefully analyzed in hazard assessment models and in the design of protective structures, such as rockfall barriers (Corominas, et al., 2014).

It can thus be affirmed that rockfall is triggered by geomorphological and geological factors. The main contributors described above are summarized in (Table 1)

Category	Factor	Description	References
Geomorphological	Slope inclination	Angles >40–45° promote detachment and reduce frictional resistance	(Varnes, 1978) Slope Movement Types and Processes, 1978)
	Relief morphology	Sub-vertical cliffs, gullies, niches, and buttresses represent preferential detachment areas	(Agliardi & Crosta, 2003)
	Debris deposits at the base	Influence the run-out distance and trajectory of fallen blocks	(Agliardi & Crosta, 2003)
	Topographic channeling	Presence of gullies and ravines concentrates the energy and propagation of blocks	(Hoek & Bray, 1981)
Geological	Lithology	Variable mechanical properties: compact rocks are resistant but prone to fracturing	(Hoek & Bray, 1981)
	Bedding orientation	Layers dipping downslopes at an angle similar to the slope increase the likelihood of rockfall	(Cruden & Varnes, 1996)
	Structural discontinuities	Fractures, joints, faults, and schistosity planes act as weakness surfaces	(Cruden & Varnes, 1996)
	Lithological weathering	Physical (freeze-thaw, thermal variations) and chemical process that weaken rock blocks	(Matsuoka & Sakai, 1998)
	Water infiltration	Increases pore pressure, reduces strength, and promotes fracture opening	(Hungr, Leroueil, & Picarelli, 2014)

*Table 1: Geomorphological and geological factors predisposing rockfall.*

For a better identification of the phenomenon under examination it is necessary to introduce classification. The act of classification represents a conceptual challenge, in which the criteria defined by Fanti, 2015 reported below must be respected:

- scientific validity: the use of objective criteria;
- finalization: the use of criteria relevant to hazard mitigation;
- practicality: the use of criteria that can be effectively applied in practice.

Significance is attributed to the classification proposed by Varnes in 1978, who developed a system for categorizing slope instability processes, based on the differentiation of the phenomena introduced in the previous chapter. His system is structured around two main characteristics: the type of movement and the type of material subject to instability. As previously described, the principal types of discontinuity phenomena can be classified as topples, slides, spreads, flows, and falls. A sixth class, referred to as complex landslides, represents the spatial and/or temporal combination of two or more of the afore mentioned movement types. The material involved may consist of rock or soil, the latter further subdivided into debris and earth (Lecce, 2019). A landslide is therefore classified using a matrix system, in which the rows represent the type of movement and the columns the type of material, Table 2 report the Hungr classification. Which is an update of the Varnes classification.

Type of movement	Rock	Soil
Topple	Rock blocks topple	Gravel/sand/silt topple
	Rock flexural topple	
Slide	Rock rotational slide	Clay/silt rotational slide
	Rock planar slide	Clay/silt planar slide
	Rock wedge slide	Gravel/sand/debris slide
	Rock compound slide	Clay/silt compound slide
	Rock irregular slide	
Spread	Rock slope spread	Sand/silt liquefaction spread
		Sensitive clay spread
Flow	Rock/ice avalanche	Sand/silt/debris dry flow
		Sand/silt/debris flowslide
		Sensitive clay flowslide
		Debris flow
		Mud flow
		Debris flood
		Debris avalanche
		Earthflow
Slope deformation	Mountain slope deformation	Soil slope deformation
	Rock slope deformation	Soil creep
		Solifluction

Table 2: Hungr's classification: New version of Varnes classification

## 2.2 ROCKFALL RISK ANALYSIS PROCEDURE

The main objective of a risk analysis is to describe risk. To understand what it means, it must be known what risk is and how it is expressed. In this chapter the meaning of risk is defined and how it is expressed (Aven, 2015).

Risk analysis is the use of available information to estimate the risk to individuals or populations, property or the environment, from hazards. Risk analyses generally contain the following steps: definition of scope, danger (threat) identification, estimation of probability of occurrence to estimate hazard, evaluation of the vulnerability of the element(s) at risk, consequence analysis, and their integration. The analysis can be qualitative or quantitative. (Marchelli M. , Rockfall risk assessment, 2000).

The main objective of risk analysis is to provide a rational basis for decision-making in risk management, enabling the implementation of effective mitigation and prevention measures.

Numerous publications in recent years have addressed the topic of natural events and their impact on human activities. In these works, terms such as hazard, risk, and vulnerability have been used with varying meanings by different authors. In 1986, Varnes, together with the United Nations Disaster Relief Office (UNDRO) and UNESCO, provided the following definitions:

- susceptibility: probability of a person, place, or system to be exposed to a hazard or threat due to inherent or acquired characteristics
- natural hazard (H): the probability of occurrence within a specific time period and considering a specific area subject to a potentially damaging phenomenon.
- vulnerability (V): the degree of loss of a given element or set of elements at risk, resulting from the occurrence of a natural phenomenon of a given magnitude. It is expressed on a scale from 0 (no damage) to 1 (completely damaged);
- exposure (E): possibility of people, property, infrastructures, economic activities, or environmental assets to be affected by the source of hazard. It expresses the spatial, temporal, and quantitative relationship between the hazard and the element at risk:
- specific risk (Rs): the expected degree of loss due to a particular natural phenomenon. It can be expressed as the product of H and V Eq. (1).

$$Rs = E \times H \times V \quad (1)$$

- elements at risk (El): refers to the population, property, economic activities, including public services, etc., exposed to risk within a specific area;
- total risk (Rt): represents the expected number of human lives lost, injured persons, property damage, or disruption of economic activities due to a particular natural phenomenon and can therefore be calculated as shown in Eq. (2).
- value (Val): represents the value in terms of costs, public utility, environmental importance for each element at risk.

$$Rt = (H \times E) \times V \times Val \quad (2)$$

Eq. (2) can be rewritten using the definition damage Eq. (3), which is the occurrence of the loss of the value if the simulated scenario takes place.



$$D = V \times Val \quad (3)$$

Models can be useful tools for assessing rockfall risk in relatively large mountainous areas (>500 km<sup>2</sup>), with the aim of improving the protection of residential areas and at-risk infrastructure (Dorren, 2003).

In 2003, Dorren published a study with the objective of summarizing existing rockfall models and proposing modifications to make them suitable for predicting rockfall at a regional scale. Firstly, he summarized the basic mechanisms of rockfall, including knowledge of the main modes of motion: falling, bouncing, and rolling. Secondly, he classified the models into three groups: (1) empirical models, (2) process-based models, and (3) models based on Geographic Information Systems (GIS). For each type of model, he summarized the basic principles and their capability to predict rockfall run-out zones, also including a discussion on how a model should be developed for the prediction of such zones. for rockfall run out at a regional scale (Dorren, 2003). Such approaches are fundamental to the design of rockfall protection structures, as they provide realistic design values for the forces involved.

### **2.2.1 Identification of the danger**

The danger is related to the most likely instability scenario: its estimation requires the characterization of the rock mass (i.e., geomechanically survey, rock quality, etc.) and the consequent identification of the rockfall source zones (i.e., detachment niches) and estimation of rock volumes involved. (Scavia, et al., 2020). Identification must be carried out in order to find the natural phenomenon that could lead to damage, described in terms of its geometry, mechanical and other characteristics, the type of destructive phenomenon and the possible causes or predisposal factors (such as seismic data or topography). For such a scope on site and around site investigation are needed within monitoring and historical analysis (Marchelli M. , Rockfall risk assessment, 2000).

### **2.2.2 Scenario definitions**

In order to define a realistic and reliable scenario for rockfall risk assessment, it is essential to conduct a thorough evaluation of the source area from which the phenomenon originates. This evaluation forms the basis for the subsequent modeling and analysis, as it directly influences both the dynamics of the rockfall and its potential impacts. Critical parameters to be considered include the initial intensity of the phenomenon, which is generally related to the velocity of movement, the initial volume of the detached material, and the return period associated with an event of a given magnitude. (Marchelli M. , 2020)

The initial intensity of the rockfall is typically determined through a combination of physical-mechanical properties of the rock mass, such as density, cohesion, internal friction angle, and fracturing characteristics, together with historical and empirical data on past events. Integrating these factors allows for a more precise representation of the potential energy and kinematics of the falling blocks. Furthermore, the return period, defined as the average interval of time between events of a specific intensity, provides crucial information for probabilistic risk assessments and helps in identifying areas of higher susceptibility.

By carefully defining the scenario with these parameters, it becomes possible to establish a solid foundation for subsequent propagation modeling, hazard mapping, and risk evaluation. This approach enables the identification of critical zones where mitigation measures may be necessary and supports the development of decision-making strategies aimed at reducing exposure and potential damage to people and infrastructure. Ultimately, scenario definition is a key step in ensuring that rockfall risk analyses are both realistic and actionable, bridging the gap between theoretical modeling and practical risk management applications.

### **2.2.3 Propagation analysis and hazard evaluation**

Once evaluated the type of damaging potential phenomenon, its initial intensity and return period; its evolution must be analyzed. Such operation is called hazard zoning/mapping. To that, a qualitative or a quantitative analysis can be carried out. Qualitative analysis is a deterministic approach based on geomorphological in-situ survey or parametric maps; quantitative analysis is a statistical approach based on a geomechanical approach.

Between these, the geomechanical approach lends to an accurate model of the phenomenon. For the spatial propagation analysis, morphological empirical models or physically based models can be used. With the first, propagation and energy dissipation are evaluated in function of the length of the path and are based on statistical analysis of previous events and on analyzable physical parameters. The seconds are based on the understanding of physics of the process, describable through physically based equations.

The union of both these methods brings to a numerical model which is essential to realize an accurate hazard map (Marchelli M. , Rockfall risk assessment, 2000).

To carry out an accurate propagation analysis, it is essential to possess a comprehensive understanding of:

- the trajectory of the blocks;
- the type of motion;
- the runout of the falling rocks & stopping point;
- velocity and kinetic energies of the block;
- passing heights of the blocks for each point along their fall paths.

These data are obtainable through rockfall simulation, whose parameters can be validated with in situ tests and back analysis (Marchelli M. , Rockfall risk assessment, 2000).

#### **2.2.3.1 Trajectory analysis**

The analysis of rockfall trajectories is carried out using a mathematical–physical model capable of predicting the path of falling blocks and the associated kinematic parameters, such as impact energy, bounce height, velocity and runout distance. To obtain reliable results, it is essential to correctly describe the underlying physics of the motion, which typically consists of three main phases: the initial fall, the flight in air between successive impacts, and the interaction between the block and the slope surface. During these phases, blocks may interact with the terrain in several different ways, including rolling, sliding, bouncing and fragmentation, each governed by distinct mechanical principles and strongly influenced by factors such as block size, shape, rotational inertia and surface roughness. These interactions ultimately control the dissipation or redistribution of energy along the trajectory and therefore must be accurately represented in the modelling approach.

From a mechanical point of view, the equations describing the initial detachment and fall are based on the laws of free-fall motion and projectile (parabolic) motion. After detachment, the block follows a parabolic trajectory until the next impact, where the contact mechanics determine the block's post-impact velocity and direction. The alternation of these phases forms the complete rockfall trajectory, which must be reconstructed through a combination of analytical expressions and numerical simulation.

The model can be even simplified in terms of boulder geometry and type of motion. The block can be schematized as a lumped mass or a sphere, if the information about it are low, while if the information are exhaustive a rigid complex shape or a discrete element complex shape can be used. The type of motion is function of the topography, if a well-done representation is present, a 3D model can be used.

Once all the information are collected and the choice of the correct simplification is performed, the analysis can be run. The two possible performable analysis are deterministic and probabilistic. With the first, the safety factor is calculated as deterministic quantity on the basis of one or more realistic scenarios. With the second, a statistical distribution is assigned to each input parameter and in each analysis the values of the input parameters are randomly selected from their interval, this procedure is better described in chapter 4.1

#### **2.2.4 Evaluation of the elements at risk: value and vulnerability**

Once evaluated the evolution of the phenomenon it is necessary to consider the elements at risk, which could be people, buildings, infrastructures, environment. Any element must be analyzed with an appropriate scale (small, medium, large or detailed), the type of the scale defines the accuracy of the analysis (Marchelli M. , Rockfall risk assessment, 2000).

Every element at risk has intrinsic value, which could be:

- physical: depending on the cost of the element;
- economic: depending on the activity/production;
- social: depending on the number of people involved and the social utility of the element;
- environmental: depending on the flora and fauna present

The vulnerability of the element at risk is determined by the degree of loss, which results from the occurrence of a dangerous phenomenon of a given magnitude. The assessment of vulnerability can be performed with both qualitative and quantitative approaches. This parameter depends on two factors:

- Phenomenon function (Eq.4) depending on the intensity of the hazard;

$$f(\text{phenomenon}) = f(I) \quad (4)$$

- Element at risk function (Eq.5), depending on quality and type of construction, position/orientation, possibility to avoid unease, type of activity or production, and presence of protection elements.

$$f(\text{element at risk}) = f(\text{Typology}) = f(T) \quad (5)$$

## 2.3 RISK MITIGATION STRATEGIES

Risk mitigation strategies encompass all the actions, measures, and techniques aimed at reducing the probability of occurrence of hazardous events and/or minimizing their potential consequences on exposed elements through the use of protective measures. Within the context of slope and rockfall hazard management, mitigation represents a fundamental phase of the overall risk management process, following hazard identification and risk assessment. Protective measures against rockfall aim to intercept and stop falling blocks along the slope. For this reason, it is appropriate that interventions are implemented along the blocks' trajectory or at the most critical points of the slope, making thorough geotechnical investigations and trajectory analyses of potential falling bodies essential (UNI Standard 11211-4:2018). Among the classifications regarding the different types of interventions for rockfall protection, the most widely used distinguish between:

- Active measures: act at the source of the problem by preventing the detachment of rock elements from the slope. Examples include modifications of slope geometry, mechanical strengthening, piezometric condition improvements, and interventions on the rock mass surface using anchors, bolts, rock nails, etc. This can be distinguished in interventions that modify mechanical resistance and Interventions acting on the rock mass surface (GEOPRODOTTI, s.d.).
- Passive measures: intercept or divert blocks that have already been mobilized, with interventions primarily located at the base of slopes or rock faces. Examples include slope reprofiling with intermediate benches, installation of rockfall barriers with various energy-dissipation technologies, protective walls, artificial tunnels, trenches, earth embankments (reinforced or unreinforced), revetments, reinforced earth structures, and cellular walls (Catanzariti, 2016).

Interventions that modify mechanical resistance: the basic principle of this type of intervention is the insertion of external elements into the unstable rock mass to enhance its stability and limit rockfall. To counterbalance the destabilizing force acting on the discontinuity surfaces, rock nailing can be employed using GEWY and DYWIDAG nails and bolts (GEOPRODOTTI, s.d.) (Figure 2).

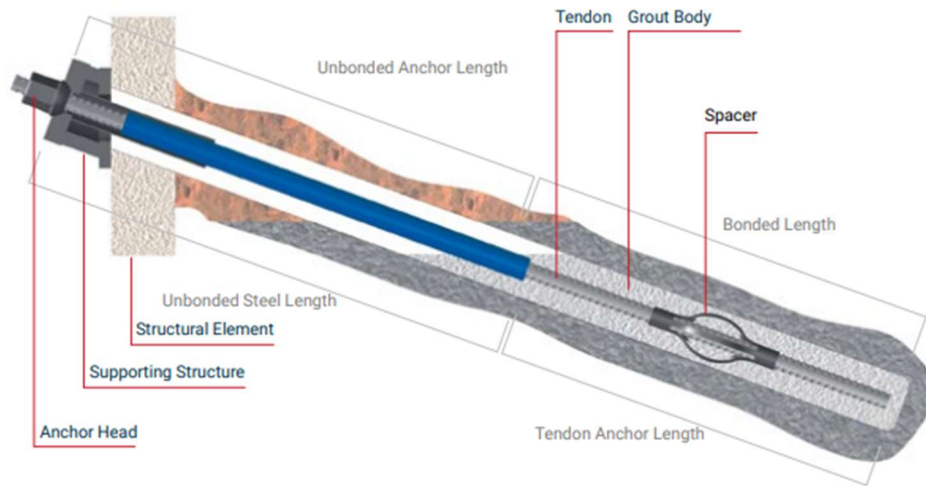


Figure 2: DYWIDAG nail. (DYWIDAG, 2025)

Interventions acting on the rock mass surface: this type of intervention prevents the initiation of progressive failure from the surface into the rock mass, through the use of high-strength steel meshes such as SPIDER (Figure 3), TECCO, and QUAROX, designed using dedicated software and often combined with widespread rock nailing measures (GEOPRODOTTI, s.d.).



Figure 3: SPIDER steel meshes (Geobrugg, s.d.)

Passive protective measures can be distinguished as follows:

Earth embankments (reinforced or unreinforced) (Figure 4): typically constructed at the base of unstable rock slopes prone to falls, toppling, rock detachment, and large-scale debris flows. Depending on slope characteristics and site constraints, the intervention may consist of a single embankment or a system composed of a berm and a rockfall embankment (*Unirock, s.d.*).

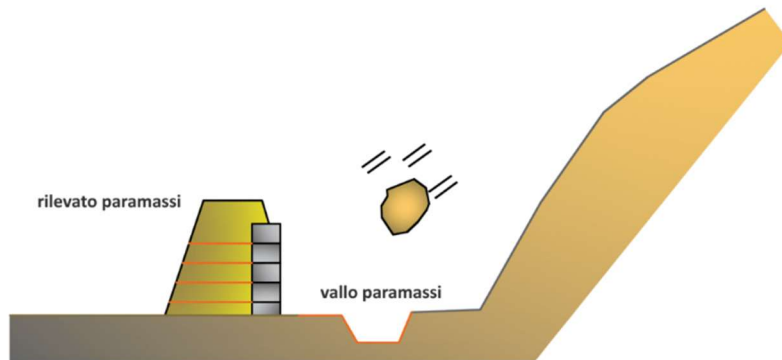


Figure 4: Earth Embankments. (*Catanzariti, 2016*)

Surface meshes and cortical reinforcements (Figure 5): the purpose of cortical reinforcements with double-twisted metal meshes is to prevent the fall of debris and small rocks and to improve the connection between the weathered surface layer and the intact rock mass at depth. These systems can be configured in a simple arrangement (anchored at the top and base) or reinforced with a wire rope mesh and supported by an adequate number of anchors (*GEOPRODOTTI, s.d.*).



Figure 5: Surface meshes. (*GEOPRODOTTI, s.d.*)

Installation of rockfall barriers (Figure 6): thanks to high-strength steel wire and straightforward installation, these types of interventions are often preferred over others. Further details regarding this intervention are provided in Chapter 3.



*Figure 6: Rockfall barrier. (Geobruigg, s.d.)*





### 3 ROCKFALL BARRIER

The net fence or rockfall barrier is a protection system essentially made of a net, intercepting and stopping the falling blocks, sustained by a metallic posts and connecting components, as ropes and connecting devices, which transfer the impact loads to the foundations. This system should be able to intercept the trajectories of rock blocks in motion along slopes and stop the blocks, deforming itself without breaking (Figure 7), absorbing elastic and/or plastic deformation stresses induced by the kinetic energy of the moving block (Marchelli M. , 2020).



Figure 7: Fallen rock in Fenille (Valle d'Aosta) on 24.10.2019 (Marchelli M. , 2020)

#### 3.1 COMPONENTS OF ROCKFALL BARRIERS

Rockfall barriers are passive protection systems that impede the natural progression of the fallen body thanks to net's elastic or plastic deformation. This deformation is possible thanks to the different components of the structure; the different elements that compose the protection device are:

- net fences;
- posts;
- post base system;
- rope anchorages;
- energy dissipating devices

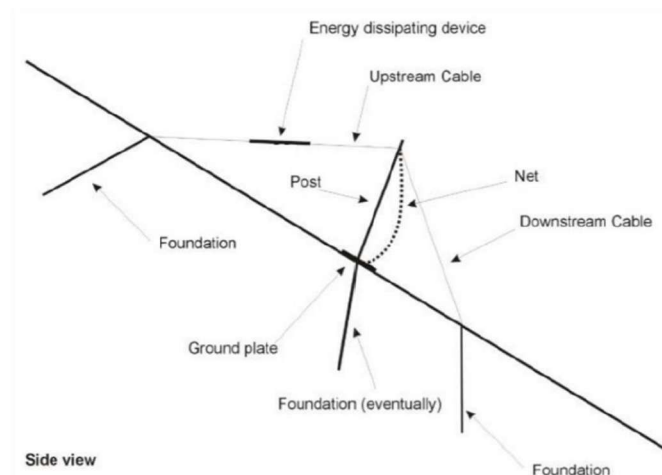


Figure 8: Lateral view of a falling rock protection kit (EOTA, 2018)

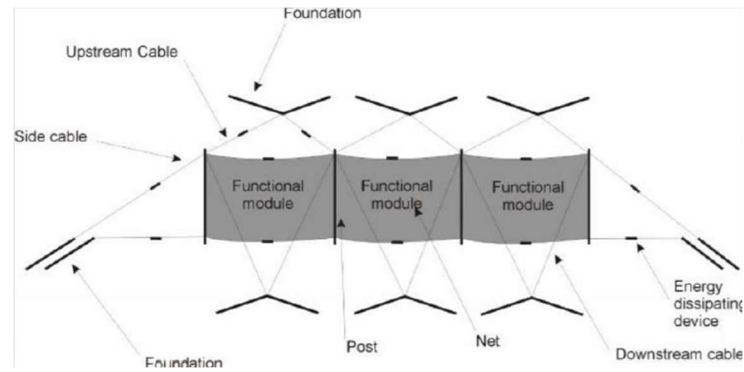


Figure 9: Back view of a falling rock protection kit (EOTA, 2018)

### 3.1.1 Net fences

Net fences consist of a sequence of functional modules made up of:

- An interception structure;
- A support structure;
- Connection components.

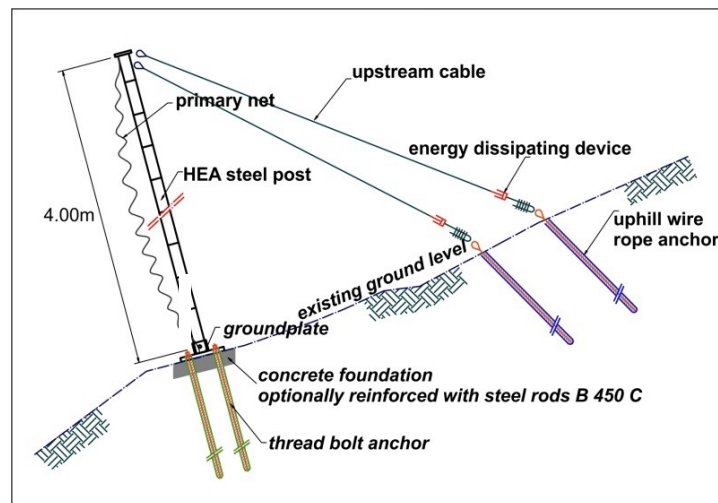


Figure 10: Detailed lateral view of a falling rock protection kit. (Güntel & Acar, 2016)

The interception structure is the principal net, made up of metallic cables, wires and/or bars of different types and materials (for example cable nets joined by clamps, submarine nets and ring nets. In the last two cases the rings forming the net are connected to each other). The structure presents even additional layers, usually with finer meshwork than the principal net, made up of cables and/or wires or other materials, that's because of the possibility of letting them pass through small pieces, which could be dangerous if reach high level of kinematical energy. The support structure is composed of posts made of different materials, geometries and lengths (for example, pipes or structural metallic elements, having a hinge at the bottom. Greater information about posts will be given in chapter 3.1.2.) Connection components are connecting ropes, steel cables, wires and/or bars of different types and material, junctions, clamps, energy dissipating devices (elements which can dissipate energy and/or allow a controlled displacement when stressed. Greater information about energy dissipation devices will be given in chapter 3.1.5) (Marchelli M. , 2020)

### 3.1.1.1 Net fences typologies

Ring net: has more extensive application than other typologies, because of its flexibility, energy dissipating ability and interconnection of the independent rings. However, there is usually destruction of the ring net when it comes to practical engineering applications (Chunlan, Zhiyong, Chengqing, Huaxin, & Shuai, 2022).



*Figure 11: Ring net in exercise (Meccaferrri, s.d.)*

Rhomboidal net:



*Figure 12: Rhomboidal net in exercise (Geobrugg, s.d.)*

Omega net:



*Figure 13: Omega net in exercise (Trumer Schutzbauten, s.d.)*



### 3.1.2 Posts

Posts are the elements that ensure the connection between the net fences and the ground. The connection is made through the posts base system (see chapter 4.1.3). The degree of the stiffness with which the connection between the mesh and the posts is made provides a better or worse dynamic response, thus determining greater or lesser deformation. This parameter depends on the site and fallen rock's characteristics (size, mass, elevation, inclination) that generates the event. Furthermore, the posts are also connected to the ground through the top, in this position the cables for energy dissipation are installed and anchored to the ground.

The section of the posts can be different, among the most used there are HEA profile (Figure 14) and round tube profile (Figure 15).



Figure 14: HEA profile post (Marchelli M. , 2020)

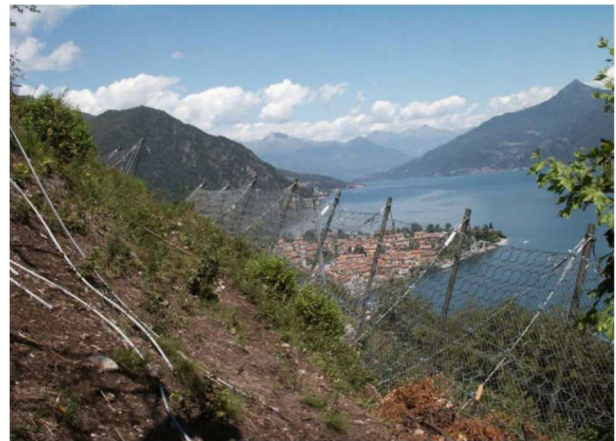


Figure 15: Round profile post (Marchelli M. , 2020)

### 3.1.3 Posts base system

Post base system transfers the load, and so the energy, from the post to the ground, depending on the typology of the barrier two different primary types of bases can be described:

1. Base with a fixed connection between the post and the plate (Figure 16), this typology is characterized by a fixed angle between the base plate and the post, in no situation it can be altered. This rigid connection is guaranteed through welding the base plate directly to the post beam with the help of stiffeners. This technique generates a self-supporting post that requires no retaining ropes for the post head, with the advantage of a smaller footprint, eliminating the need anchors upslope of the system and providing unobstructed access to the system in case of an event. This type of base system require more extensive anchoring for the base support, and thus are much heavier than hinged system with the same energy absorption capacity: hinged system distributes forces from the post head directly to ground anchors via upslope retaining ropes while the fixed post system require a larger post cross section to resist the forces as well as more involved anchoring of the post base to resist overturning. Since the rigid connection must be guaranteed, where the bedrock is located at surface, the post can be anchored directly to the subsurface, but in the case of soils, a system of concrete pedestals with compression and tension anchors is required (Marchelli M. , 2020).



Figure 16: Fixed support (Marchelli M. , 2020)

2. Base with hinged connection between the post and the plate (Figure 17, Figure 18, Figure 19): this typology has independent base plate and post linked together using a pin. The angle between the post and base plate is controlled by retaining ropes attached to the head of the post and anchored on the upslope side of the system. This system is light weight and highly adaptable to difficult terrain, often being installed with helicopters. The use of retaining ropes means lower force at the base plate and the hinged connection eliminates the overturning of the base, for this reason the base support is often minimal, normally using two rock or soil anchors and sometimes a small leveling pad (Marchelli M. , 2020).



Figure 17: Mono-directional hinge (Marchelli M. , 2020)



Figure 18: Bi-directional hinge (Marchelli M. , 2020)



Figure 19: Spherical hinge (Marchelli M. , 2020)

Depending on the material on which the base system is placed, the installation techniques change:

- Soil (Figure 20):
  1. set the inclination of the base plate from  $0^\circ$  to  $30^\circ$  with respect to the horizontal;
  2. drill two anchor holes: one vertical and one with  $45^\circ$  inclined to the base plate;
  3. prepare foundation **(111)**: dimension and reinforcement of the concrete foundation is set by the project engineer (recommended dimension: 0,6 x 0,5 x 0,2 m);
  4. insert anchor **(05)**, washer plate **(09)** and nuts **(10)** (these two must be installed on both side see Figure 21), (the calculation of the anchor length is set by the project engineer;
  5. apply the stabilization tube **(04)** for vertical anchor;
  6. grout the anchor **(05)** in soil **(110)**;
  7. pour concrete in the foundation **(111)**;
  8. fasten the nuts **(10)** until an initial tensile force of approximately 30kN is reached.

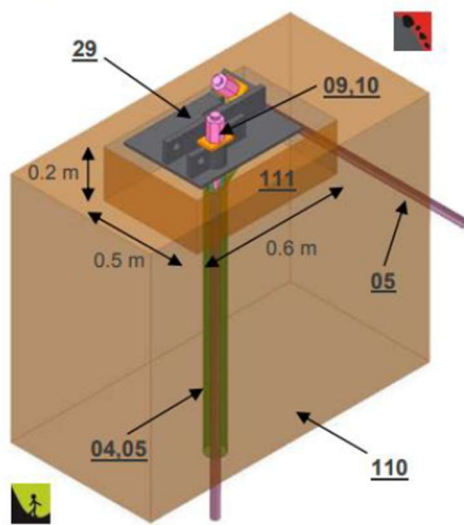


Figure 20: Base system on soil (Geobrugg, s.d.) reported by (Marchelli M. , 2020)

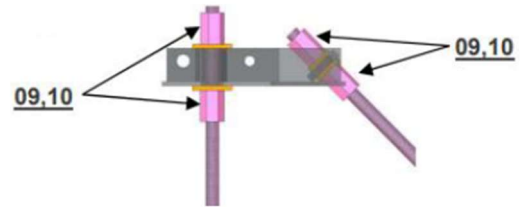


Figure 21: Washer plates and nuts correct placement (Geobrugg, s.d.) reported by (Marchelli M. , 2020)

- Rock (Figure 22):
  1. level the rock from  $0^\circ$  to  $30^\circ$  from the horizontal underneath the base plate (29);
  2. drill into the rock (112) two anchor holes: both perpendicular to the base plate (29);
  3. grout in the anchors (08), the calculation of the anchor length is set by the project engineer;
  4. realize a thin levelled layer that ensure a stable placement of the base plate;
  5. position the base plate (29) into the levelling layer;
  6. fasten the nuts (10) until an initial tensile force of approximately 30kN is reached.

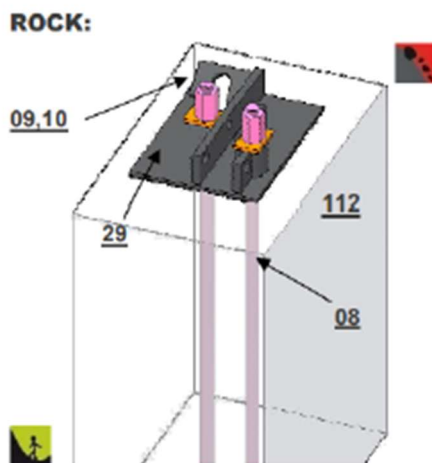


Figure 22: Base system in rock (Geobrugg, s.d.) reported by (Marchelli M. , 2020)

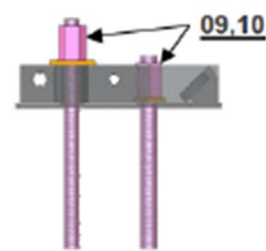


Figure 23: Washer plates and nuts (Geobrugg, s.d.) reported by (Marchelli M. , 2020)



- Concrete (Figure 24):
  1. excavate foundation pit (111);
  2. drill the holes for tie back anchoring (07), (the calculation of the anchor length is set by the project engineer);
  3. prepare concrete foundation (111) dimension and reinforcement of the concrete foundation (111) that are set by the project engineer;
  4. grout tie back anchoring (07) with nuts (10) and washer plates (09);
  5. install the central anchors (08) with help of the base plate (29), washer plates and nuts must be installed on both sides of the plate (29) as shown in ;
  6. pour concrete foundation (111);
  7. fasten the nuts (10) until an initial tensile force of approximately 30kN is reached.

#### CONCRETE:

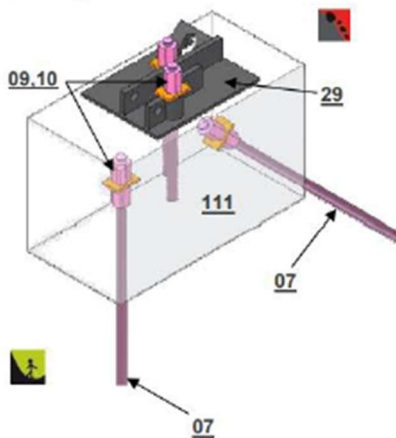


Figure 24: Base system in concrete (Geobrugg, s.d.) reported by (Marchelli M. , 2020)

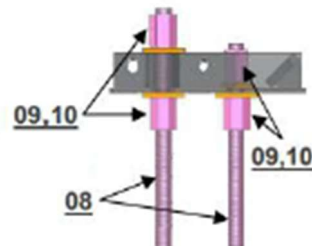


Figure 25: Washer plates and nuts (Geobrugg, s.d.) reported by (Marchelli M. , 2020)

Concrete solutions can be used in both soil and rock situations.

### 3.1.4 Ropes anchorages

Rope anchorages are components of the barrier that guaranteed the connection between the rope and the ground, thanks to this connection the structural capacity of the system is increased. Anchors are placed at the edges of the barrier connecting to the ground the top, lateral and bottom ropes. Additional ropes are present in the central area of the barrier, depending on its length, these are top ropes (connected to the top of the post) and are called intermediate suspension. The intermediate suspensions are usually two and are connected to the ground through two independent and singular anchors.

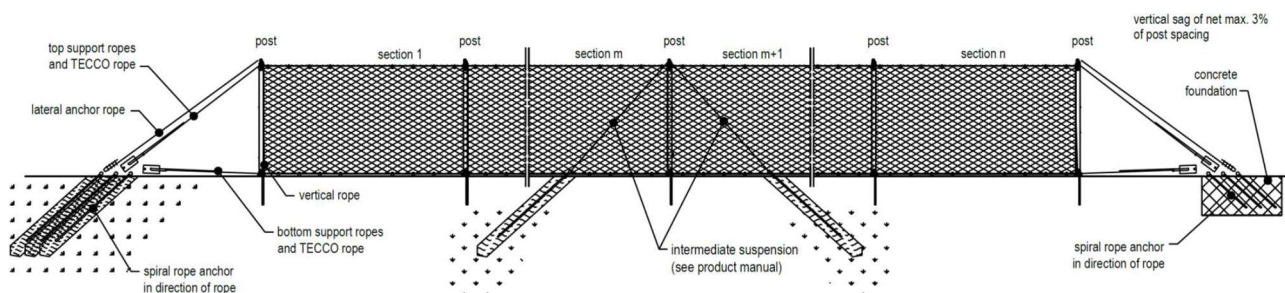


Figure 26: Front view of a rockfall barrier, showing the ropes anchorages position (Geobrugg, s.d.) reported by (Marchelli M. , 2020)

There are two different types of rope anchorages:

1. grouted bars: this system is also called solid bar because the anchor is grouted into the ground realizing a rigid scheme. As reported from Ingram & Wagner, (2012) at the 63<sup>rd</sup> annual highway geology symposium in California, this type of anchor were not working properly because rocks that were shearing off the top of the anchor bars as they rolled down the slope prior to impacting the barrier resulting in post failures and reduced net height, thus compromising the systems capacities before impacting the net; in addition the force that are transferred to the anchors is more in shear than the vertical pull-out direction, reducing the capacities required as the shear strengths in the solid bars were considerably less than the required pull-out strength.



*Figure 27: Bent solid bar anchor, due to shear, after impact (Ingram & Wagner, 2012)*

2. Injected cables: The use of cable anchors in the design of all rockfall mitigation systems allows for a greater degree of assurance with respect to the grouted bars, so that the anchor will not be compromised. This is true for impacts from falling rocks in barrier installations or potential shearing or bending when movement of rocks under a drapery system occurs. The use of a cable anchor also provides higher capacities in a similar depth and diameter holes than the use of solid bar anchors. Cable anchors conform to uneven ground conditions due to their flexibility. They can also flex in multiple directions during loading events, which allows for the transfer of load to the ground. Thus, ensuring loads, during rockfall events, are transferred to the anchors and prevents damage to the systems. For these reasons wire rope cable anchors should be specified in all rockfall systems instead of solid bar anchors as they provide better overall products than the solid bar anchors (Ingram & Wagner, 2012).



*Figure 28: Loaded wire rope cable anchor (Ingram & Wagner, 2012)*



## Rope Anchorage

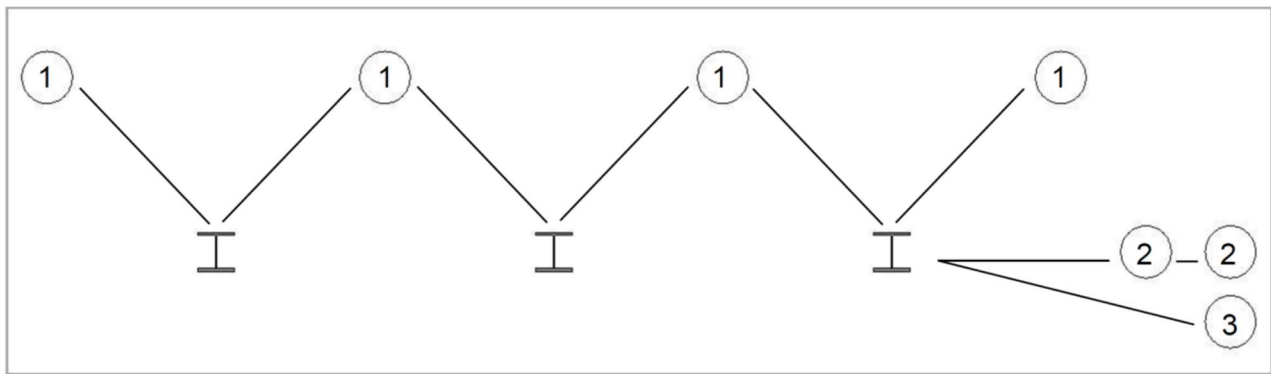


Figure 29: Rope anchorage position (Geobrugg, s.d.) reported by (Marchelli M., 2020)

In (Figure 29) the scheme represent with number (1) is the upslope anchor (Figure 30), with number (2) and (3) respectively support rope and lateral rope (Figure 31).

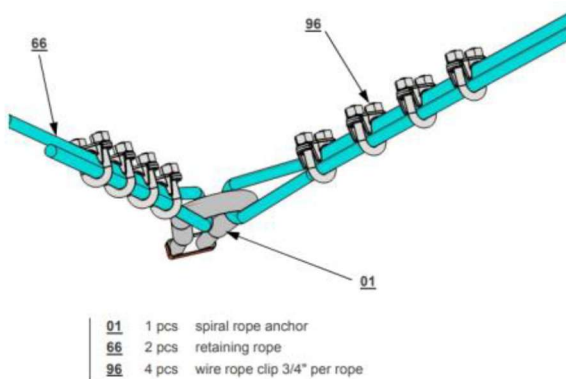


Figure 30: Upslope anchor, technical datasheet from (Geobrugg, s.d.)

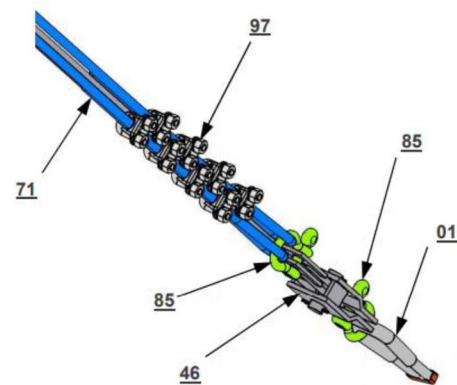


Figure 31: Support and lateral rope anchor, technical datasheet from (Geobrugg, s.d.)

As shown in (Figure 30) number (96) and (Figure 31) number (97) a cable clips are present, usually three or four per rope . These clips are usually U-bolt clamp (Figure 32).

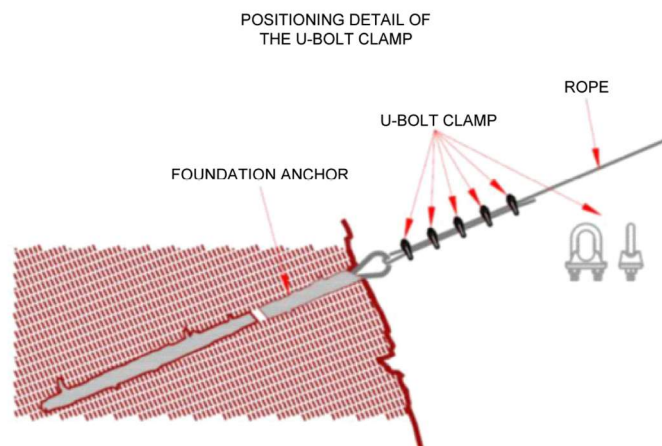


Figure 32: Positioning detail of the U-bolt clamp (Meccaferrri, s.d.)

### 3.1.5 Energy dissipation devices

Energy dissipation devices may be defined as the mechanism incorporated into the flexible barrier system to absorb internal energy, helping to reduce stress within the structure in a rock impact. They transform the kinetic and potential energy of the impacting block into deformation energy, fracture or heat generated by friction (Marchelli M. , 2020).

When rocks fall from areas which are difficult to reach or, when the natural conditions do not allow the building of large structure, the impact energy can differ from 150 kJ to 8000 kJ, energy dissipaters are an essential device in this context. The maximum absorbed energy of a barrier without these device is 100 kJ, the addition of energy dissipator brings this value up to 8500 kJ (Castanon-Jano, Blanco-Fernandez, Castro-Fresno, & Ballester-Munoz, 2017)

Brake elements currently on the market are grouped in four classes according to the way they dissipate energy:

- brake elements by pure friction;
- brake elements by partial failure;
- brake elements by plastic deformation;
- brake elements by mixed friction/plastic deformation.

Pure friction elements were the first brakes to be invented due to their simplicity. In this system the rope runs through a device that generates friction between itself and the rope, such that the energy is well dissipated. Pressure is applied on the clamp by the bolts' torque (Castanon-Jano, Blanco-Fernandez, Castro-Fresno, & Ballester-Munoz, 2017). Depending on the expected impact the system can be repeated through the rope in order to increase the dissipation capacity. There different typology of pure friction brake elements, in (Figure 33, Figure 34, Figure 35) are reported three of the most used.

(Figure 33) and (Figure 35) show a brake system where cable are compressed on a plate through a clamp with bolts. This cable is fixed at one end to the post, and the other end is free to allow slippage in the clamp, in order to ensure the transmission of force to the ground, the plate is connected to the anchor (Castanon-Jano, Blanco-Fernandez, Castro-Fresno, & Ballester-Munoz, 2017).

(Figure 34) shows a brake system composed of a looped cable, that pass, more than one time, through holes properly placed into a plate, increasing the plates dimension and the number of holes the potential dissipation energy can be increased.



Figure 33: IGOR-SAFE brake system (Meccaferrri) (Marchelli M. , 2020)



Figure 34: ISOFER-INCOFIL brake system (INCOFIL) (Marchelli M. , 2020)



Figure 35: ISO-200 brake system (meccaferrri) (Marchelli M. , 2020)

Partial failure brake elements can be dangerous due to the possibility of rupture in unexpected zones of the brake. The preservation of brake integrity is essential. Otherwise, the connections of the free end of posts with the anchors would fail leaving the barrier inoperable. Metal disc brakes are installed in a continuous cable where there are no discontinuities; therefore, when all the discs break, the cable bears the loads preserving the barrier integrity. For these reasons these elements are the least common (Castanon-Jano, Blanco-Fernandez, Castro-Fresno, & Ballester-Munoz, 2017).

Figure 36 a) shows an element composed of a tube within which two cables move in opposite directions from each side. These drag a sharpened piece, which when entering in the tube divides it and dissipates energy. The work performed by the forces in the brake element to absorb kinetic energy is the same as the cut resistance of the tube multiplied by the cut length.

Figure 36 b) shows an element of this type that is composed of wires connected in parallel, the only one loaded is the inner one (the shortest) once this fails the load pass to the second one, until, at the ultimate failure, the last stage is reached with the stressing of the outer wire (the longest).

Figure 36 c) shows an element composed of a stack of steel ring, the wire pass enters from a side and exits from the same side, in the middle it is attached to a pivot, with greater dimensions respect to the rings. Once the wire is stressed, the pivot puts in compression the rings, making them fail sequentially.

Figure 36 d) comprises a disc with a series of drilled holes in a spiral pattern. When the cables transmit the force to the brake, the material between the holes deforms plastically, one after another, until failure. In addition, a second cable start works the full disc failed.

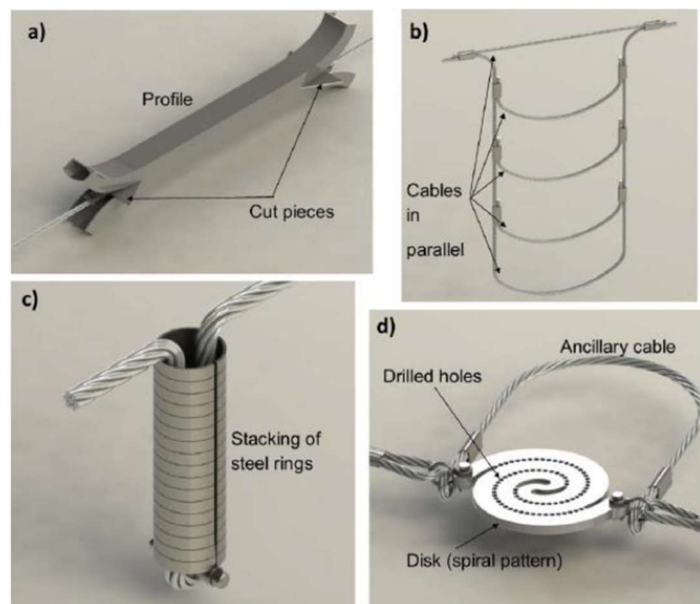


Figure 36: Partial failure brake system: a) by tube cutting (Sisyphe); b) by cables in parallel (Sol Systemes); c) metal disks (Tecnap Sàrl); d) Pfeifer brake system (Pfeifer), (Castanon-Jano, Blanco-Fernandez, Castro-Fresno, & Ballester-Munoz, 2017)

Brake elements by plastic deformation present an energy absorption based on non-recoverable deformation of some of their components.

Figure 38 present a system in which a steel spiral is connected at its ends to the cables by shackles. When tension is created in the cables, the spiral stretches deforming plastically (Castanon-Jano, Blanco-Fernandez, Castro-Fresno, & Ballester-Munoz, 2017).



*Figure 37: plastic deformation brake system: isodisk (PFEIFER) (Marchelli M. , 2020)*

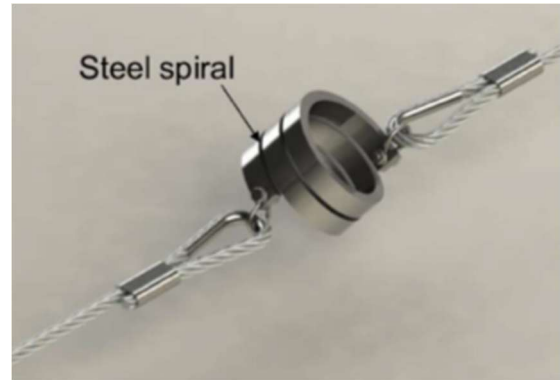


*Figure 38: plastic deformation brake system: spiral (TRUMER) (Marchelli M. , 2020)*

Brake elements by mixed friction/plastic deformation: friction is the first mechanism that activates in order to dissipate energy, once the brake reaches the end (Figure 41) of its stroke, plastic deformation mechanism start. In this way the service limit state (repeated impacts) is fulfilled. This type of solution must be always adaptable and durable.

Figure 39 and Figure 41 show the so called “Meccafferri brake”, is composed of two steel tubes and two rigid perforated plugs at the ends. Two cables coming from opposite directions pass through the tubes and are fixed in the plugs. When a rock impacts on a flexible barrier, the load transmission makes the plugs press against the tubes, generating buckling in the tube, with non-recoverable plastic deformation (Castanon-Jano, Blanco-Fernandez, Castro-Fresno, & Ballester-Munoz, 2017).

Figure 40 represent a brake in which the cable is conducted through a protective pipe in a ring shape. An aluminum sleeve acts as a compression element and fastens both ends of the tube. The tension caused by the rockfall on the cable leads to pipe-sleeve friction and the consequent pipe deformation (Castanon-Jano, Blanco-Fernandez, Castro-Fresno, & Ballester-Munoz, 2017).





Figure 39: Mixed friction/plastic deformation: string brake system (Meccaferrri, s.d.) (Marchelli M. , 2020)



Figure 40: Mixed friction/plastic deformation ring brake system (Geobruigg, s.d.) (Marchelli M. , 2020)



Figure 41: Mixed friction/plastic deformation string brake system: plastic deformation active (Meccaferrri, s.d.) and (RISP) (Marchelli M. , 2020)



## 4 ROCKFALL BARRIER DESIGN PROCEDURE

The procedure to follow for the design of this protection system is really complicated and restricted, considering that a failure in the rockfall barrier means, with high probability, important damage to buildings and lost life. There are different advice for the correct installation and assembly that the designer can follow to achieve a good project setup.

(Marchelli M. , 2020) reports correct installation and connection of the posts for net fences:

- the angle between the posts and the perpendicular (named  $\Omega$ ) depends on the terrain slope angle (named  $\beta$ ) (Figure 42);
- the angle between the upslope anchor rope and the post (named  $\gamma$ ) must be maintained between  $60^\circ$  and  $85^\circ$  (Figure 42);
- the default angle (named  $\alpha$ ) between the terrain and the post must be  $75^\circ$  (Figure 42).

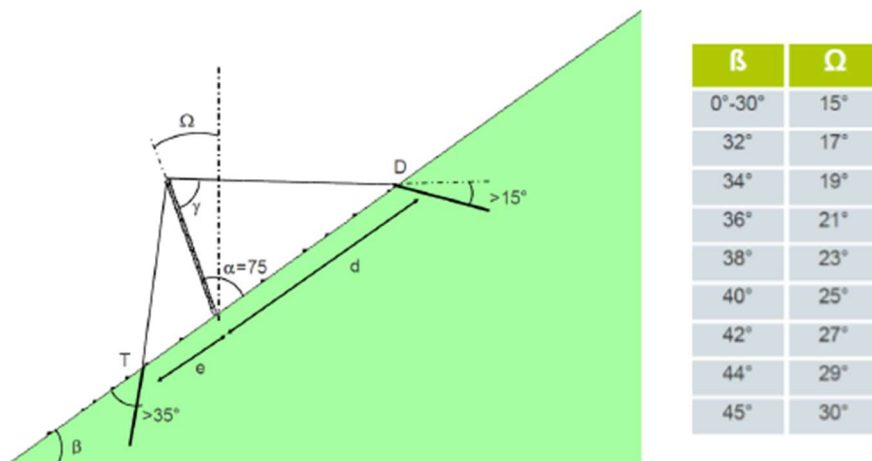


Figure 42: Correct installation scheme (Geobrugg, s.d.)

For a correct installation and connection of the rope anchors for net fences, the anchor holes must be drilled in the pulling direction, with a minimum angle of  $15^\circ$  to the horizontal (Marchelli M. , 2020).

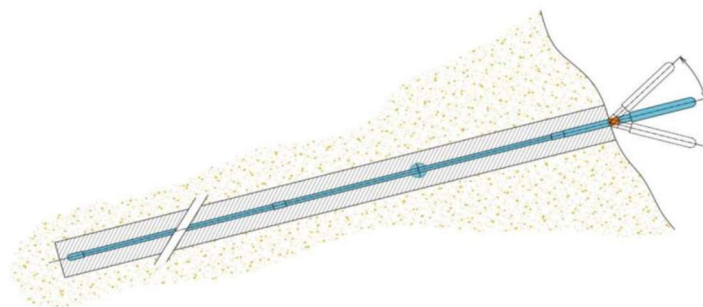


Figure 43: anchor direction hole and angle variation (Geobrugg, s.d.)

In addition, the different typologies of anchor ropes (top, lateral and intermediate) have a specific scheme to follow, reported in (Figure 44).

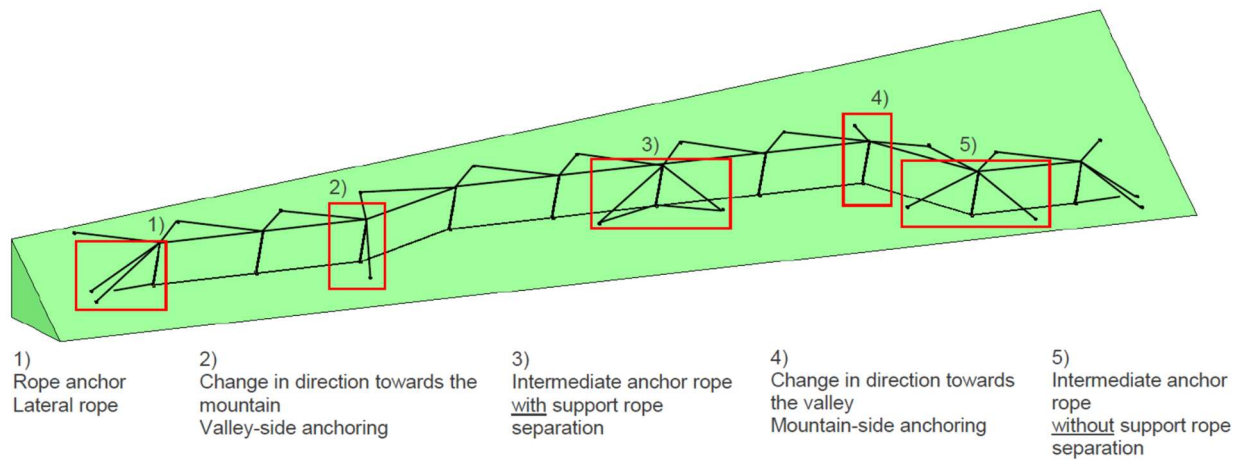
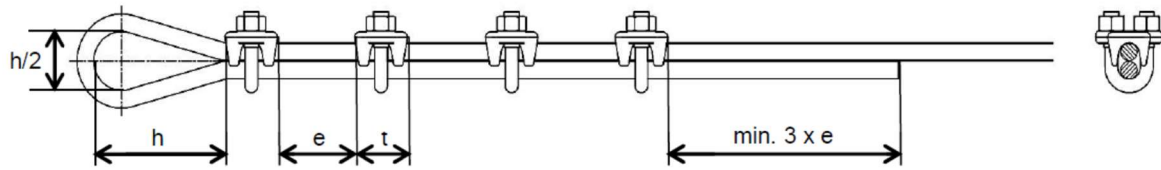


Figure 44: Rope anchors positioning, (Geobrugg, s.d.) (Marchelli M. , 2020)

Correct installation and connection of rope grips for net fences: as reported in the European Normative “EN 13411-5:2003 Terminations for steel wire ropes” the dimensions of the terminations depend on the nominal size of the rope. A scheme is reported in (Figure 45) (Marchelli M. , 2020).





Nominal size <sup>*)</sup> [mm]	Distance "e" [mm]	Required tightening torque <sup>**) </sup> [Nm]	Required number of wire rope clips	Width across flats [mm]
13	50 - 80	35	4	19
16	50 - 90	55	4	22

Wire rope di- ameter [mm]	Size of the wire rope clip	Required amount of wire rope clips	Required tightening torque lubri- cated [Nm]	Required tightening torque unlubricated [Nm]	Wrench size [mm]
3 - 4	1/8"	2	4	8	10
6 - 7	1/4"	2	10	25	15

Figure 45: Terminations dimension in function of nominal size and rope diameter (Geobrugg, s.d.)

After the first load application the tightening torque must be checked and if not fulfilled, adjusted to the required value. (Marchelli M. , 2020)

In addition, “never saddle a dead horse”, this is a manner of speaking into the field of ropes that remember to not place the saddle of the clips on the dead end (side of the rope which is unloaded) instead always place the saddle on the live end (side of the rope that carry the load), as shown in (Figure 46).

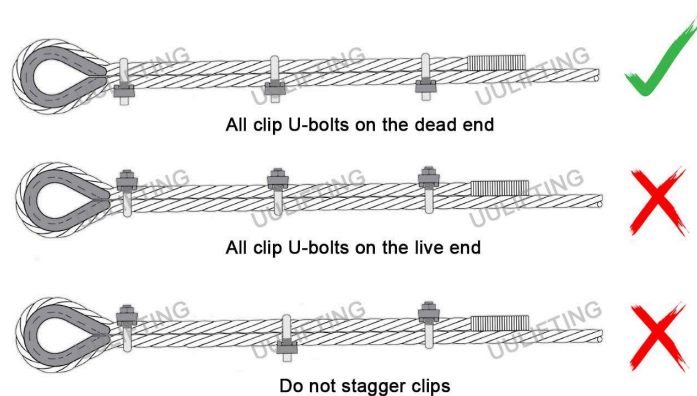


Figure 46: Correct position of U-bolts clip (uu lifting)

Two other aspects that must be always checked are avoiding void at the bottom (Figure 47) and not using inadequate anchor system (Figure 48).



*Figure 47: Presence of void at the bottom (source: Peila D.)*



*Figure 48: Inadequate anchor system (source: Marchelli M.)*

#### **4.1 DATA COLLECTION AND PRELIMINARY ANALYSIS**

To properly design a rockfall barrier some starting information must be known, starting from the knowledge and typology of actions. From propagation analysis (trajectory analysis) it is possible to identify (for each thrown block): velocity, flight/bounce height and trajectory and stopping point. In a probabilistic analysis, a thrown block is the single simulation (signed as “n”) performed. In general N simulations are performed for each potential source point (Figure 49) to account for the variability of the inputs (for example “n” blocks are thrown from each source point): for each simulation the input parameters are chosen within the chosen validity range (probability distribution or, eventually, deterministic value) generating different possible results for each simulation (Figure 50) (Marchelli M. , 2020).

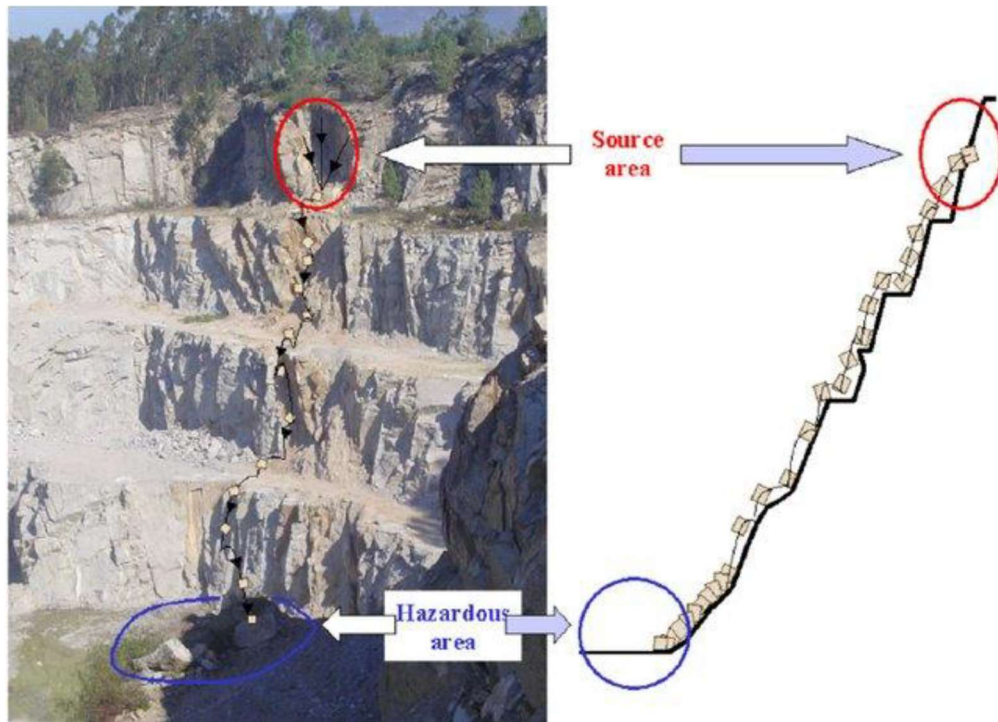


Figure 49: Trajectory scheme highlighting the source and hazardous area (Alejano, Veiga, Castro-Filgueira, Arzua, & Castro-Caicedo, 2017)

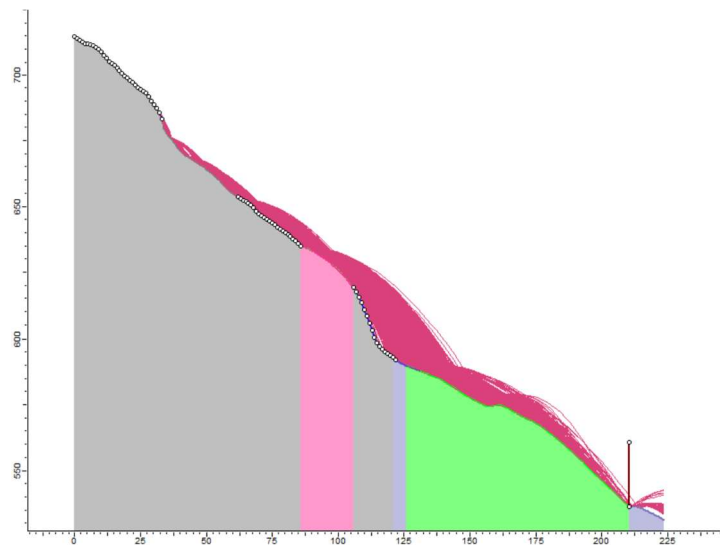


Figure 50: Simulation of "n" thrown block from one source point: showing passed and not passed cases. (Marchelli M. , 2020) produced with RocFall

At each point (x,y,z) of the path, is possible to have:

- percentage of passed blocks;
  - probability of reaching:  $N_{\text{reach}} / N$ ;
- percentage stopped;
- velocity distribution;
- bounce height distribution;
- energy distribution.

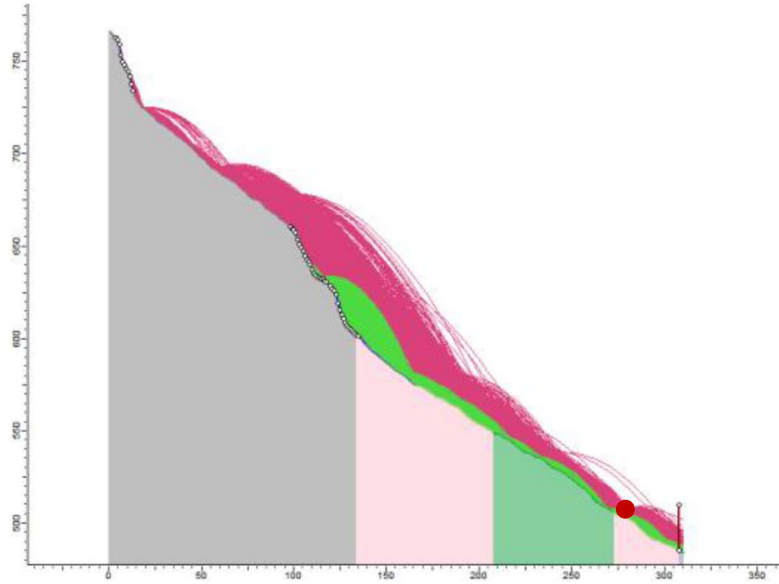


Figure 51: Throw blocks analysis and considered point for the parameters (Marchelli M. , 2020) produced with RocFall

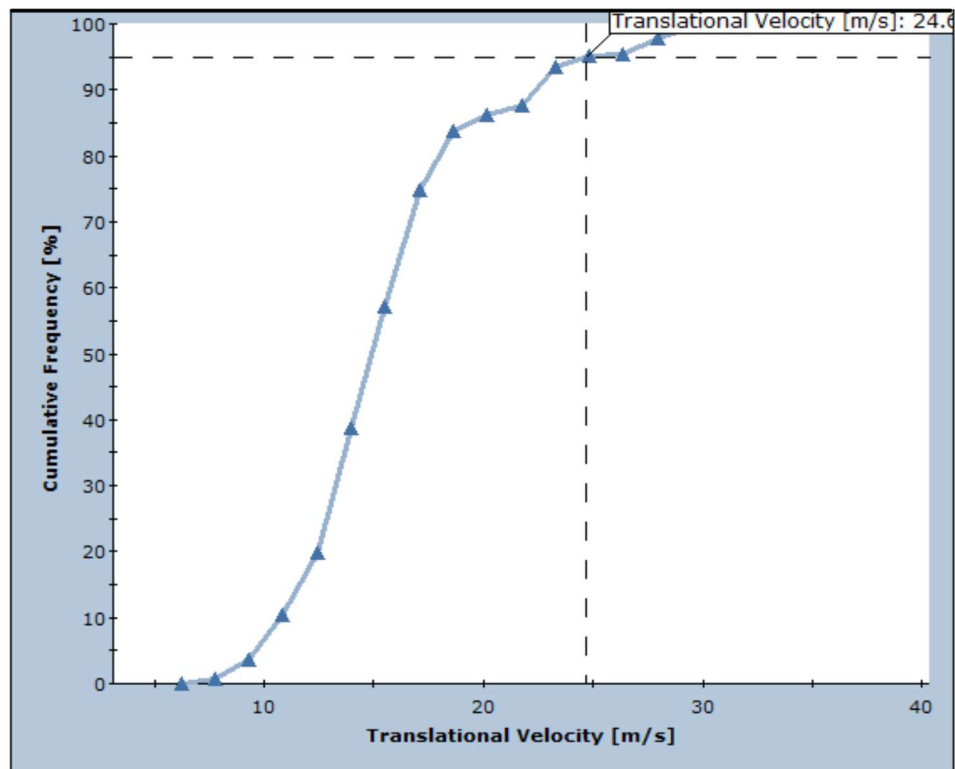


Figure 52: Cumulative frequency chart for the translational velocity parameter (Marchelli M. , 2020) produced with RocFall

Usually, the 95<sup>th</sup> percentile of the distribution of the chosen parameter is represented on the path/slope (Figure 52). This value (or another percentile) is considered representative (characteristic) of the effect of the actions (Marchelli M. , 2020).

This procedure is called semi-probabilistic approach, and is well known in the structure design field, it is called in this way because instead of using a range of value (probabilistic approach) we use a single value, called characteristic value that comes from a probabilistic analysis. It is called characteristic because in order to increase the security of the procedure partial safety factors are introduced. Once the characteristic value is

multiplied by this factor, the design value of the research parameter is obtained. This approach is governed by law and prescription.

- European standards: EN 1997-1;
- Italian law: DM 17/01/2018;
- Italian standards: UNI 11211-4 (2018);
- Austrian standards: ONR 24810 (2021).

The last two are specific for rockfall.

## **4.2 DESIGN AND DIMENSIONING CRITERIA: DIFFERENT STANDARD APPROACH**

References standards are normative that guide the designer through the design, any type of structure, buildings or geotechnical work have its own normative, and depending on the country normative can present small or huge variations. In this chapter are reported two different normative:

- ONR 24810: Technical protection against rockfall. Terms and definitions, actions, design and construction, and monitoring and maintenance: guideline published in its latest update by Austrian Standards institute in 2021.

It is a comprehensive technical guideline focused on rockfall mitigation measures, which not only includes rockfall catchment fences but also many other forms of mitigation including stabilization with anchoring and mesh/nets, embankments, and galleries (Trumer Schutzbauten, s.d.).

- Eurocode 7: Reference Design Code (RDC) for geotechnical design including rock engineering design within European Union (EU).

Its principles have also been adopted by several other countries, becoming a key design standard for geotechnical engineering worldwide. It is founded on limit state design (LSD) concepts, and the reliability of design is provided mainly by a semi-probabilistic method based on partial factors. The use of partial factors is currently an advantage, mainly for the simplicity in its applicability, and a limitation, especially concerning geotechnical designs. (Vagnon, Bonetto, Ferrero, Harrison, & Umili, 2020). Since the application of partial factors to geotechnical design has proven to be difficult another approach can be added; the reliability-based design (RBD).

### **4.2.1 ONR 24810**

The ONR 24810 guides the reader through the initial site investigation through the construction and subsequent maintenance of mitigation measures. The major sections include baseline surveys for planning and determining actions; mitigation specific chapters on anchors, nails, netting, rockfall catchment fences, dams and galleries; monitoring and maintenance; and maintenance tasks. Specifically, for rockfall catchment fences, it has sections dedicated to the verification of the superstructure itself, anchor design, corrosion protection, grouting, non-standard actions, construction rules and lifespan.

As reported from Trumer in Austria, the ONR 24810 must be applied to rockfall related projects which have any of the following aspects:

- deal with hazard assessment;
- planning and implementation of mitigation measures;
- official procedure and expert reports;
- teaching and professional training;

- during the award of public contracts;
- in reference to using other technical standards and guidelines regarding relevant mitigation measures:
- for the allocation of public funding;
- constructions carried out by the Forest Engineering Service in Torrent and Avalanche Control;
- information and public relations.

One of the building blocks of the guideline is the concept of Consequence Class. It is a qualitative rating of the consequences resulting from the failure of mitigation measures with regards to the degree of loss of life, and economic, social or environmental impacts. These classes are borrowed from the European Norm EN 1990:2003 “Eurocode: Basis of structural design”. There are three levels of consequence defined as low, medium or high.

- CC1: Provides the least conservative case for protection. It should only be used where there is a low impact on human life with small or negligible economic, social and environmental effects.
- CC2: Provides a modest case for protection. Normally applied where there is a medium impact on human life with possibly considerable economic, social and environmental effects.
- CC3: Provides the most conservative case for protection. It is applied where there is a high impact on human life with very large economic, social and environmental effects.

Prior to carrying out modeling an appropriate design block needs to be defined. The guideline provides two methods of selecting the design block: a Simplified Approach and a Standard Approach. For the simplified approach, an expert can define the block size based on their experience and information obtained during the site investigation. The standard approach involves carrying out a statistical analysis of measured block sizes in the initiation and/or deposition zones (Trumer Schutzbauten, s.d.).

With ONR 24810 verifications must be carried on: energy, height and anchorage. In addition, performance criteria and construction rules must be checked for a good result of the barrier.

The design energy capacity of the mitigation structure is determined by comparing the design energy (action energy) with the resistance capacity (energy) of the structure. The design resistance value of energy  $T_{R,d}$  is based on the available commercial characteristic energy capacity of a structure  $T_{K,MEL}$  according to ETAG 27 or EAD 340059-00-0106 guidelines reduced by a partial factor of safety according to the consequence class. The partial factor of safety  $\gamma_{T,R}$  is equal to the one for the design action energy (Trumer Schutzbauten, s.d.).



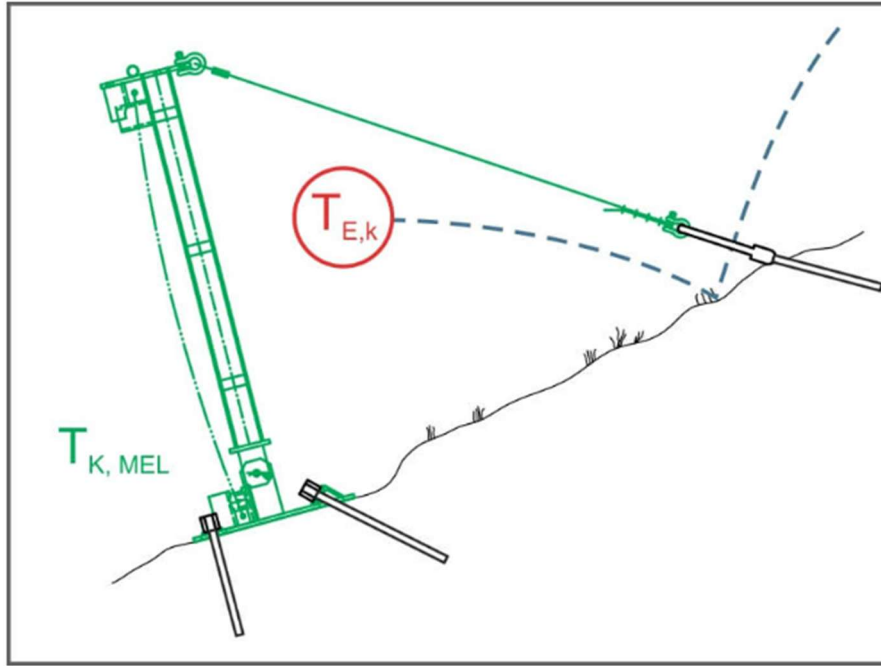


Figure 53: Action energy and Resistance value of energy (Trumer Schutzbauten, s.d.)

The verification that must be respected is shown in Eq (6)

$$T_{E,d} \leq T_{R,d} \quad (6)$$

The design height of the mitigation structure is determined by comparing the design bounce height (action height) with the resistance height of the structure. Various partial factors of safety are applied to compensate for uncertainties in the modeling results (Trumer Schutzbauten, s.d.).

The characteristic value of the height is defined in chapter 4.2. The design value of the height can be computed as reported in Eq (7)

$$h_{E,d} = h_{E,k} \times \alpha_1 \quad (7)$$

$\alpha_1$  is the partial safety factor and is defined in function of the consequence classes, reported in Table 3.

	Consequence Class 1	Consequence Class 2	Consequence Class 3
$\alpha_1$	1,05	1,10	1,30

Table 3: Height partial safety factor

The design resistance height  $h_{R,d}$  in Eq (8) is based on the available commercial characteristic height of a structure ( $h_{R,k}$ ) reduced by a partial factor of safety according to the consequence class (Table 4).  $h_{R,k}$  may only be up to 0,5 m taller than the as tested height of the structure for systems tested below 4 m high and up to 1 m taller for systems tested at 4 m or higher. Systems may never be below the as tested height (Trumer Schutzbauten, s.d.).

$$h_{R,d} = h_{R,k} / \alpha_2 \quad (8)$$

	Consequence Class 1	Consequence Class 2	Consequence Class 3
$\alpha_2$	1,00	1,05	1,10

Table 4: Resistance height partial safety factor

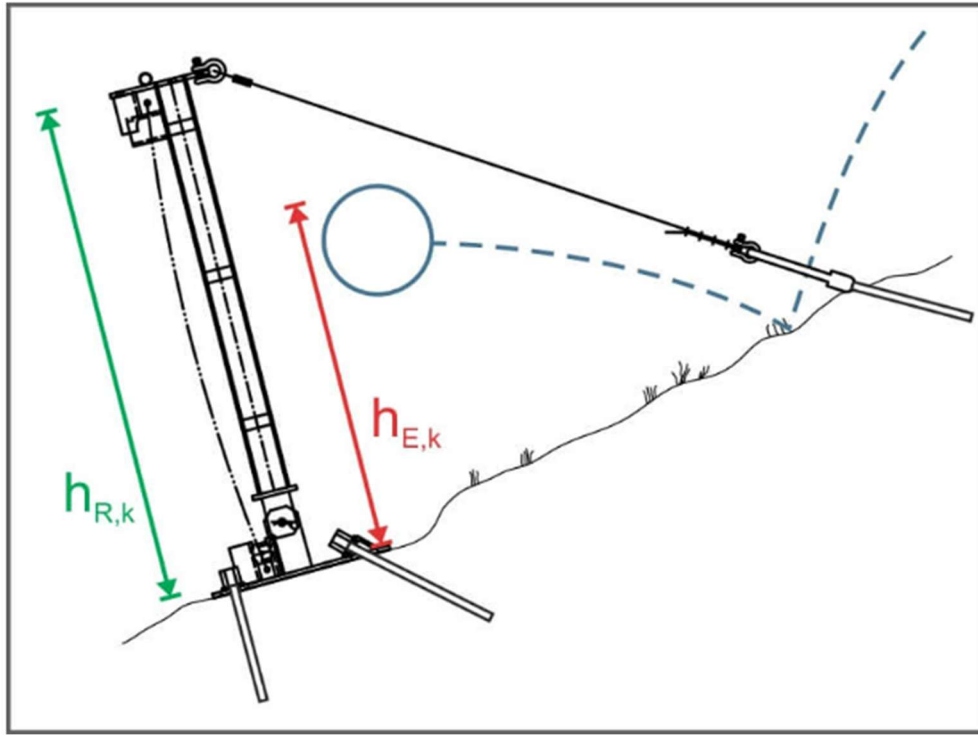


Figure 54: Height and Resistance height (Trumer Schutzbauten, s.d.)

The verification that must be respected is shown in Eq (9)

$$h_{E,d} \leq h_{R,d} \quad (9)$$

The anchors for the structure are verified by comparing the design force (action force) to the resistance capacity of the anchor, in particular the failure of the reinforcement element regarding tensile strength and pull-out capacity. Various partial factors of safety, model factors and distribution coefficients are applied in order to compensate for uncertainties and simplifications due to natural variation (Trumer Schutzbauten, s.d.).

The design value of action force  $E_d$  is equal to the product of the characteristic force ( $E_k$ ) recorded during testing and a partial factor of safety ( $\gamma_E$ ). Eq (10)

$$E_d = E_k \times \gamma_E \quad (10)$$

$\gamma_e$  is fixed and equal to 1,5.



The resistance of an anchor must be calculated for two cases:

1. the resistance of the reinforcement element to failure ( $R_{t,d}$ );
2. the resistance of the anchor to being pulled out of the ground ( $R_{a,d1}$ ).

Reinforcement element resistance is computed through Eq. (11)

$$R_{t,d} = R_{t0,2k} / (\gamma_s \times \eta) \quad (11)$$

Where  $R_{t0,2k}$  is the characteristic value of the steel tensile strength at 0.2% elongation,  $\gamma_s$  is the partial factor of safety equal to 1.15 and  $\eta$  is model factor, function of the consequence class, reported in (Table 5)

	Consequence Class 1	Consequence Class 2	Consequence Class 3
$\eta$	1,30	1,30	1,50

Table 5: Model factor values (Trumer Schutzbauten, s.d.)

Pull-out resistance is computed through Eq. (12)

$$R_{a,d1} = R_{a,k1} / \gamma_{s,t} \quad (12)$$

$\gamma_{s,t}$  is the partial safety factor, function of the consequence class, reported in Table 6

	Consequence Class 1	Consequence Class 2	Consequence Class 3
$\gamma_{s,t}$	1,20	1,20	1,50

Table 6: Pull-out safety factor (Trumer Schutzbauten, s.d.)

While  $R_{a,k1}$  is the characteristic value from anchor pull-out tests reported in Eq. (13)

$$R_{a,k1} = (R_{a,m})_{min} / \xi_2 \quad (13)$$

$(R_{a,m})_{min}$  is the minimum value from anchor pull-out tests, while  $\xi_2$  is a distribution coefficient for micropiles according to the number of anchor pull-out tests, reported in (Table 7)

N° of tests	1	2	3	4
$\xi_2$	1,40	1,20	1,05	1,00

Table 7: Distribution coefficient values

The verification that must be respected is shown in Eq (14)

$$E_d \leq R_d \quad (14)$$

The verifications carried out in the previous steps define requirements according to inputs from hazard analysis in conjunction with data available from manufacture's testing, but nowhere in this process are the effects of an event on the system evaluated. As such, it is suggested that the use of additional performance criteria are applied which are based on information collected during system certification and MEL testing but which are not evaluated or classified under the ETAG 27 guideline or EAD 340059-00-0106 8 (i.e. the appearance of gaps that can open near post locations) (Trumer Schutzbauten, s.d.).

The performance criteria that must be evaluated are function of the consequence class:

- consequence class 1:
  - no additional criteria;
- consequence class 2:
  - no openings in nets close to posts with diameters greater than or equal to 0.4 m;
  - no lateral net openings greater than or equal to 10% of nominal height;
  - no break in the main nets;
  - no break in the bearing ropes;
  - no break in the retaining ropes;
  - a break in the connection of the net to the bearing ropes is permitted ONLY IF a new load-bearing connection forms after the load is applied.
- consequence class 3:
  - no openings in nets close to posts with diameters greater than or equal to 0.2 m;
  - no lateral net openings greater than or equal to 10% of nominal height
  - no break in the main nets
  - no break in the bearing ropes
  - no break in the retaining ropes
  - no break in the cross-sections (strands) of the main net, bearing ropes or retaining ropes.
  - a break in the connection of the net to the bearing ropes is not permitted.

The ONR 24810 also sets out guidelines for the construction of rockfall catchment fences that are meant to ensure the structures are positioned and laid out in a manner that will best ensure their proper functioning. These constructive rules also help reduce efforts for long-term maintenance of the system.

Construction rules are present regarding:

- Minimum distance to elements at risk:  
If the maximum elongation referred to the MEL test is lower than 5m than the minimum distance between a rockfall catchment fence and the protected object is to be 1.2 times, the maximum elongation, reported in Eq. (15) as reported during the MEL test according to ETAG 27 or EAD 340059-00-0106 and shall not be less than one meter greater than the maximum elongation, reported in Eq. (16).

$$D_{min} \geq MEL_{elong} + 1 \quad (15)$$

$$D_{min} \geq MEL_{elong} \times 1,2 \quad (16)$$

- Post Spacing

The spacing between two posts may only have a difference of  $\pm 2.0$  m as shown in (Figure 55)

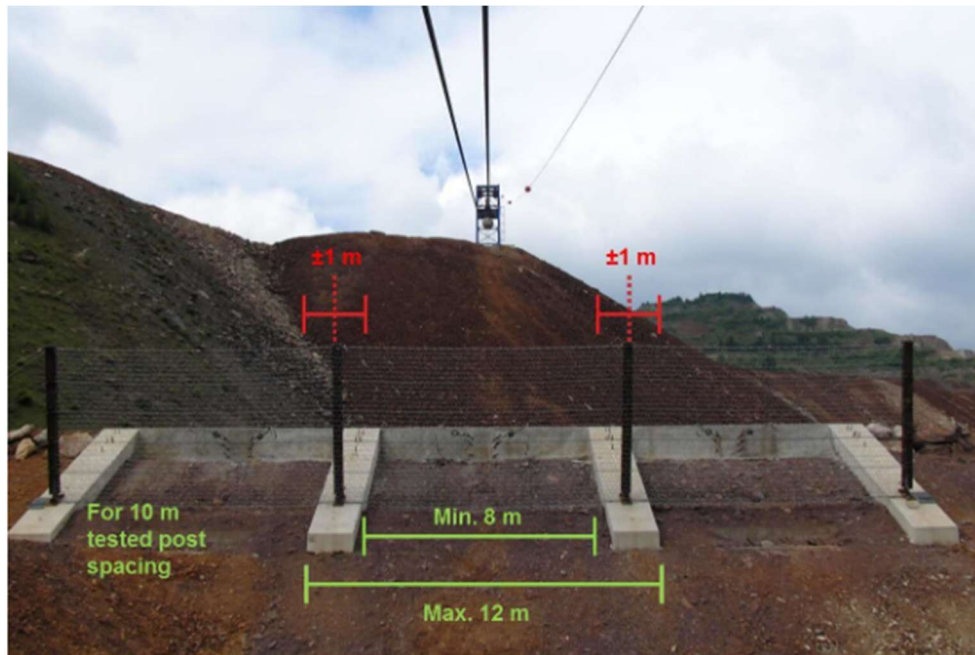


Figure 55: Posts spacing rules (Trumer Schutzbauten, s.d.)

- Row Lengths

The length of a rockfall catchment fence should be kept to a maximum of 60 m. Longer systems require internal anchoring whereby the forces in the bearing ropes can be led to the ground at intervals no longer than 60 m. (Figure 56)



Figure 56: Maximum row length (Trumer Schutzbauten, s.d.)

- Under length system

Systems comprised of less than three fields (i.e. 4 posts) of fencing are not covered by the ETAG 27 or EAD 340059-00-0106 guidelines and are therefore considered special constructions. A qualified expert must carry out the design on a case-by-case basis.

- End fields and overlapping system.

In general, it should be avoided that end fields occur in the hazard zone. However, if this is unavoidable it is necessary to ensure that there are no net openings of more than 10% of the nominal height between the boundary post and the net as tested during an MEL test according to ETAG 27 or EAD 340059-00-0106.

For overlapping rows, the two systems should overlap by a full field length, and the rows must be offset in the fall direction by a minimum distance defined by the MEL elongation. If smaller overlaps are necessary, then the 10% rule is also applied.

All these construction rules are reported from Trumer.

#### 4.2.2 Eurocode 7

The reliability-based design approach deals with the relation between the loads a system must carry and the ability of the system to carry those loads. Both the loads and the resistance may be uncertain, so the result of their interaction is also uncertain. Moreover, the RBD approach enables the non-normal distribution of leading variables in rockfall flow phenomena and their possible correlations to be taken into account. The results of RBD analyses are expressed by the coordinates of the design point,  $x^*$ , and the reliability index, which can be related to the probability of failure,  $P_f$  defined in Eq (17)

$$P_f \cong 1 - \Phi(\beta) = \Phi(-\beta) \quad (17)$$

where  $\Phi$  is the normal cumulative probability function.

Among the available methods for performing reliability analysis, the most widely used and consistent one is the first order reliability method called FORM in which  $\beta$  is given by Eq. (18)

$$\beta = \min_{x \in F} \sqrt{n^T [R]^{-1} n} \quad (18)$$

Where  $x$  is the vector of random variables;  $R$  is the correlation matrix between the random variables;  $F$  is the failure domain, notation “ $T$ ” and “ $-1$ ” represent the transpose and inverse matrix, respectively, and  $n$  is a dimensionless vector defined in Eq. (19)

$$n = \frac{x - \mu^N}{\sigma^N} \quad (19)$$

Where  $\mu^N$  and  $\sigma^N$  are the normal mean and the normal standard deviation vectors, respectively.

As reported from Vagnon, Bonetto, Ferrero, Harrison, & Umili, (2020) in the result of their computation, factor of safety is not used, but is replaced by a reliability index, that represents the probability of failure  $P_f$ . These are linked through the Eq. (17). This is done because values of  $P_f$  can be assigned much more objectively than a factor of safety: for example, society may accept a higher probability of failure for rock slopes in remote mountainous regions than alongside heavily trafficked major roads and rail links.

### 4.2.3 Design parameters for verification analysis

As reported in 4.2.1 , ONR 24810 and UNI 11211-4 require the design values computation of the principal parameters: mass, velocity, kinetic energy and height

The design block mass computation is reported in Eq (20)

$$m_d = m_k \gamma_m \quad (20)$$

Its parameters are expired in (Table 8) reported by (Marchelli M. , 2020)

Parmeter	UNI 11211-4 (2018) (Italy)	ONR 24810 (2021) (Austria)
$m_k = Vol_b \times \gamma$	For $Vol_b$ a cautelative percentile (minimum 95 <sup>th</sup> ) if the blocks potentially impacting the structure is adopted	$Vol_b$ cautelative chosen by the designer (simplified approach) for small/rare events/low consequence class. Otherwise, a fractile $f$ (consequence class and the event frequency class)
$\gamma_m$	$\gamma_m = \gamma_\Psi \times \gamma_{VolF1}$ $\gamma_\Psi$ = function of accuracy of the choice of $\gamma$ $\gamma_{VolF1}$ = function of accuracy of the survey of the design block volume	No coefficient

Table 8: Design mass parameters (Marchelli M. , 2020)

- Regarding the Italian normative:
  - $\gamma_\Psi$  is the coefficient related to the mass evaluation per volume unit of the rock, that can be assumed, generally, equal to 1,00;
  - $\gamma_{VolF1}$  is the coefficient related to precision of survey of the volume of the design block, that can be assumed:
    - = 1,02 for accurate wall surveys (for example using photogrammetric techniques, precision topography, systematic geomechanical surveys on the wall, measurement of the block present on the debris at the base of the walls)
    - = 1,10 if no project survey is performed
- Regarding the Austrian normative:
  - simplified approach is allowed if one of the following conditions is met:
    - less than 100 rocks in the fall deposit zone;
    - less than 100 rocks in the fall start zone;
    - consequence class 1 (CC1);
    - event frequency is less than 1 per year ( $n < 1$ )

The consequence class is defined in chapter 4.2.1.

The event frequency classes are function of the event frequency, the different sections are reported in (Table 9)

Event Frequency Classes	Event Frequency	Fractile for Design Block
EF 4 (very high)	$\geq 10$ events per year ( $n \geq 10$ )	$V_{98}$
EF 3 (high)	1–10 events per year ( $1 < n < 10$ )	$V_{97}$
EF 2 (low)	1 event per year – 1 per 30 years ( $0.03 \leq n \leq 1$ )	$V_{96}$
EF 1 (rare)	1 event per 30 years ( $n \leq 0.03$ )	$V_{95}$

Table 9: Event frequency classes

The design velocity computation is shown in Eq (21), reported by (Marchelli M. , 2020).

$$v_d = v_k \gamma_v \quad (21)$$

Its parameters are expired in (Table 10)

Parmeter	UNI 11211-4 (2018) (Italy)	ONR 24810 (2021) (Austria)
$v_k$	95 <sup>th</sup> percentile of the cumulative distribution from trajectory analysis	Not present
$\gamma_v$	$\gamma_v = \gamma_{Tr} \times \gamma_{Dp}$ $\gamma_{Tr}$ = function of reliability of the input trajectory analysis $\gamma_{Dp}$ = function of accuracy of topography	No present

Table 10: design velocity parameters (Marchelli M. , 2020)

- Regarding the Italian normative:
  - $\gamma_{Tr}$  is the coefficient related to the reliability of trajectory computation, and can be assumed equal to:
    - = 1,02 for rockfall simulation based on coefficient of restitution get from backward analysis
    - = 1,10 for rockfall simulation based on coefficient of restitution based on literature information
  - $\gamma_{Dp}$  is the coefficient that takes into account the quality of topography discretization of the slope, and can be assumed equal to:
    - = 1,02 for slopes discretized with a good precision site characteristic topographic survey
    - = 1,10 for slopes discretized with medium-low precision

The design height computation is exposed in Eq (22), reported by (Marchelli M. , 2020).

$$h_d = h_k \gamma_h \quad (22)$$

Its parameters are expired in (Table 11)

Parmeter	UNI 11211-4 (2018) (Italy)	ONR 24810 (2021) (Austria)
$h_k$	95 <sup>th</sup> percentile of the cumulative distribution from trajectory analysis	95 <sup>th</sup> percentile of the cumulative distribution from trajectory analysis $\pm \frac{1}{2}$ maximum block dimension (from Vol <sub>b</sub> )
$\gamma_h$	$\gamma_h = \gamma_{Tr} \times \gamma_{Dp}$ $\gamma_{Tr}$ = function of reliability of the input trajectory analysis $\gamma_{Dp}$ = function of accuracy of topography	Function of consequence class

Table 11: Design height parameters (Marchelli M. , 2020)

For the coefficient regarding the Italian normative: see the design velocity computation.  
For the coefficient regarding the Austrian normative: see the design block mass computation.

The design block kinetic energy computation is reported in Eq (23)

$$E_d = E_k \gamma_E \quad (23)$$

Its parameters are expired in (Table 12)

Parmeter	UNI 11211-4 (2018) (Italy)	ONR 24810 (2021) (Austria)
$E_k$	Not present	99% of the cumulative distribution from trajectory analysis ( $\frac{1}{2}mv^2$ )
$\gamma_E$	Not present	Function of consequence class

Table 12: Design block kinetic energy parameters (Marchelli M. , 2020)

Partial safety factor  $\gamma_E$  can be evaluated following the ETAG 027 omologation in function of the consequence class, as reported in (Table 13)

	Consequence Class 1	Consequence Class 2	Consequence Class 3
$\gamma_E$	1,00	1,05	1,15

Table 13: Kinetic energy partial safety factor (Marchelli M. , 2020)



To sum up, the two principal parameters must be computed, in function of the following normative, as reported in (Table 14)

UNI 11211-4 (2018) (Italy)	ONR 24810 (2021) (Austria)
$E_d = \frac{1}{2} m_d v_d^2$	$E_d = E_k \gamma_E$
$h_d = h_k \gamma_h$	$h_d = h_k \text{ (with tollerance)} \gamma_h$

*Table 14: Design height and design kinetic energy in function of the chosen normative (Marchelli M. , 2020)*

#### 4.2.4 Performance evaluation of the product through real scale test: codified impact tests

To analyze the performance of the barrier two parameters must by computed:

1. height: by intercepting the block;
2. absorbable energy level: by stopping the block with the barrier in safe condition (Figure 57)



*Figure 57: intercepted block in safe condition for real scale test (Marchelli M. , 2020)*

##### 4.2.4.1 Walenstadt vertical drop impact test

In 2001, a guideline was published in Switzerland that represented the first attempt worldwide of an official certification of flexible rockfall protection system. All type testing of barrier system was conducted by the Swiss Federal Institute for Forest, Snow and Landscape Research (WSL). Testing took place at ESL's testing site in Walenstadt, Switzerland. After successful test, a certificate was issued by the Federal Office for the Environment (FOEN), grouped into Energy classes 1-9 according to the tested maximum impact energy ranging from 100-5000 kJ (Marchelli M. , 2020).





Figure 58: Walenstadt vertical drop impact test instrumentation and configuration (Marchelli M. , 2020)

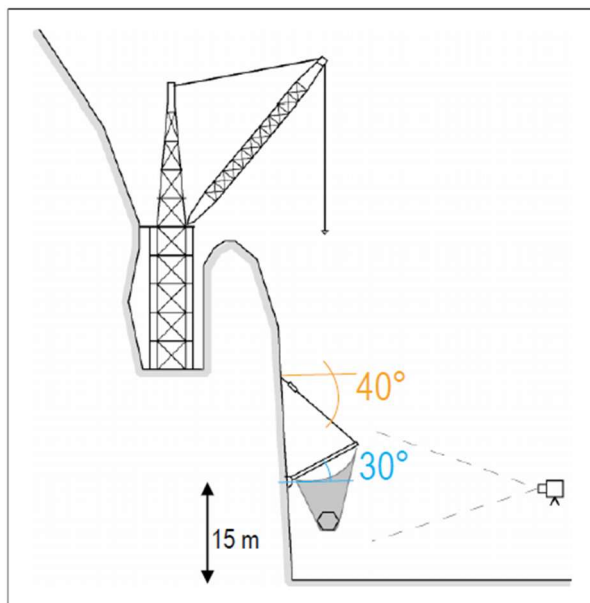


Figure 59: Walenstadt vertical drop impact test: geometrical configuration for the barrier (Marchelli M. , 2020).

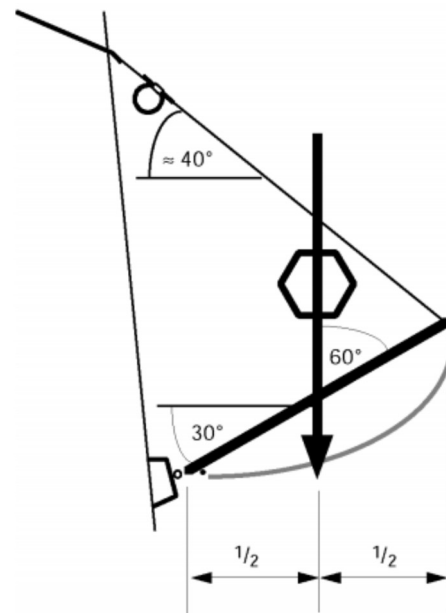


Figure 60: Walenstadt vertical drop impact test: geometrical configuration for the impact

Swiss Agency for the Environment, Forests and Landscape (SAEFL) gives guideline for the approval of rockfall protection kits (Figure 59 and Figure 60).

#### 4.2.4.2 Falling rock protection kits (ETAG 027)

The European Organization for Technical Approvals (EOTA), in order to realize a more realistic scheme, endorsed a new European technical approval guideline: “Falling rock protection kits” (ETAG 027) (now called EAD 340059-00-0106 (2018)), where a testing procedure for the technical assessment of the fitness for use and for CE marking of a net fence (which has been called falling rock protection KIT In the guideline) has been defined (Marchelli M. , 2020).

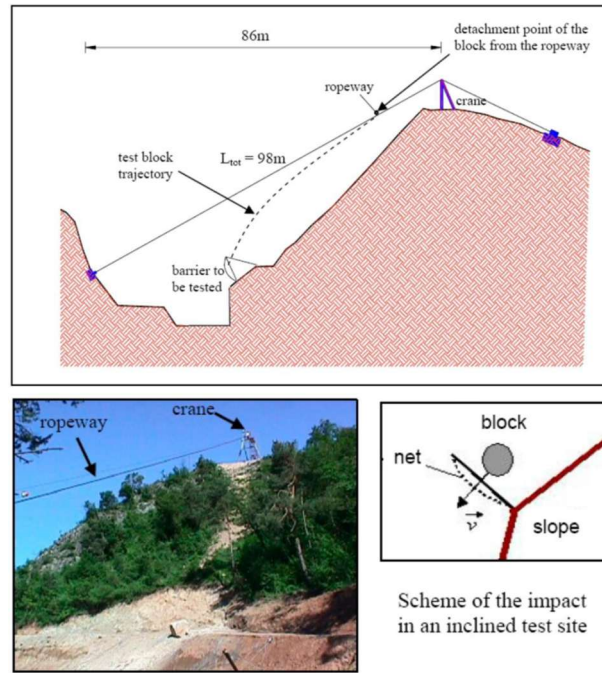


Figure 61: Scheme of the impact in an inclined test site (Peila & Ronco, 2009)

EAD 340059-00-0106 (2018) identifies relevant and mandatory characteristics of the net fences and the threshold values that have to be respected for technical reasons, establish a method for the verification and assessment of these characteristics and define the relevant identification tests for the kit components. The test site is a structure, which shall be able to accelerate a concrete block (Figure 63) to the test speed and to impact it onto the net fence, with the necessary precision (Figure 62). The slope downhill to the kit is at least parallel to the block trajectory in the last meter before the impact (Marchelli M. , 2020).

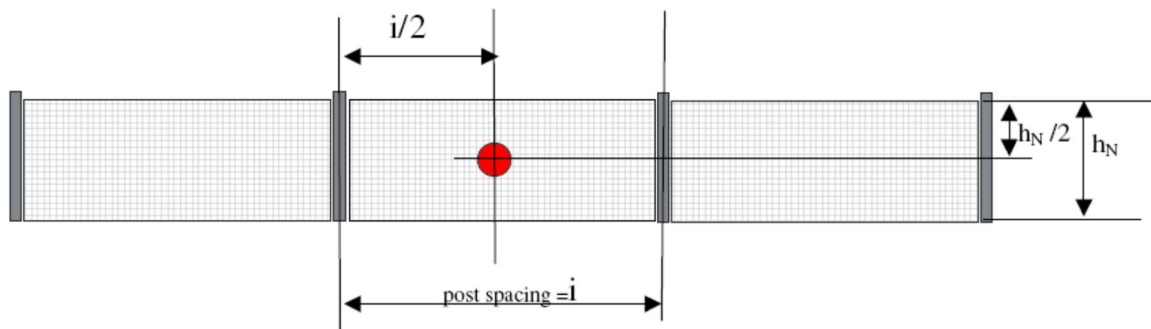


Figure 62: Location of impact (Marchelli M. , 2020)

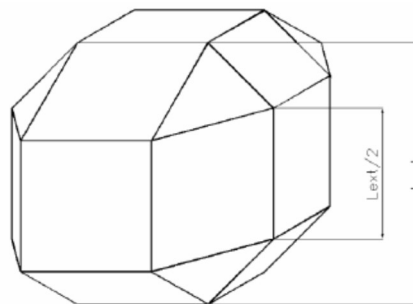


Figure 63: Block geometry and dimensions (Marchelli M. , 2020)

The tested fence must be composed by three functional modules and four posts (Figure 62); while the block is made of plain or reinforced concrete and its shape is a polyhedral (Figure 63).

To compute the energy absorption capacity two different parameters that come out from this test, can be used:

1. The SEL (Service Energy Level) of a falling rock protection kit. SEL is the kinetic energy of a regular block impacting the net fence (impact against the net at a speed non lower than 25 m/s) which guarantee that the barrier stops the block after two impacts at the same kinetic energy and that after the first impact, the block is stopped by the kit, there are not ruptures in the connection components, the openings if the mesh are smaller than two times the initial size of the mesh. The residual height of the kit after the impact (the minimum distance between the lower and the top rope or the upper part of the mesh, measured orthogonally to the reference slope after the test without removing the block) is higher or equal to 70% of the nominal height of the kit before the test. In addition, the net fences of the barrier must be able to stop the block after the second impact (Marchelli M. , 2020).
2. The MEL (Maximum Energy Level) of a falling rock protection kit. MEL is the kinetic energy of a regular block impacting the net fence (impact against the net at a speed no lower than 25 m/s). During this test the maximum displacement of the structure and the forces on the foundation are measured. The MEL must fulfill the following constraint:
  - a)  $MEL > g \times SEL$ ;
  - b) the barrier stops the block;
  - c) the block, during the impact, does not touch the ground, until the kit reaches the maximum elongation.

Energy level classification	0	1	2	3	4	5	6	7	8
SEL [kJ]	–	85	170	330	500	660	1000	1500	>1500
MEL [kJ]≥	100	250	500	1000	1500	2000	3000	4500	>4500

Figure 64: Energy level classification in function SEL/MEL (Marchelli M. , 2020)

Category	Residual height
A	≥50% nominal height
B	30<nominal height<50%
C	≤30% nominal height

Figure 65: Falling rock protection kit categories derived by evaluation of MEL residual height (as used in ETAG 027) (Marchelli M. , 2020)

#### 4.2.5 CE marking

CE marking is a certification mark that indicates conformity with health, safety, and environmental protection standards for products sold in the European Economic Area (EEA).

The EAD or ETAG (European Technical Approval Guidelines) is the documentation of the accepted methods and criteria in EOTA applicable for the assessment of the performance of a construction product in relation to its essential characteristics. EAD is developed in all cases where the assessment of a construction product is or not fully covered by a harmonized technical specification (Regulation (EU) No 305/2011). The EOTA

coordinates the application of the procedures established for a request for a European Technical Assessment (ETA) and for the procedure adopting a European Assessment Document (EAD). It contains at least:

- a general description of the construction product and its intended use;
- the list of essential characteristics relevant for the intended use;
- the methods and criteria for assessing the performance of the product;
- the principles for the applicable factory production control.

The European Technical Assessment (ETA) is the documented assessment of the performance of a construction product, in relation to its essential characteristics. It is a voluntary document that contains the performance of the essential characteristics of a construction product and is issued when, in the absence of harmonized standards, a European Assessment Document (EAD) is available as a reference or a document of methods and criteria for assessing performance in relation to the essential requirements (Marchelli M. , 2020).

The ETA is the basis for a declaration of performance (DoP) that the manufacturer is obliged to draw up in accordance with the Construction Products Regulation (CPR) before marking his product with the CE marking. The CE marking allows the manufacturer to freely place his product on the European internal market (Marchelli M. , 2020).

Manufactures are obliged to qualify their materials and exhibit a Declaration of Performance (DoP) and the relevant CE marking, issued on the basis of an ETA (or the Technical Assessment Certificate issued by the President of the Superior Council of Public Works (C.S.LL.PP.), after preliminary investigation by the Central Technical Service (STC), also on the basis of Guidelines approved by the Superior Council of Public Works. The construction manager has the duty, during acceptance at the worksite, to verify the prescribed qualification documentation; in particular, no products may be used in the works that are not accompanied by the documentation of the qualification materials (Marchelli M. , 2020).

### **4.3 CONSIDERATION FOR EXTREMELY HIGH LOAD CASE**

The main goal of the standardizing guidelines, previously described, is to clearly define the load cases a structure has to withstand. However, a consequence of this is that special and extreme load cases are mostly neglected, for example in areas with very high slopes or cliffs where this can happen. In particular high speed rockfall can create puncturing effects on the net structure that are not observed using slower and bigger impacting rocks, even if the energy level is the same. The same effect also appears with falling trees where the log can be heavy (comparable to falling rocks), but the impact area is quite small as trees tend to slide down a slope, hitting the barriers with their tip. (Volkwein, Roth, Gerber, & Aron, 2009)

In the guidelines described in chapter 5.2.1, the load case rockfall is defined as the impact of a single boulder with a certain kinetic energy selected from an array of energy classes. This in turn defines the retention capacity of the respective rockfall barrier. The impact energy  $E$  of the falling rock is obtained from its mass (kg) and impact velocity (m/s). Hence, the required energy class can be obtained by changing one of these factors, resulting in quite a variety of possible testing conditions. To reduce this variety, the impact velocity is set at 25 m/s (typical value of Alpine region). High cliffs and steep slopes provide large free-fall distances to falling rocks, potentially increasing their maximum speed enormously. Reckoning the energy level, this reduces the impact mass by factor 7,4 compared to a standard impacting body according to the guidelines. Because of the thereby reduced volume of the boulders, the so-called bullet-effect becomes evident: The total energy of falling rock has to be absorbed by a smaller impact area of the flexible net structure (Figure 66) (Volkwein, Roth, Gerber, & Aron, 2009).





Figure 66: High-speed rockfalls can create high energies with quite small blocks and could puncture protection barriers loading smaller impact areas (Volkwein, Roth, Gerber, & Aron, 2009)

Field tests with high free-falling heights are difficult to perform because targeting structure at predefined impact location becomes increasingly unlikely. Consequently, numerical simulations must enhance the knowledge on the interaction between high-speed rockfalls and flexible barriers. Comparative calculations for an impact energy of 3000 kJ were performed using the mass/velocity impact combinations 9640 kg/25 m/s and 1300 kg/68 m/s for spherical boulders made from reinforced concrete; the latter combination would require a free-falling height of 230 m neglecting the air resistance. This study showed that the maximum net load increased by 90–130%. However, the maximum load of the supporting structure consisting of steel posts, ropes and energy absorbers was reduced by 15–30% for the high-speed events (Figure 67) (Volkwein, Roth, Gerber, & Aron, 2009)

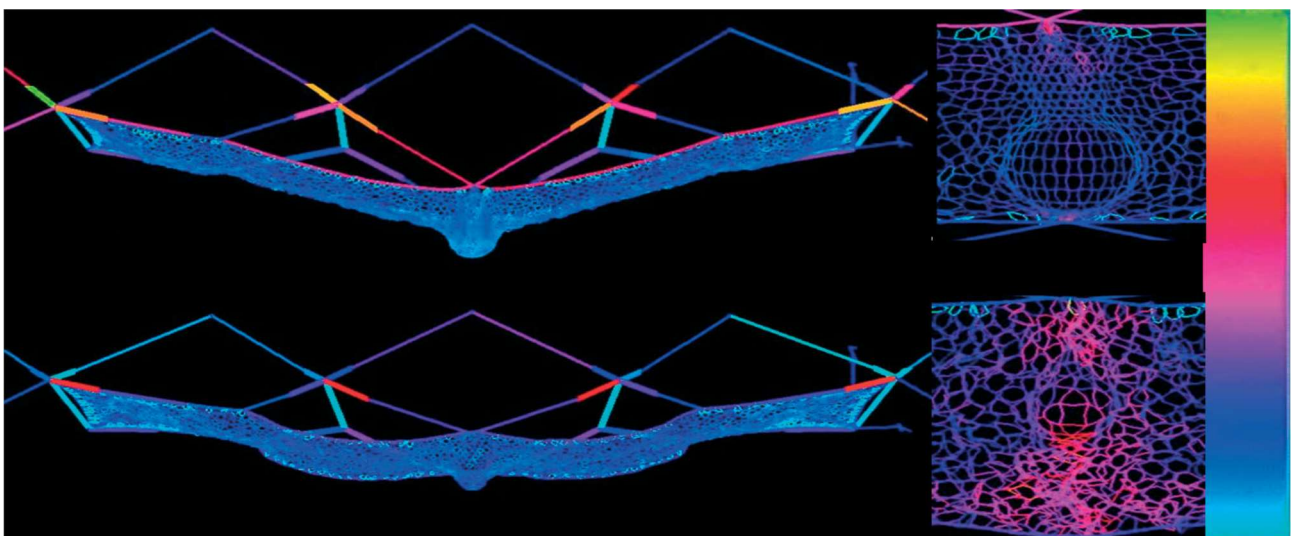


Figure 67: Different loading percentage of a rockfall barrier due to a “slow and large” Swiss standard test specimen (top) and a small high speed rockfall event (bottom). Details of impact area utilization are displayed on the right. The fast event loads the impact area higher, but the superstructure less (Volkwein, Roth, Gerber, & Aron, 2009)

This shows that the surrounding superstructure of a protection net is loaded less by smaller high-speed rockfall events having the same energy level as large and slower boulders. The net itself, however, is loaded more in the impact area by small high-speed boulders (Figure 67). Therefore, the mass ratio between barrier and the falling object has a large influence on the dynamics and the stresses within the barrier. An additional consideration of the impulse  $p = mv$  would compensate for this deficiency, since the velocity is not squared (Volkwein, Roth, Gerber, & Aron, 2009).

	Tree B	Tree C	Boulder
Mass	1600 kg	2080 kg	1600 kg
Dimension	Φ0,49m , 10 m	Φ0,39 m, 20m	0,88m cube
Front face dimension	Φ < 0,3m	Φ < 0,3m	0,88m x 0,88m
Falling height	20m	30m	32m
Impact velocity	20m/s	24m/s	25m/s
Impact energy	314kJ	612kJ	512kJ
Braking distance	4,5m	6,0m	4,2m
Total energy absorbed	385kJ	735kJ	577kJ
Upslope anchor rope	72kN	112kN	92kN
Top support ropes	220kN	226kN	174kN
Bottom support ropes	184kN	202kN	174kN
Lateral anchor ropes	158kN	152kN	124kN

*Table 15: Comparison of maximum loads within protection barrier for tree and boulder*

To deal with extremely high-speed cases a selection of non-unified loads is presented. It is shown from Volkwein, Roth, Gerber, & Aron, (2009) that it is possible to use typical flexible rockfall barriers for extreme loads, such as high-speed rockfalls, falling trees, snow slides or others. This is only the case when systems approved according to the existing testing guidelines show sufficient capacity reserves after a standard test. If not, accordant field tests or numerical models become necessary, which allow the design of systems according to specific and individual project conditions.

#### 4.4 ROCKFALL SIMULATION WITH NUMERICAL SOFTWARE

The rockfall simulation is a powerful tool that can give to designer additional information regarding the design parameters such as kinetic energy or height. When in-situ tests are not possible this analysis is strongly recommended. To highlight the importance of numerical simulation, and its reliability, research of (Koo & J.S.H., 2014) is reported. In their study, rockfall and landslide debris impacts are simulated by punching and areal loads respectively. Numerical simulations are carried out using three-dimensional non-linear finite element numerical package LS-DYNA.

A first study is conducted from (Koo & J.S.H., 2014) to demonstrate that the program LS-DYNA is an appropriate tool for the analysis of flexible rockfall structures. To do this, the behavior of horizontal flexible rockfall net simulated by Arup (2013) is validated against the experimental results of the rockfall test reported by Volkwein (2004).



Rockfall experiments were conducted in the early 2000s. The test setup, illustrated in (Figure 68 and Figure 69) featured a flexible barrier panel measuring  $3.7 \text{ m} \times 3.7 \text{ m}$ . The ring net was positioned horizontally and supported by four cables. The barrier had an energy capacity of 550 kJ. During the tests, it was struck by a spherical projectile with a diameter of 0.82 m and a mass of 825 kg, released vertically from various drop heights.



Figure 68: The specifically built Test Rig for Rockfall Tests, Front View (Koo & J.S.H., 2014)

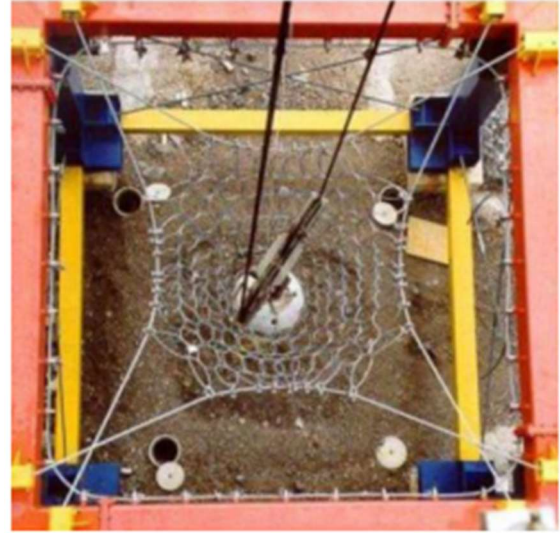


Figure 69: The specifically built Test Rig for Rockfall Tests, Plan View (Koo & J.S.H., 2014)

Figure 70 presents the numerical model set-up in LS-DYNA. The test simulation was performed with a 16m drop height and results were analyzed at four different times:  $t = 0$  seconds,  $t = 0.1$  seconds,  $t = 0.2$  seconds and  $t = 0.3$  seconds.

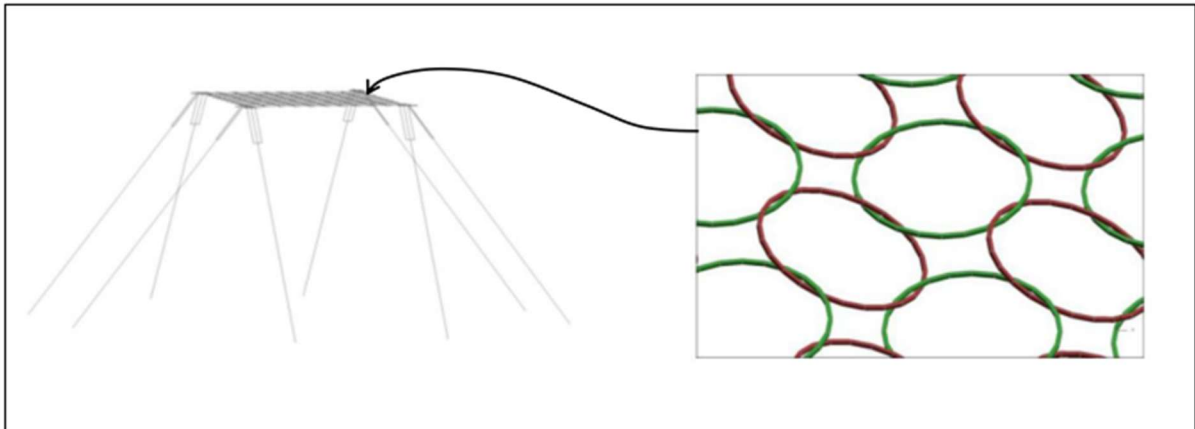


Figure 70: (Left) Structural Model set-up in LS-DYNA and (Right) Ring Net Model (Koo & J.S.H., 2014)

Through this first test the validation of the software was verified. A series of numerical simulations were performed to evaluate the behavior of Volkwein's net under both punching and distributed impact loads. To generate various loading conditions, drop weights with different geometries—namely a single sphere, a group of four spheres, and a rigid slab—were employed. The setup and parameters used for these simulations are summarized in (Table 16) (Koo & J.S.H., 2014).

Simulation No.	Drop Weight	Dimension	Contact Area	Impact Velocity (m/s)	Kinetic Energy (kJ)
1	Single sphere	0,82m diam.	5% of the barrier panel	14,9	90
2				18,6	143
3				22,7	215
4				27,2	309
5				31,9	425
6				36,6	559
7	Four spheres	Each sphere: 0,82m diam.	20% of the barrier panel	14,9	90
8				18,6	143
9				22,7	215
10				27,2	309
11				31,9	425
12				36,6	559
13	Rigid slab	Each sphere: 0,6m diam.  Slab: 3m by 3m	70% of the barrier panel	14,9	90
14				18,6	143
15				22,7	215
16				27,2	309
17				31,9	425
18				36,6	559

Table 16: Simulation Schedule of the parameters for study of horizontal net (Koo & J.S.H., 2014)

Figure 71 illustrates the vertical acceleration and displacement time histories obtained from Simulation No. 3 for the single-sphere impact case. The model represents the free fall of the drop weight. Prior to contact with the barrier, the vertical acceleration ( $a$ ) of the drop weight was  $-9.81 \text{ m/s}^2$ , indicating motion in the downward direction. Upon impact with the barrier (time  $t = 0 \text{ s}$ ), the barrier exerted an upward reaction force, causing the acceleration to rapidly shift from negative to positive. The downward movement of the drop weight continued until it was momentarily brought to rest, corresponding to the point of maximum upward acceleration. Subsequently, the weight rebounded upward, after which its acceleration returned to  $-9.81 \text{ m/s}^2$  as it moved freely again. The LS-DYNA simulation results indicate that the entire impact event occurred over a duration of approximately 0.3 seconds. (Koo & J.S.H., 2014). This process describes even what happens in the real case.

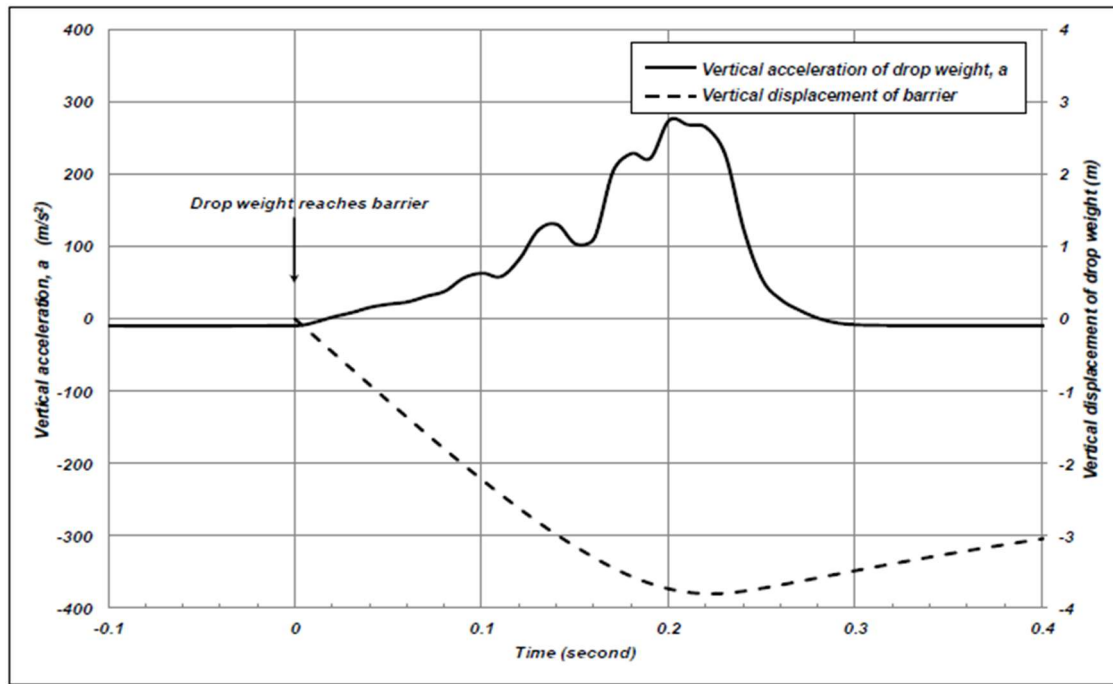


Figure 71: Vertical acceleration and displacement of the drop weight in simulation No. 3 (Koo & J.S.H., 2014)

Simulation carried from (Koo & J.S.H., 2014) shows that the maximum acceleration is reached by the rigid slab case, in accordance with this, slab is even the case that shows the shortest time for stopping. This demonstrates fallen bodies with higher acceleration are going to be stopped in less time.

The upward force exerted by the barrier on the drop weight can be determined from the measured accelerations of the drop weights. Figure 72 presents the peak upward forces obtained from various numerical simulations. According to the principle of action and reaction, these upward forces correspond to the vertical reactions acting at the foundation of the test rig. It is assumed that the energy losses due to friction between the barrier's movable components are negligible compared to the total impact energy. The simulation outcomes suggest that the foundation reaction force increases with the kinetic energy or equivalently, with the impact velocity of the drop weight (Koo & J.S.H., 2014).

The data in Figure 72 also shows that the rigid-slab resulted in higher foundation load compared with the other drop weights. The single sphere drop weight induced the smallest foundation load. The difference in the calculated foundation load produced by the rigid-slab and the single-sphere is 36% on average, (Koo & J.S.H., 2014).

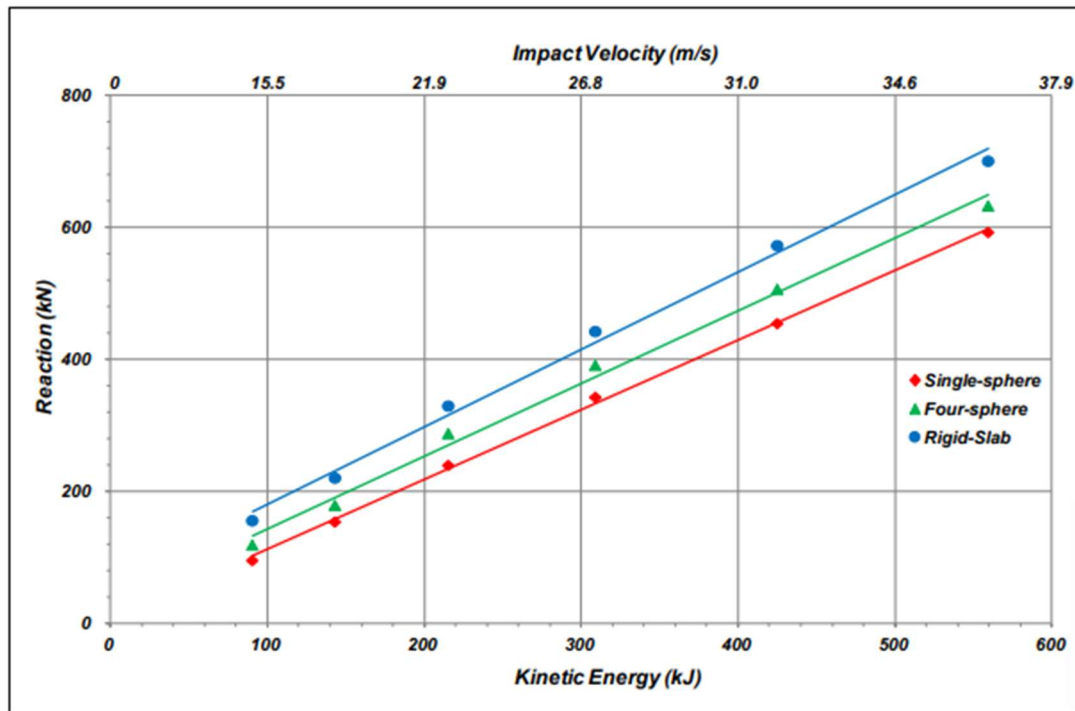


Figure 72: Reaction of horizontal net against impact velocity and kinetic energy (Koo & J.S.H., 2014)

The LS-DYNA results show that landslide debris impact may induce a higher barrier foundation load compared with that induced by rockfall impact for identical kinetic energy levels of the impacts. As also shown from (Volkwein, Roth, Gerber, & Aron, 2009).

Figure 73 presents the cable forces obtained from the numerical simulations. The results indicate that the forces in the cables do not vary significantly with different types of drop weights. According to Wendeler (2013), the cable forces generated by rockfall or landslide impacts of the same energy level may be comparable if the cables are equipped with energy-dissipating devices. This is because the forces developed in the cables are primarily governed by the load–deformation behavior of the energy-dissipating elements. (Koo & J.S.H., 2014)

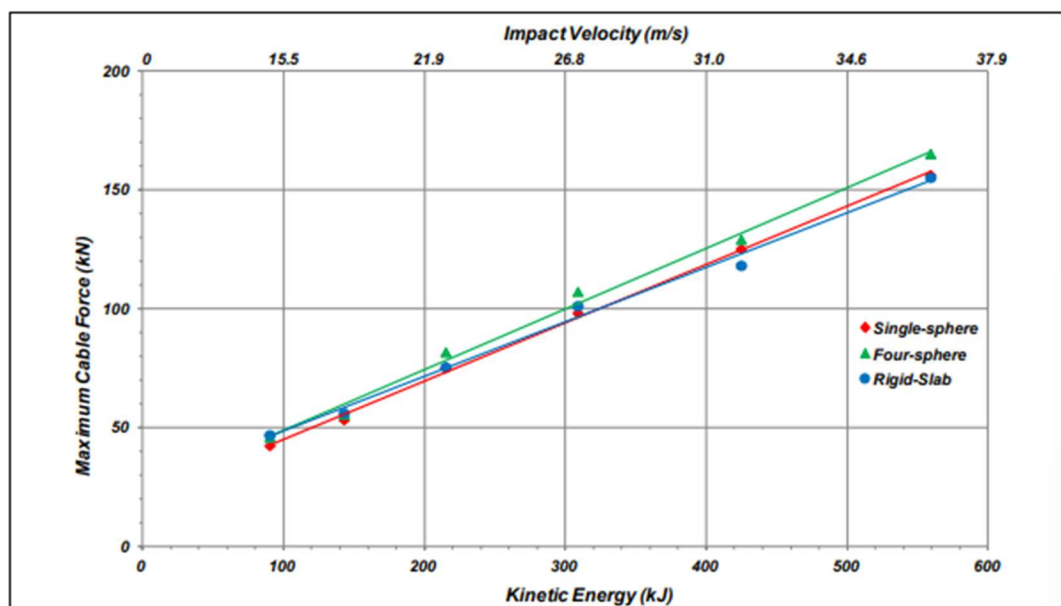


Figure 73: Cable force against impact kinetic energy.

The upward force acting on the drop weights corresponds to the vertical component of the cable forces. If the cable is inclined at an angle  $\theta$  relative to the horizontal, the vertical component of the force can be calculated as the product of the total cable force and  $\sin \theta$ . This angle increases with the increasing of the kinetic energy and so with greater or faster elements. Figure 74 shows, how  $\theta$  change for the three different cases analyzed with LS-DYNA from Koo & J.S.H., (2014).

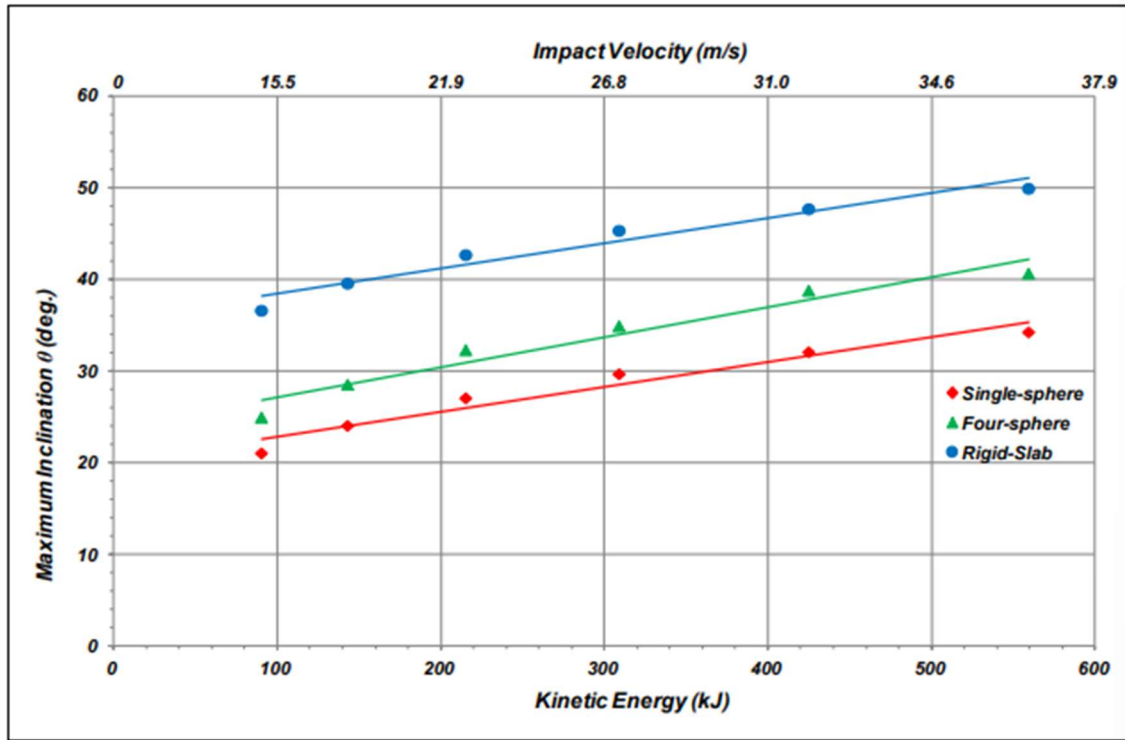


Figure 74: Maximum inclination of cables against impact velocity and kinetic energy (Koo & J.S.H., 2014)

Field observations of flexible debris-resisting barriers indicate that landslide debris tends to impact a larger area of the barrier, causing smaller and less localized deformations compared to rockfall impacts. It was suggested that landslide debris generally represents a less severe loading scenario for the barrier netting. This aspect is confirmed from tests carried out with LS-DYNA simulation into the (Koo & J.S.H., 2014) study.

The previously discussed results refer to a rockfall net positioned horizontally. In real-world applications, however, flexible rockfall barrier systems are typically installed vertically or at a sub-vertical angle, with steel posts stabilized by uphill and/or lateral cables. To investigate the behavior of a vertical flexible rockfall barrier under both punching and distributed loads, additional LS-DYNA simulations were conducted. The simulation adopted the LS-DYNA model developed by Ng et al. (2012), representing a 3,000 kJ proprietary flexible rockfall barrier system. The model included a barrier 5 m in height, composed of five panels each 10 m wide (Figure 75). Double cable ropes ran along the top and bottom of the barrier and were anchored at both ends. The posts supporting the top cable and the net were stabilized using tie-back retention cables, and the post-to-foundation connection was modeled as a pin joint. Energy-dissipating devices were integrated along the cables. Further details of the numerical model can be found in Ng et al. (2012), while the simulation parameters are summarized in

Table 17) (Koo & J.S.H., 2014).

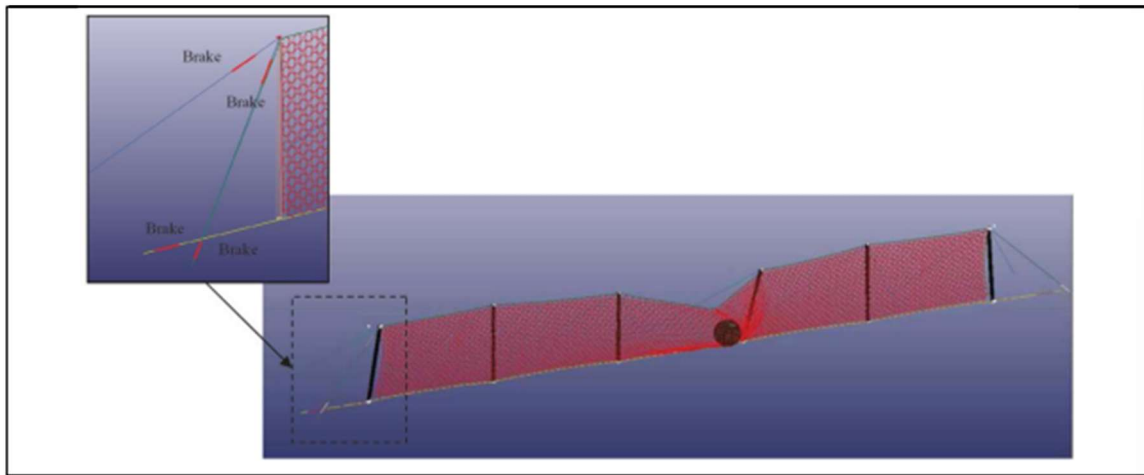


Figure 75: Flexible rockfall barrier system subjected to impact of a single sphere. (Koo & J.S.H., 2014)

Simulation No.	Impact weight	Dimension	Impact velocity (m/s)	Kinetic energy (kJ)
F1	Single sphere	2,0 m diameter	37	3.000
F2	Rigid slab	Each sphere: 1,0 m diameter	37	3.000
		Slab: 7m by 4m		

Table 17: Parameters for the simulation of the vertical net. (Koo & J.S.H., 2014)

The LS-DYNA simulations indicate that the flexible rockfall barrier successfully arrested both the single-sphere and rigid-slab impactors. The intermediate posts connected to the impacted net panels exhibited forward deflection. Table 17 presents the horizontal acceleration and displacement histories of the impact weights. The moment of contact with the barrier was defined as time 0.0 s. From that instant, the impactors experienced resistive forces from the barrier and began to decelerate. The peak decelerations recorded were 195 m/s<sup>2</sup> for the rigid slab and 134 m/s<sup>2</sup> for the single sphere. According to Newton's second law, this corresponds to the rigid slab experiencing approximately 40% more resistance from the barrier than the single sphere. Conversely, the single-sphere impact produced a larger net deformation, with maximum horizontal displacements of 6.3 m and 5.1 m for the single sphere and rigid slab, respectively (Koo & J.S.H., 2014).

Key results including cable forces and post reactions of the two simulations are summarized in Table 18. Physical rockfall tests had been conducted for the proprietary rockfall barrier simulated in the LS-DYNA analysis in accordance with ETAG 27 requirements. Results of the physical test indicate that the maximum cable force induced by a 3,000 kJ rockfall impact was up to 293 kN and the maximum force in the uphill retention cable was 83 kN. These are comparable with the results of the single-sphere simulation. The results of simulations could be further improved by adopting the exact barrier set-up, such as the orientation of the barrier posts, dimensions of panels and impact direction of single sphere used the physical rockfall test (Koo & J.S.H., 2014).



	Single sphere	Rigid slab	Difference
Top cable force	225 kN (per cable rope)	242 kN (per cable rope)	+8%
Bottom cable force	117 kN (per cable rope)	152 (per cable rope)	+30%
Uphill retention cable force	60 kN (per cable rope)	65 kN (per cable rope)	+8%
Shear at post foundation	190 kN	259 kN	+36%
Vertical reaction at post foundation	181 kN	150 kN	-21%
Deflection angle of cable ( $\theta$ ) (see Figure 76)	30°	50°	+67%

Table 18: Ket results - Maximum forces, Cable inclination and Barrier deformation (Koo & J.S.H., 2014)

In the rigid-slab impact simulation, the maximum shear force at the post foundations was approximately 40% higher than that observed for the single-sphere impact. This aligns with the findings presented earlier in this chapter, indicating that, compared to a single-sphere impact, a rigid-slab impact can generate a more critical barrier foundation load in the direction of impact. The post foundation shear corresponds to the horizontal component of the cable force acting on the barrier posts and is influenced by the cable deflection angle. A larger angle between the cable and the post results in a higher post foundation shear (see Figure 76 and Table 18) (Koo & J.S.H., 2014).

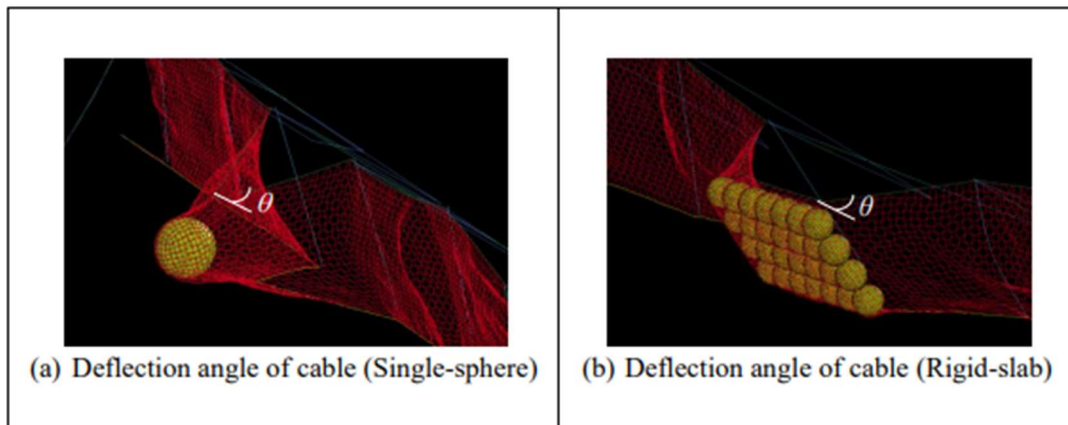


Figure 76: Deflection angles of cables (Koo & J.S.H., 2014)

The forces and bending moments acting on the barrier posts are summarized in Table 19. LS-DYNA simulations indicate that the bending moments induced by areal and punching impact loads are of a similar magnitude, whereas the axial load on the posts tends to be lower under areal impact conditions (Koo & J.S.H., 2014).

	Single sphere	Rigid slab	Difference
Maximum bending moment in posts	36 kNm	40 kNm	+11%
Maximum axial compressive load in posts	285 kN	229 kN	-24%

Table 19: Maximum bending moments and axial forces in barrier posts (Koo & J.S.H., 2014)

The reported studies show that the two rockfall structures could withstand the impact of the rigid slab and the punching impact load. The difference of the two falling cases are reported in chapter 4.2.4 and found similar in this simulation analysis. Another important aspect is that, since the physical test and simulation give results in the same order, the simulation could be used as a strong tool to analyze specific cases where the physical tests are not possible, giving realistic results as outputs.



## 5 DEGRADATION OF ROCKFALL BARRIER

To discuss the degradation of rockfall barriers, an overview of the corrosion of metallic materials, and in particular of steel, must be provided. Rules and directions about this aspect are given from the EN ISO: European Normative, International Organization for Standardization, which produce normative in accordance with IEC: International Electrotechnical Commission.

As reported from BSI (British Standard Institution), that co-produce the normative, metals, alloys and metallic coatings can suffer atmospheric corrosion when their surfaces are wet. The nature and rate of the attack depend upon the properties of surface-formed electrolytes, particularly with regard to the level and type of gaseous and particulate pollutants in the atmosphere and to the duration of their action on the metallic surface.

The character of the corrosion attack and the corrosion rate are consequences of the corrosion system, which comprises the metallic materials, the atmospheric environment, technical parameters and operation conditions. The corrosivity category is a technical characteristic which provides a basis for the selection of materials and protective measures in atmospheric environments are subject to the demands of the specific application, particularly regarding service life. The corrosivity categories are defined by the first-year corrosion effects on standard specimens as specified in ISO 9226. The corrosivity categories can be assessed in terms of the most significant atmospheric factors influencing the corrosion of metals and alloys. (BSI, 2012)

The ways of determining and estimating the corrosivity category of a given location according to this International Standard and the relationships among them are presented in (Figure 77). It is necessary to distinguish between corrosivity determination and corrosivity estimation. It is also necessary to distinguish between corrosivity estimation based on application of a dose-response function and that based on comparison with the description of typical atmospheric environments. (BSI, 2012)

These International Standard (9223, 922 and 9226) are useful to understand the general process beyond the corrosion process, and its categorization, but they do not consider the design and mode of operation of the product, steps in the choice of optimized corrosion protection measures in atmospheric environments are defined in ISO 11303.

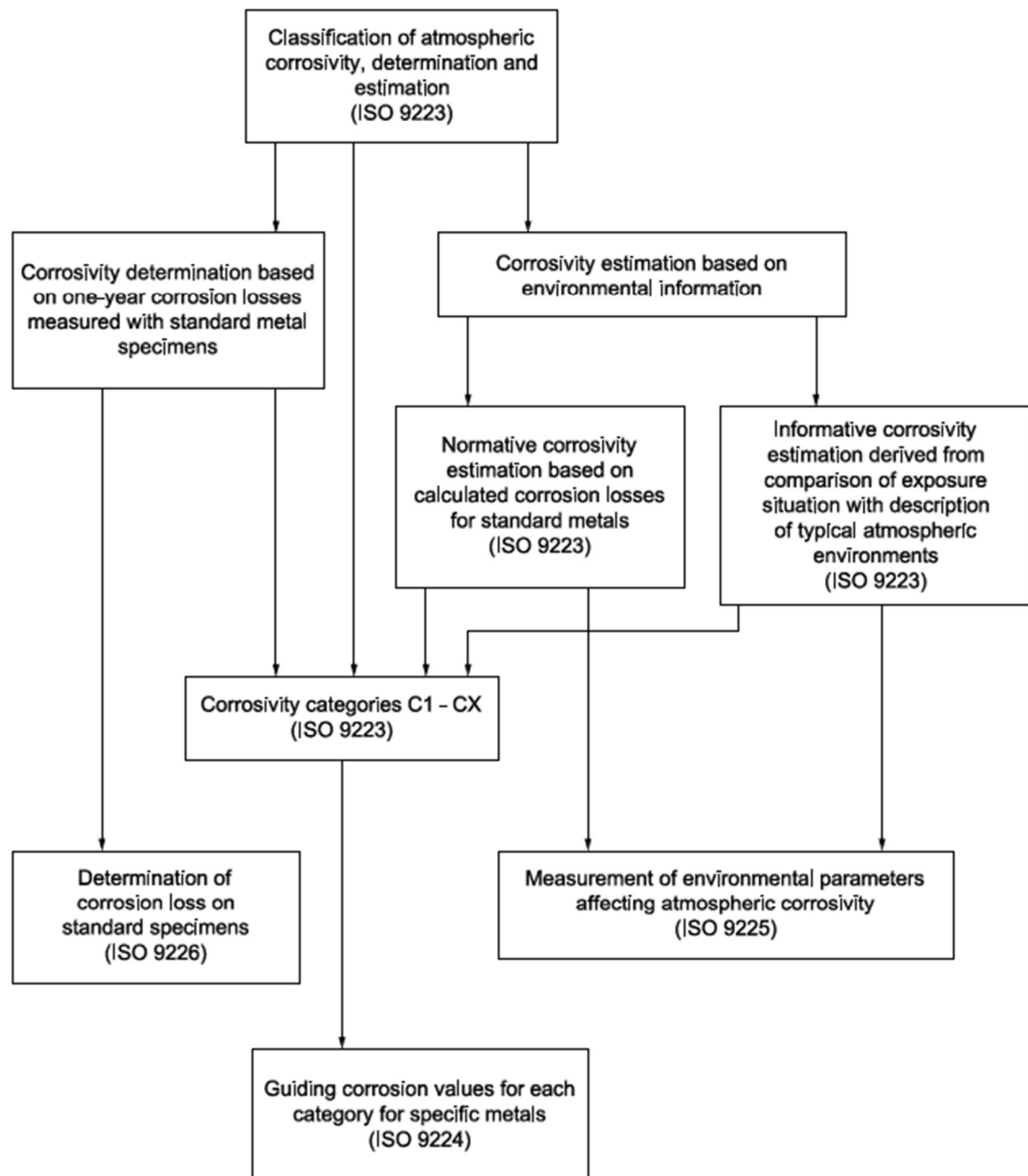


Figure 77: Classification of atmospheric corrosivity. (BSI, 2012)

In (Table 20) a definition of the principal terms is led.

Term	Definition
Corrosivity of atmosphere	Ability of the atmosphere to cause corrosion in a given corrosion system
Category of corrosivity of atmosphere	Standardized rating of corrosivity of atmosphere in relation to the one-year corrosion effect
Type of atmosphere	Characterization of the atmosphere based on appropriate classification criteria other than corrosivity or of complementary operation factors (i.e. rural, urban)
Temperature-humidity complex	Combined effect of temperature and relative humidity on the corrosivity of the atmosphere
Time of wetness	Period when a metallic surface is covered by adsorptive and/or liquid films of electrolyte to be capable of causing atmospheric corrosion
Pollution level	Numbered rank based on quantitative measurements of specific chemically active substances, corrosive gases or suspended particles in the air (both natural and the results of human activity) that are different from the normal components of the air
Category of location	Conventionally defined typical exposure conditions of a component or structure (i.e. Exposure in the open air, under shelter)
Dose-response function	Relationship derived from results of field tests for calculation of corrosion loss from average values of environmental parameters

*Table 20: Terms and definitions related to corrosivity (BSI, 2012)*

## 5.1 CORROSIVITY OF ATMOSPHERE

EN ISO 9223 establishes a comprehensive classification system for the corrosivity of atmospheric environments and provides the methodological framework used in this chapter. Specifically, the standard defines corrosivity categories based on the first-year corrosion rate of standard metallic specimens, offering a direct and measurable approach to evaluating the aggressiveness of the atmosphere. In addition, it introduces dose-response functions that allow a normative estimation of the corrosivity category through the calculation of first-year corrosion losses for different metals, thereby linking environmental parameters to material degradation. Finally, the standard enables an informative assessment of atmospheric corrosivity using qualitative or quantitative knowledge of local environmental conditions, making it applicable even where on-site corrosion measurements are not available.

In the following sections, these three complementary approaches are examined in detail. Section 5.1.1 discusses the evaluation of corrosivity through the measured corrosion rate of standard specimens. Section 5.1.2 presents the dose-response functions prescribed by the standard for estimating corrosion losses from environmental data. Section 5.1.3 addresses the estimation of corrosivity based on general knowledge of local

environmental characteristics, while Section 5.1.4 summarizes the corrosivity categories defined by EN ISO 9223 that are six and goes from C1 which means very low, to C5 which means very high and an additive class called CX which means extreme.

### 5.1.1 Evaluation of corrosivity through corrosion rate of standard specimens

Numerical values of the first-year corrosion rates for standard metals (carbon steel, zinc, copper, aluminum) are given in (Table 21) for each corrosivity category. One-year exposure tests should start in the spring or autumn. In climates with marked seasonal differences, a starting time in the most aggressive period is recommended. (BSI, 2012)

Corrosivity Category	Corrosion rates of metals ( $r_{\text{corr}}$ )				
	Unit	Carbon steel	Zinc	Copper	Aluminum
C1	g/(m <sup>2</sup> a)	$r_{\text{corr}} \leq 10$	$r_{\text{corr}} \leq 0,7$	$r_{\text{corr}} \leq 0,9$	negligible
	µm/a	$r_{\text{corr}} \leq 1,3$	$r_{\text{corr}} \leq 0,1$	$r_{\text{corr}} \leq 0,1$	-
C2	g/(m <sup>2</sup> a)	$10 \leq r_{\text{corr}} \leq 200$	$0,7 \leq r_{\text{corr}} \leq 5$	$0,9 \leq r_{\text{corr}} \leq 5$	$r_{\text{corr}} \leq 0,6$
	µm/a	$1,3 \leq r_{\text{corr}} \leq 25$	$0,1 \leq r_{\text{corr}} \leq 0,7$	$1,3 \leq r_{\text{corr}} \leq 0,6$	-
C3	g/(m <sup>2</sup> a)	$200 \leq r_{\text{corr}} \leq 400$	$5 \leq r_{\text{corr}} \leq 15$	$5 \leq r_{\text{corr}} \leq 12$	$0,6 \leq r_{\text{corr}} \leq 2$
	µm/a	$25 \leq r_{\text{corr}} \leq 50$	$0,7 \leq r_{\text{corr}} \leq 2,1$	$0,6 \leq r_{\text{corr}} \leq 1,3$	-
C4	g/(m <sup>2</sup> a)	$400 \leq r_{\text{corr}} \leq 650$	$15 \leq r_{\text{corr}} \leq 30$	$12 \leq r_{\text{corr}} \leq 25$	$2 \leq r_{\text{corr}} \leq 5$
	µm/a	$50 \leq r_{\text{corr}} \leq 80$	$2,1 \leq r_{\text{corr}} \leq 4,2$	$1,3 \leq r_{\text{corr}} \leq 2,8$	-
C5	g/(m <sup>2</sup> a)	$650 \leq r_{\text{corr}} \leq 1500$	$30 \leq r_{\text{corr}} \leq 60$	$25 \leq r_{\text{corr}} \leq 50$	$5 \leq r_{\text{corr}} \leq 10$
	µm/a	$80 \leq r_{\text{corr}} \leq 200$	$4,2 \leq r_{\text{corr}} \leq 8,4$	$2,8 \leq r_{\text{corr}} \leq 5,6$	-
CX	g/(m <sup>2</sup> a)	$1500 \leq r_{\text{corr}} \leq 5500$	$60 \leq r_{\text{corr}} \leq 180$	$50 \leq r_{\text{corr}} \leq 90$	$r_{\text{corr}} \geq 10$
	µm/a	$200 \leq r_{\text{corr}} \leq 700$	$8,4 \leq r_{\text{corr}} \leq 25$	$5,6 \leq r_{\text{corr}} \leq 10$	-

Table 21: Corrosion rates,  $r_{\text{corr}}$ , for the first year of exposure for the different corrosivity categories (BSI, 2012)

The corrosion rates exceeding the upper limits in category C5 are considered extreme. Corrosivity category refers to specific marine and marine/industrial environments.

### 5.1.2 Corrosivity estimation based on environmental information: dose-response function

If it is not possible to determine the corrosivity categories by the exposure of standard specimens, an estimation of corrosivity may be based on corrosion loss calculated from environmental data or on information in environmental conditions and exposure situations (BSI, 2012).

Dose-response functions can be used to describe the corrosion attack after the first year of exposure in open air as a function of SO<sub>2</sub> dry deposition, chloride dry deposition, temperature and relative humidity. Functions are based on results of worldwide corrosion field exposures and cover climatic earth conditions and pollution within the scope of this International Standard. (BSI, 2012). The equations to use change with the material analyzed are from Eq (24) to Eq (32).



For steel:

$$r_{corr} = 1,77 \cdot P_d^{0,52} \cdot \exp(0,020 \cdot RH + f_{st}) + 0,102 \cdot S_d^{0,62} \cdot \exp(0,033 \cdot RH + 0,040 \cdot T) \quad (24)$$

$$\begin{aligned} f_{st} &= 0,150 \cdot (T - 10) \text{ for } T \leq 10^\circ C \\ f_{st} &= -0,054 \cdot (T - 10) \text{ for } T \geq 10^\circ C \end{aligned} \quad (25)$$

$$N = 128, R^2 = 0,85 \quad (26)$$

For zinc:

$$r_{corr} = 0,0129 \cdot P_d^{0,44} \cdot \exp(0,046 \cdot RH + f_{zn}) + 0,0175 \cdot S_d^{0,57} \cdot \exp(0,008 \cdot RH + 0,085 \cdot T) \quad (27)$$

$$\begin{aligned} f_{zn} &= 0,038 \cdot (T - 10) \text{ for } T \leq 10^\circ C \\ f_{zn} &= -0,071 \cdot (T - 10) \text{ for } T \geq 10^\circ C \end{aligned} \quad (28)$$

$$N = 114, R^2 = 0,78 \quad (29)$$

For copper:

$$r_{corr} = 0,0053 \cdot P_d^{0,26} \cdot \exp(0,059 \cdot RH + f_{cu}) + 0,01025 \cdot S_d^{0,27} \cdot \exp(0,036 \cdot RH + 0,049 \cdot T) \quad (30)$$

$$\begin{aligned} f_{cu} &= 0,126 \cdot (T - 10) \text{ for } T \leq 10^\circ C \\ f_{cu} &= -0,080 \cdot (T - 10) \text{ for } T \geq 10^\circ C \end{aligned} \quad (31)$$

$$N = 121, R^2 = 0,88 \quad (32)$$

Where:

- $r_{corr}$  is first year corrosion rate of metal, expressed in micrometers per year ( $\mu\text{m/a}$ )
- $T$  is the annual average temperature, expressed in degrees Celsius ( $^\circ\text{C}$ );
- $RH$  is the annual average relative humidity, expressed as a percentage (%);
- $P_d$  is the annual average  $\text{SO}_2$  deposition, expressed in milligrams per square meter per day [ $\text{mg}/(\text{m}^2\text{d})$ ];
- $S_d$  is the annual average  $\text{Cl}^-$  deposition, expressed in milligrams per square meter per day [ $\text{mg}/(\text{m}^2\text{d})$ ].

The dose-response functions can be used when the parameters defining it respect a given range, as reported in (Table 22).

Symbol	Description	Interval	Unit
T	Temperature	-17,1 to 28,7	$^\circ\text{C}$
RH	Relative humidity	34 to 93	%
$P_d$	$\text{SO}_2$ deposition	0,7 to 150,4	$\text{mg}/\text{m}^2\text{d}$
$S_d$	$\text{Cl}^-$ deposition	0,4 to 760,5	$\text{mg}/\text{m}^2\text{d}$

Table 22: Parameters interval used in the derivation of dose-response functions.

### 5.1.3 Estimation of the corrosivity category based on knowledge of the local environment situation

The classification approach for informative corrosivity estimation must be simple, as far as the parameters to be considered for this scope. The principal's atmosphere factors for corrosion of metals and alloys are the temperature-humidity complex, and sulfur dioxide and chloride pollution levels (BSI, 2012).

The relative humidity is caused by the wetting of surfaces, the length of time during which relative humidity is greater than 80 % at a temperature greater than 0 °C (measured in hour per year) is used to estimate the calculated time of wetness,  $\tau$  (see Table 23), of corroding surfaces.

Time of wetness [h/a]	Level	Example of occurrence
$\tau \leq 10$	$\tau_1$	Internal microclimates with climatic control
$10 \leq \tau \leq 250$	$\tau_2$	Internal microclimates without climatic control except for internal non-air-conditioned spaces in damp climates
$250 \leq \tau \leq 2500$	$\tau_3$	Outdoor atmospheres in dry, cold climates and some zones of temperate climates; properly ventilated sheds in temperate climates
$2500 \leq \tau \leq 5500$	$\tau_4$	Outdoor atmospheres in all climates (except for dry and cold climates); ventilated. sheds in humid conditions; unventilated sheds in temperate climates
$5500 \leq \tau$	$\tau_5$	Some zones of damp climates; unventilated sheds in humid conditions

Table 23: Time of wetness in different exposure conditions (BSI, 2012)

The other factor is the pollution level caused by sulfur dioxide (Table 24) and/or airborne salinity (Table 25):

Deposition rate of SO <sub>2</sub> [mg/m <sup>2</sup> d]	Concentration rate of SO <sub>2</sub> [μg/m <sup>3</sup> ]	Level
$P_d \leq 4$	$\leq P_c \leq 5$	P <sub>0</sub> Rural atmosphere
$4 \leq P_d \leq 24$	$5 \leq P_c \leq 30$	P <sub>1</sub> Urban atmosphere
$24 \leq P_d \leq 80$	$30 \leq P_c \leq 90$	P <sub>2</sub> Industrial atmosphere
$80 \leq P_d \leq 200$	$90 \leq P_c \leq 250$	P <sub>3</sub> Highly polluted industrial atmosphere

Table 24: Grouping of pollution by sulfur-containing substances represented by SO<sub>2</sub> (BSI, 2012)

Deposition rate of chloride [mg/(m <sup>2</sup> d)]	Level
$S_d \leq 3$	S <sub>0</sub>
$3 \leq S_d \leq 60$	S <sub>1</sub>
$60 \leq S_d \leq 300$	S <sub>2</sub>
$300 \leq S_d \leq 1500$	S <sub>3</sub>

Table 25: Grouping of pollution by airborne salinity represented by chloride based on wet candle method (BSI, 2012)

### 5.1.4 Corrosivity categories

The category of corrosivity of atmosphere is a standardized rating of corrosivity of atmosphere, mostly, in relation to the one-year corrosion effect, were not possible, it is related to estimation based on environmental parameters or information. It is divided into six categories, see (Table 26)

Cat.	Corrosivity	Typical environments - Examples	
		Indoor	Outdoor
C1	Very low	Heated spaces with low relative humidity and insignificant pollution, e.g. offices, schools, museums	Dry or cold zone, atmospheric environment with very low pollution and time of wetness, e.g. certain deserts, Central Arctic/Antarctica
C2	Low	Unheated spaces with varying temperature and relative humidity. Low frequency of condensation and low pollution, e.g. storage, sport halls	Temperate zone, atmospheric environment with low pollution ( $\text{SO}_2 < 5 \mu\text{g}/\text{m}^3$ ), e.g. rural areas, small towns Dry or cold zone, atmospheric environment with short time of wetness, e.g. deserts, subarctic areas
C3	Medium	Spaces with moderate frequency of condensation and moderate pollution from production processes, e.g. food-processing plants, laundries, breweries, dairies	Temperate zone, atmospheric environment with medium pollution ( $\text{SO}_2$ : $5 \mu\text{g}/\text{m}^3$ to $30 \mu\text{g}/\text{m}^3$ ) or some effect of chlorides, e.g. urban areas, coastal areas with low deposition of chlorides Subtropical and tropical zone, atmosphere with low pollution
C4	High	Spaces with high frequency of condensation and high pollution from production processes, e.g. industrial processing plants, swimming pools	Temperate zone, atmospheric environment with high pollution ( $\text{SO}_2$ : $30 \mu\text{g}/\text{m}^3$ to $90 \mu\text{g}/\text{m}^3$ ) or substantial effect of chlorides, e.g. polluted urban areas, industrial areas, coastal areas without spray of salt water or, exposure to strong effect of de-icing salts Subtropical and tropical zone, atmosphere with medium pollution
C5	Very high	Spaces with very high frequency of condensation and/or with high pollution from production process, e.g. mines, caverns for industrial purposes, unventilated sheds in subtropical and tropical zones	Temperate and subtropical zone, atmospheric environment with very high pollution ( $\text{SO}_2$ : $90 \mu\text{g}/\text{m}^3$ to $250 \mu\text{g}/\text{m}^3$ ) and/or significant effect of chlorides, e.g. industrial areas, coastal areas, sheltered positions on coastline
CX	Extreme	Spaces with almost permanent condensation or extensive periods of exposure to extreme humidity effects and/or with high pollution from production process, e.g. unventilated sheds in humid tropical zones with penetration of outdoor pollution including airborne chlorides and corrosion-stimulating particulate matter	Subtropical and tropical zone (very high time of wetness), atmospheric environment with very high $\text{SO}_2$ pollution (higher than $250 \mu\text{g}/\text{m}^3$ ) including accompanying and production factors and/or strong effect of chlorides, e.g. extreme industrial areas, coastal and offshore areas, occasional contact with salt spray

Table 26: Corrosivity categories (BSI, 2012)

## 5.2 CORROSION OF METAL AND ALLOYS

The corrosion of metallic materials includes all the interactions between the environment and the metallic surface. As exposed in the previous chapter 5.1, the major factor that influences the corrosion process is the micro-environment (composition, temperature, pH, oxygen dissolved and similar aspects). The driving force for metallic corrosion is that the oxidized form of metallic atoms is the most thermodynamically stable, since the metallic state is temporary, corrosion is a natural and spontaneous evolution of the surface of metal that turns into its stable form, the oxide one.

Generic corrosion processes can be described as an electrochemical process generated by the oxidation of metallic materials, where anodic reaction takes place and metal is consumed, and by reduction of non-metallic species, where cathodic reaction takes place.

According to this description corrosion is due to the formation of an electrochemical cell with the presence of an anode and of a cathode and of an electrolyte that enters in contact both with the anode and the cathode. So, it can be said that higher is the negative potential of metal, more is subjected to corrosion.

To complete the electrochemical cell a potential difference should be present between the cathode and the anode. It means that each electrode has to be characterized by a certain potential (electrochemical potential). In particular the anodic zone has to be characterized by a negative electrochemical potential whereas the cathode has to be characterized by a positive or by a less negative potential. The two electrodes in the corrosion cell can be constituted by either different materials or by the same material that locally has a different electrochemical potential.

As said in Di Sarno, Majidian, & Karagiannakis, (2021) corrosion can be classified using different approaches. The most conventional classification divides the corrosion types according to their appearance which some of them can be identified visually and others are not visible, most common are reported in (Table 27) a representation is given in (Figure 78)

Type of corrosion	Description
Uniform corrosion (a)	Corrosion attack proceeds uniformly on all the surface exposed to aggressive environment. The uniform corrosion can reduce the rate of corrosion by limiting the contact surface between metal and the atmosphere. Based on this a way to control this type of corrosion is to use cathodic protection, for example zinc plating (see Figure 78)
Galvanic corrosion (b)	When two different metals are put in contact and they are embedded into an electrolyte. Due to the difference in corrosion potential of the two materials a galvanic cell takes place
Pitting corrosion (c)	One of the most common, characterized by a small anodic reaction, as consequence even the cathodic region became clearly visible. Local attack can be highlighted, with a sort of excavated holes (pits) into the surface.
Crevice corrosion (d)	It happens any time we have a portion of the metal hidden and difficult to be "washed" (i.e. hidden bolt or junctions). This scenario brings to different % of $\approx 2$ or to presence of stagnant water.
Erosion corrosion (e)	When fluid flowing with the relatively high velocity attacks over the surface of the metal, it can remove the coating film and accelerate the corrosion process. (Di Sarno, Majidian, & Karagiannakis, 2021)

Stress corrosion (f)	It extremely depends on the material. It starts due to the presence of a corrosive environment and within a residual stress (usually tensile)
Fatigue corrosion (g)	It occurs when repeated applied loads applied into a corrosive environment causes stress concentration which leads to cracks into the metal.
Fitting corrosion (h)	When two surfaces are in close contact in the presence of load provoke the abrasion of the surfaces by oxide (Di Sarno, Majidian, & Karagiannakis, 2021)
Intergranular corrosion (i)	The co corrosion attack between steel grain boundaries which affect the mechanical properties of the material. (Di Sarno, Majidian, & Karagiannakis, 2021)

Table 27: Corrosion classification in function of their appearance

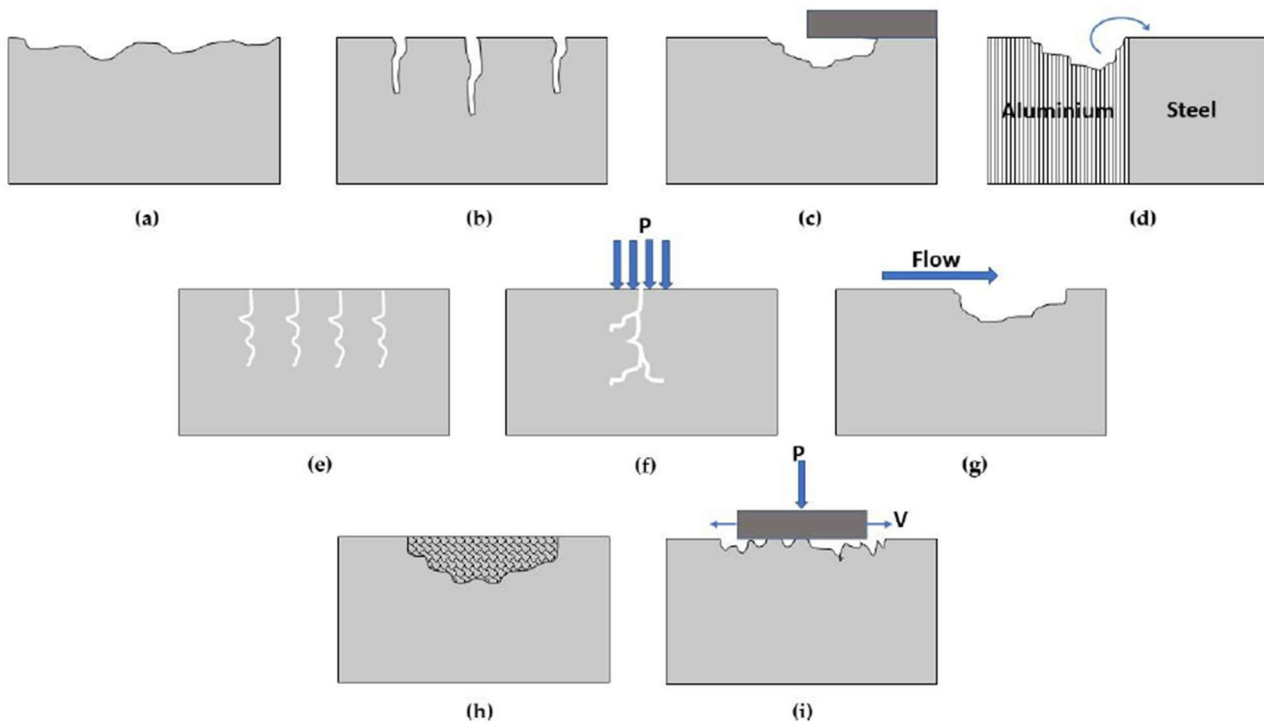


Figure 78: Prevalent forms of corrosion in steel structures: (a) uniform; (b) pitting; (c) crevice; (d) galvanic; (e) fatigue; (f) stress; (g) erosion; (h) intergranular; and (i) fitting corrosion (Di Sarno, Majidian, & Karagiannakis, 2021)

### 5.2.1 Environments effect

Environment is a determinant factor for the corrosion of mild steel, depending on its composition the process can be more or less detrimental. To evidence the different effects, (Chuka, Odio, Chukwuneke, & Sinebe, 2014) perform an investigation on five different scenarios: presence of 0,1mol of Hydrochloric acid, underground (soil), atmosphere, salt water and fresh water. The parameter measured in the test is the weight loss in 5 weeks, plotting results each week passed, from this parameter the corrosion rate is computed using Eq. 33

$$r_{corr} = \frac{k \times \Delta w}{A \times T \times \rho} \quad (33)$$

Where  $r_{corr}$  is the corrosion rate in mm/year,  $\Delta w$  is the weight loss in gram,  $A$  is the exposed surface area of the sample,  $\rho$  is the density of sample in g/cm<sup>3</sup> and  $k$  is a constant for the unit conversion = 8,76E104

The results of Chuka, Odio, Chukwuneke, & Sinebe, (2014) are reported below:

	1 <sup>st</sup> Week	2 <sup>nd</sup> Week	3 <sup>rd</sup> Week	4 <sup>th</sup> Week	5 <sup>th</sup> Week
C <sub>R</sub> of HCl	2,5563	1,4997	2,1850	2,551	2,9977
C <sub>R</sub> of Soil	0,0170	0,0341	0,7345	1,5473	1,5880
C <sub>R</sub> of Atmosphere	0,0085	0,0197	0,0302	0,2275	0,1977
C <sub>R</sub> of Salt water	0,0597	0,9464	1,1242	1,3201	1,0622
C <sub>R</sub> of Fresh water	0,0139	0,0689	0,4686	0,8267	1,0010

*Figure 79: Corrosion rate plot for different environmental scenarios. (Chuka, Odio, Chukwuneke, & Sinebe, 2014)*

The results are in line with the (BSI, 2012) which says that the corrosion rate is not constant in time, it is greater at the beginning; as matter of fact the study demonstrates tant once the corrosion process start the initial weeks present a derivative of the corrosion rate in time, grater with respect to the ones in late weeks.

In addition it can be highlighted, as said in chapter 5.1.1, that the acid environment is the worst for the corrosion, followed by the salt water environment.

## 5.2.2 Corrosion test in artificial atmosphere

The long-term performance of rockfall barriers is strongly influenced by degradation caused by corrosion. Since these protection devices are always exposed to extreme conditions, the understanding of their corrosion is essential to evaluate their durability and maintenance program. To simulate in short-term the natural corrosion mechanisms that take place, laboratory tests are widely used. These tests simulate the environmental conditions in all their possible scenarios, that brins to understanding the corrosion process and its evolution in time. This sub-chapter contains two guided normative tests that can be performed to obtain the researched information.

### 5.2.1.1 Salt spray test

It must be said that this test is described into (BSI, 2017), that well specify that this procedure should not be taken as a reference for the corrosion all the metallic materials in all environments, it is a guide. Nevertheless, the method described gives a means of checking that the comparative quality of a metallic material, with or without corrosion protection. In addition, this test cannot be applicable to metals with different materials substructures.

In the neutral salt spray (NNS) test a neutral 5% sodium chloride solution is atomized under a controlled environment of the spray cabinet, which is the room where the test is conducted (Figure 80 and Figure 81)

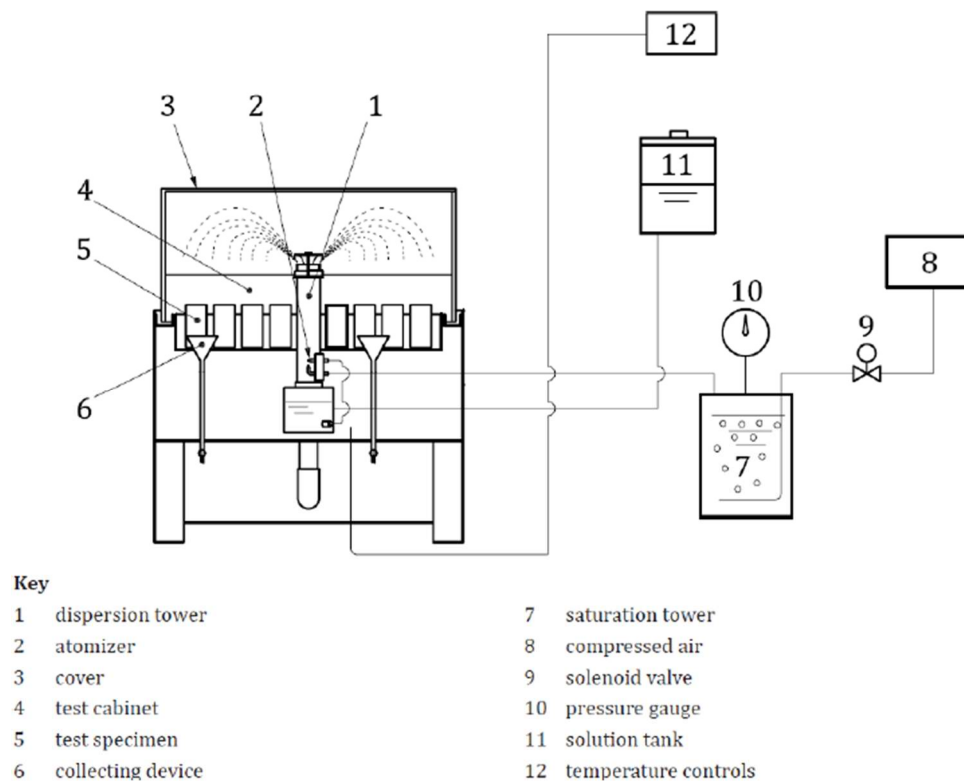


Figure 80: Schematic diagram of one possible design of spray cabinet (front view) (BSI, 2017)

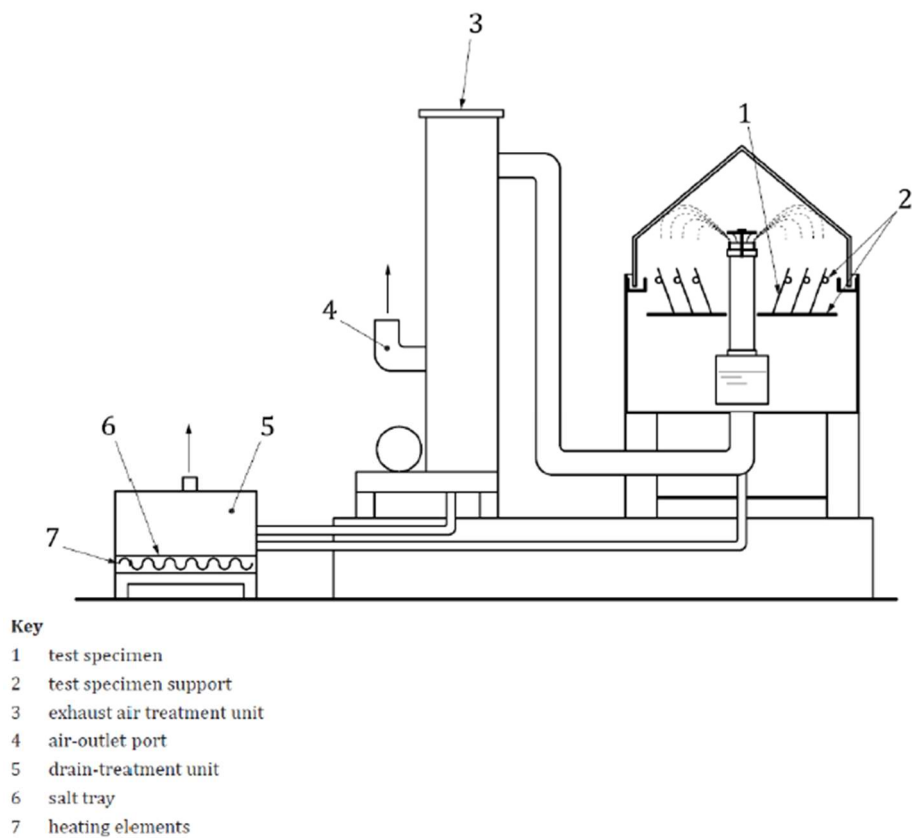


Figure 81: Schematic diagram of one possible design of spray cabinet (side view) (BSI, 2017)



BSI, (2017) explains the process for the NSS test: once the solution is ready, it must be adjusted in such a way that the pH is between 6,5 and 7,2, temperature at 25°C with a deviation of maximum 2 °C. All components in contact with the spray or the test solution shall be made of, or lined with, materials resistant to corrosion by the sprayed solution and which do not influence the corrosivity of the sprayed test solutions. Air in the cabin must be properly humidified, in order to not have evaporation of the solution, and at a specific temperature, in order to not have change in the one of the solutions. These are some of the directives reported in the normative.

To determine the corrosivity of the tests, specimens made of steel shall be used. As a complement to the reference specimens made of steel, high-purity zinc specimens may also be exposed in the test in order to determine the corrosivity against this metal.

At the end of the test, the specimens must be immediately removed from the test cabinet and the protective coating, and the corrosion products must be taken off, in order to evaluate the mass loss.

The period of the test depends on the material, anyway (BSI, 2017) gives recommended periods of exposure: that are 2, 6, 24, 48, 86, 168, 240, 480, 720 and 1008 hours.

The results can be evaluated in different criteria, depending on the requirements. (BSI, 2017) report some:

- appearance of the test;
- appearance after removing superficial corrosion product;
- number and distribution or corrosion defects;
- time elapsed before the appearance of the first signs of corrosion;
- change in masse;
- alteration reveled by micrographic examination;
- change in mechanical properties.

If the test is performed even on a zinc specimen (suggested), BSI, (2017) exhibit a complementary method for evaluating corrosivity.

#### **5.2.1.2 Accelerated corrosion test**

BSI, (2015) specifies the test methos, the reagents, and the procedure to be used in an accelerated atmospheric corrosion test constituting a 6 h exposure to a slightly acidified solution of 1 % NaCl twice weekly, followed by a condition of controlled humidity cycling between 95 % RH and 50 % RH at a constant temperature of 35 °C. These are some of the properties, Normative gives them all.

BSI, (2015) specifies that specimens are subjected to a 12-hour cycle. Every seven cycle a cycle with salt spraying must be performed. At the end of the test period, remove the test objects from the chamber and allow them to dry for 0,5 h to 1 h before rinsing, in order to reduce the risk of removing corrosion products. Before they are examined, carefully remove the residues of spray solution from their surfaces.

Many different criteria for the evaluation of the test results can be applied to meet requirements, BSI, (2015) propose the same of the salt spray test: previous chapter (5.2.2.1).

BSI, (2015) exhibits the way to determine the mass loss: immediately after the end of the test, remove the protective coating, then remove the corrosion products by repetitive cleaning. From the plot of mass versus number of cleaning cycles, determine the true mass of the specimen after removal of the corrosion products as described in ISO 8407. Subtract this number from the initial mass of the reference specimen prior to testing and divide the resulting number by the area of the exposed surface area of the reference specimen to assess the metal mass loss per square meter of the reference.

### 5.3 CORROSION OF ROCKFALL BARRIER COMPONENTS

The barriers are made from carbon steel and are exposed to natural environments, which in some cases, such as barriers close to the sea, can be very aggressive. Therefore, the durability and susceptibility to atmospheric corrosion of the structures must be considered very carefully. The location of the barriers is in many cases difficult to reach and therefore an inspection or maintenance program is often impossible. This is the reason why it is necessary to consider carefully, at the design stage, any aspects which may help to increase and guarantee the durability of the barriers, because degradation due to corrosion can makes the barriers useless and pose an unacceptable risk related to the fall of stones or avalanches.

#### 5.3.1 Net corrosion and effects

As said in chapter 3.1.1 net fence is one of the most important elements for consuming the impact energy. These nets are prone to corrosion due to continuous exposure to natural environments. This susceptibility diminishes their mechanical performance and service life (Xu, Cheng, Zhao, Liu, & Yu, 2024).

Considering the high quantity of studies that do not take into account the mechanical properties variation of this element, due to the corrosion, Xu, Cheng, Zhao, Liu, & Yu, (2024) realized an experimental study on this aspect. Test was performed on uncoated, zinc coated and Galban coated (evolution of zinc-aluminum coated). For each of these types, 7 samples were analyzed with 7 different exposure times (0,2,4,6,8,10 and 12 weeks), for a total of 21 samples. The adopted test is the neutral salt spray (chapter 5.2.2). Aspect of the specimens after the test are reported in (Figure 82)






















Coating materials Corrosion duration(week)	Uncoated	Zinc-coated	Galfan-coated
0			
2			
4			
6			
8			
10			
12			

Figure 82: Specimens' aspect at different corrosion duration (Xu, Cheng, Zhao, Liu, & Yu, 2024)

After the corrosion test, Xu, Cheng, Zhao, Liu, & Yu, (2024) evaluated the mechanical properties with the quasi-static tensile tests were conducted on both steel-wire specimens and wire-ring specimens. The results of their test are reported in (Figure 83).

Specimens	Uncoated wires				Zinc-coated wires				Galfan-coated wires			
Corrosion duration (week)	0	4	8	12	0	4	8	12	0	4	8	12
Average breaking force (kN)	13.72	11.09	9.83	7.79	13.52	12.80	12.58	12.54	12.60	12.28	12.2	12.09
Reduced breaking force (kN)	/	2.63	3.39	5.93	/	0.72	0.94	0.98	/	0.32	0.40	0.51
Reduction rate (%)	/	19.17	28.35	43.22	/	5.33	6.95	7.25	/	2.54	3.17	4.05

Figure 83: Breaking force reduction due to corrosion for the three different types of specimens (Xu, Cheng, Zhao, Liu, & Yu, 2024)

### 5.3.2 Rope and rope anchor corrosion

Such as net, even rope and rope anchors are structural elements that are subjected to corrosion, leading to a reduction of their properties and so of the total system of the barrier. (Deflorian, Rossi, Tancon, & Bonora, 2004) propose a study on two different kinds of wire: zinc coated and zinc-aluminum coated both applied with hot dip, and analyzed with two different geometry (Figure 84), on which electrochemical approach was applied as an alternative to simple exposure testing for evaluation of the durability of structural ropes. Ropes were subjected to a salt spray chamber in order to provide a first overview of the corrosion properties, after that electrochemical impedance measurements were carried out in 0,35% NaCl with a three-electrode cell. The signal amplitude was 10 mV (RMS), and the frequency range was 105–0,01 Hz.

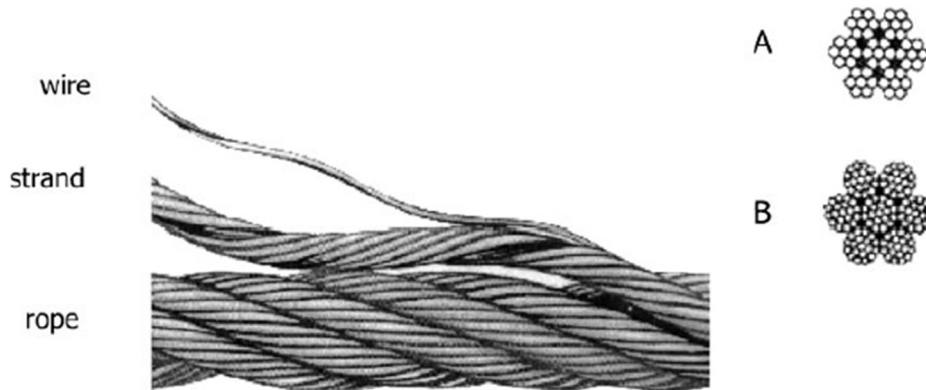


Figure 84: Two geometries of the (Deflorian, Rossi, Tancon, & Bonora, 2004) test: A) Seven wires in each strand and seven strands in the rope, B) 19 wires in every strand and seven strands in the rope.

Deflorian, Rossi, Tancon, & Bonora, (2004) highlights that corrosion phenomena are worst in pure zinc coating, respect to the zinc-aluminum. Summed results of the corrosion taken place are shown in (Figure 85)

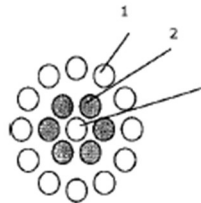
	Zn (B)	zone 1: steel corrosion (red rust) zone 2: zinc corrosion (white zinc hydroxides) zone 3: zinc corrosion (white zinc hydroxides)
	Zn/Al (B)	zone 1: zinc corrosion (white zinc hydroxides) zone 2: few zinc corrosion products (white zinc hydroxides) zone 3: no corrosion detected
	Zn (A)	zone 2: steel corrosion (red rust) zone 3: zinc corrosion (white zinc hydroxides)
	Zn/Al (A)	zone 2: zinc corrosion (white zinc hydroxides) zone 3: no corrosion detected

Figure 85: Corrosion behavior of ropes exposed for 500h in salt spray chamber. (Deflorian, Rossi, Tancon, & Bonora, 2004)

### 5.3.3 Strength reduction due to corrosion

In this paragraph, statistical analysis is used to evaluate the maximum diameter reduction of steel wire to determine its strength reduction and the critical reduction value that involves the failure of the element. To this, an introduction to the statistical elements is present and a material theory that fits perfectly with the scope of this analysis: the Weibull theory.

#### 5.3.3.1 Statistical elements and Weibull theory

Let  $X$  be a continuous random variable over the interval  $[x_1, x_2]$ . The cumulative probability density function (Figure 86),  $P(x)$  is defined in Eq (34)

$$P(X) = \text{probability} (X < x) \quad (34)$$

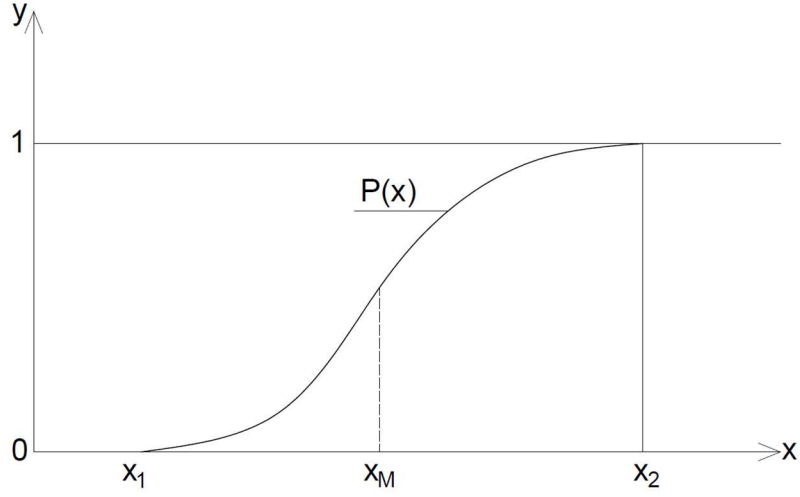


Figure 86: Cumulative probability density function.

The probability density function  $p(x)$  is defined as the probability that the random variable  $X$  takes a value included between  $x$  and  $x + dx$ . It is defined as the area below the curve of the probability density distribution (Figure 87).

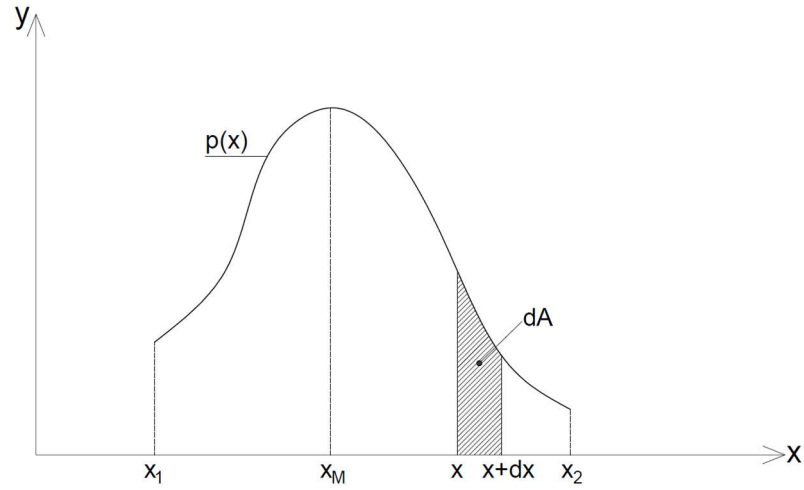


Figure 87: Probability density function.

These two functions are related, their relation is reported in Eq (34) and Eq (35)

$$p(x) = \frac{dP}{dx} \quad (34)$$

$$P(x) = \int_{x_1}^x p(x) dx \quad (35)$$

### 5.3.2.2 Weibull theory

Weibull theory is applied to homogeneous and isotropic materials, in addition the hypothesis of weakest link in a chain is introduced. It says that when the failure occurs in one of the links of the chain, this generates the failure of the entire chain. This hypothesis is true in material that are not capable of load redistribution.

With this approach the element is schematized as a progression series of elements like in a chain. The cumulated probability of resistance of a single element is defined as  $P_1(\sigma)$ , probability of the resistance to be lower than  $\sigma$ , that is the stress generated from the action. To this probability Weibull assign the name of failure

probability, because it represents the probability of resistance to be lower than  $\sigma$ . The complementary to 1 of this value, can be defined as the survival probability.

Taking  $N$  elements in series, each characterized by a probability of failure  $P_1(\sigma)$ , with the hypothesis of weakest link, a chain of  $N$  elements resist only if any of them it's capable to resist the stress  $\sigma$ , thus the survival probability of the chain is defined by Eq (36), and the failure probability by Eq (37)

$$[1 - P_1(\sigma)]^N \quad (36)$$

$$P_N(\sigma) = 1 - [1 - P_1(\sigma)]^N \quad (37)$$

Using mathematical simplification the expression of failure probability  $P_N(\sigma)$  can be rewritten as in Eq (38)

$$P_N(\sigma) = 1 - \exp[-NP_1(\sigma)] \quad (38)$$

To realize strands the steel used is the galvanized or zinc coated, which have the same coating but different application process. The tensile strength is defined in Eq (39), where  $f_{p0,1k}$  is the yielding strength and  $f_{pk}$  is the ultimate strength.

$$\sigma_{p,max} = \min(0,8f_{pk} ; 0,9f_{p0,1k}) \quad (39)$$

The failure of the element is reached when the resistance  $\sigma_{p,max}$  of the material is lower than  $\sigma$ , generated from the action, and its computation is expressed in Eq (40)

$$\sigma = \frac{N}{A} \quad (40)$$

$$A = \frac{\pi D^2}{4} \quad (41)$$

$$D_{eff} = D_0 - \Delta D \quad (42)$$

$$D_c = \sqrt{\frac{4N}{\pi * \sigma_{p,max}}} \quad (43)$$

Where  $A$  is the area of the steel strands computed with simplification as reported in Eq (41). This parameter tends to reduce with time because of diameter reduction.

Diameter reduction affects the totality of the strands, but not with a homogeneous pattern, (as shown in Figure 88) thus generating points along the element where the diameter is lower, and among these a smallest one can be detected:  $D_{min}$ . Weibull theory is applied by dividing the strands into pieces that correspond to the elements of the chain. The number of pieces is defined with  $N$  as the number of links in the chain theory. Failure is reached when the effective diameter ( $D_{eff}$ ), defined as the initial diameter ( $D_0$ ) minus the corrosion thickness ( $2\Delta D$ ) Eq. (42), reaches a critical value ( $D_c$ ) such that  $\sigma$  became equal to  $\sigma_{p,max}$  Eq. (43); that is equal to say that reduction of diameter  $\Delta D$  reaches a value  $\Delta D_c$ . So, the probability of failure of a single element is defined as the probability of  $\Delta D$  to be greater than  $\Delta D_c$ , or as the probability of  $D_{eff}$  to be lower than  $D_c$  Eq. (44). Using Eq (34) from Weibull theory it is possible to define the failure probability of the chain as reported in Eq. (45)

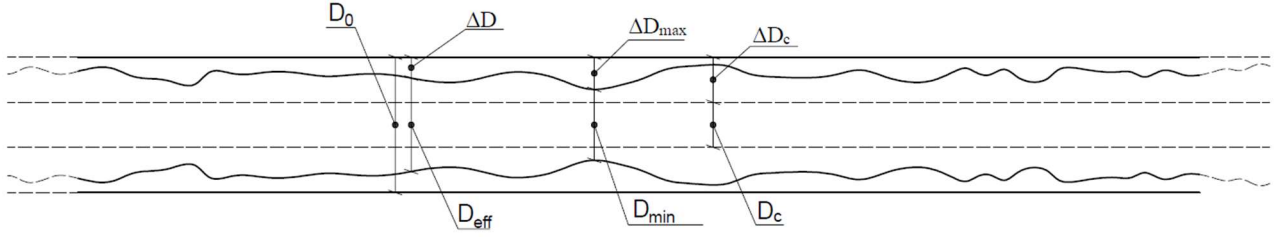


Figure 88: Elements of the strands corrosion.

$$Pf = Pi(D^*) \quad (50)$$

$$P_N(D_{min}) = 1 - \exp[-NP_i(D^*)] \quad (51)$$

The value of  $D_{min}$  must be researched along the strands, but since a continuous survey cannot be carried, a statistical analysis must be developed. To this end, analyzing  $\Delta D$  instead of  $D_{eff}$  is better, because it is distributed as a lognormal function. Achieving a minimum of thirty point ( $N = 30$ ) per each elements a probability function with a lognormal distribution can be plotted (Figure 89)

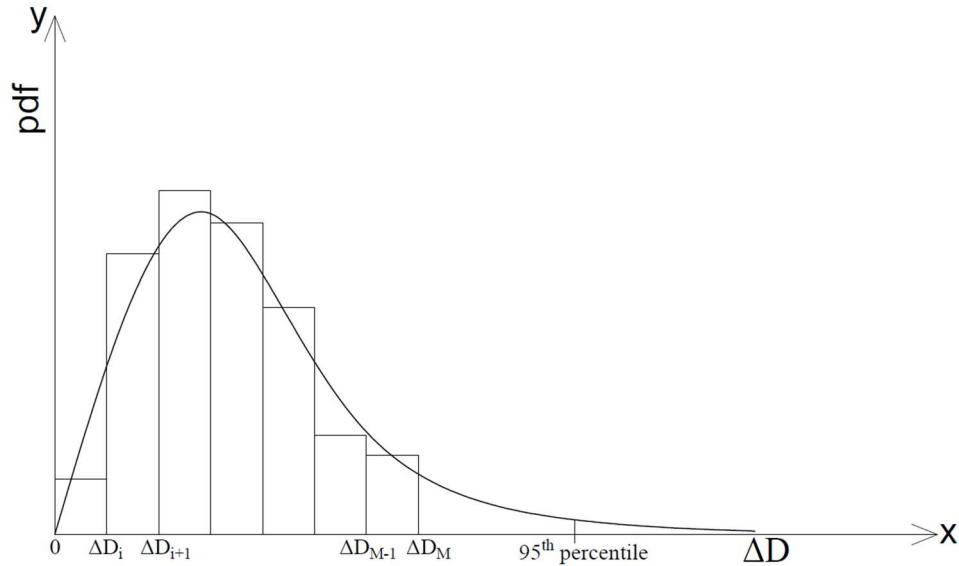


Figure 89: Lognormal distribution of  $\Delta D$  detached.

The researched value is  $D_{min}$  that is the same to research  $\Delta D_{max}$ . To this scope a semi-probabilistic approach is introduced, for which a value corresponding to the 95<sup>th</sup> percentile of  $\Delta D$  distribution (value that has the probability to be overrun equal to 5%), is taken as the maximum value. So, if this value is greater than  $\Delta D_c$  failure into the link is reached, and so failure into the total chain.

Alternative to this, an analysis without subdivision in pieces can be performed. In this case, however, the Weibull theory cannot be applied since only a single value of  $\Delta D_{max}$  will be available, on which to calculate the probability of failure, thus giving up a more detailed and accurate analysis.



## 5.4 PROTECTION PROCEDURE: ZINC COATING

Protection against corrosion can be realized by using coatings around the metal material. Since the corrosion process can be seen as an electrochemical cell with the presence on an anode and a cathode, this corrosion process can be easily translated into a galvanic series, where the electrochemical potential is called corrosion potential (see (Figure 90) for the reference value) . In this view of the phenomenon, corrosion takes place when the potential of two materials is different. In addition, the corrosion became faster for greater value of the potential difference.

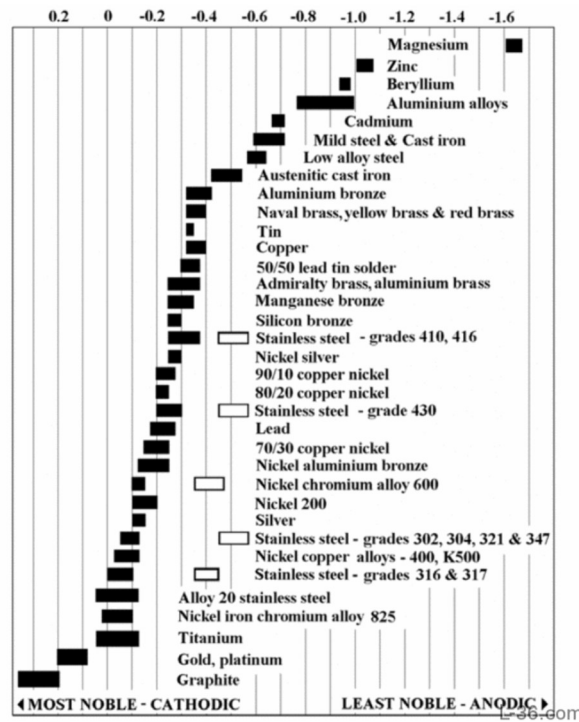


Figure 90: Corrosion potential of main structural materials.

Negative values of corrosion potential mean less noble material, so anodic reaction is consumed there, this means that the corrosion takes place. From this statement is easy to understand that zinc coating (right position, in galvanic series, with respect to the steel, and so less noble) for carbon steel generate an anodic protective layer that guarantee a priority corrosion of itself, securing the structural material, (Figure 91)

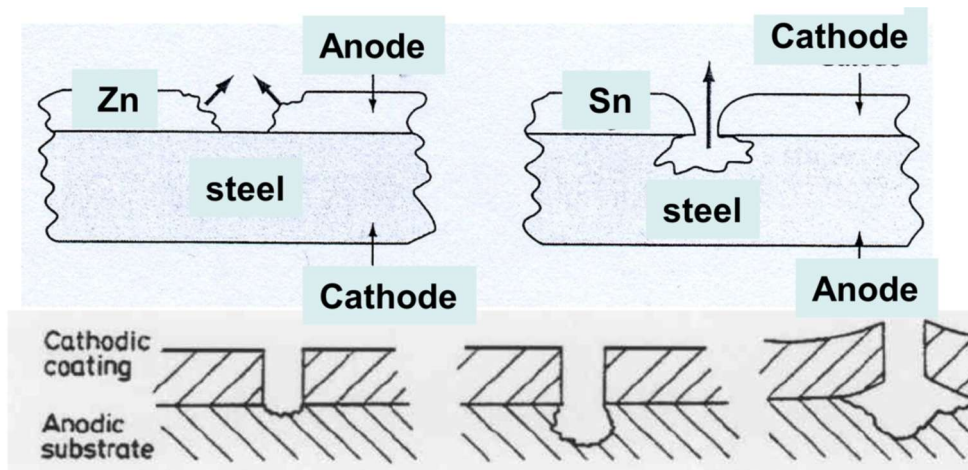


Figure 91: Anodic VS Cathodic coating for steel.

The thickness of the zinc plating is function of the corrosion rate, as reported in chapter 5.1, it depends on the environmental parameters such as, chloride presence, humidity and temperature. For the same thickness, a shorter service life is identified for severe industrial environments, while longer one for rural environment. Other environmental scenarios are exposed in the chart in (Figure 92).

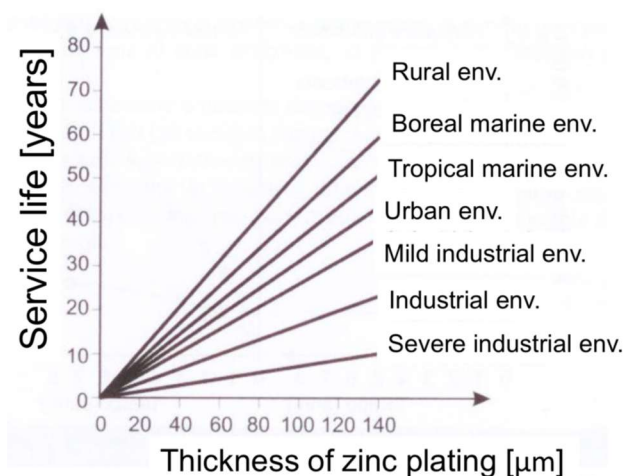


Figure 92: Service life generated from thickness of zinc coatings in function of the environmental scenarios.

Zinc coated elements must not present non coated areas, blisters, flux deposits, inclusion of dross or other perturbation types that could interfere with the use of the elements. Zinc coating must be smooth and with a uniform thickness and should adhere tenaciously to the surface of the base metal. There are different types of zinc coating, among all, general aspects of two of the main types are reported below:

The hot-dip galvanizing process consists in immersing in molten zinc, for a sufficient time to allow a metallurgical reaction between iron from the steel surface and the molten zinc, resulting in the formation of Zn/Fe alloy layers bonding the coating to the steel surface. As specified into the international normative, (AASHTO, Standard Specification for Zinc Coating (Hot-Dip) on Iron and Steel Hardware, 2016), this process is characterized by a minimum coating weight or minimum coating thickness, that must respect the values given in (Table 28).

Class of material	Minimum mass of zinc coating [g/m <sup>2</sup> ] of surface		Minimum coating thickness [microns]	
	Average of specimens tested	Any individual specimen	Average of specimens tested	Any individual specimen
Class A: castings, malleable iron, steel	610	550	86	79
Class B1: rolled, pressed, and forged articles	610	550	86	79
Class B2:	458	381	66	53
Class B3	397	336	56	48

Table 28: Thickness and weight of zinc hot-coating for various classes of material. (BSI, 2015)

Class B1, B2 and B3 differ in thickness and length dimensions. Enter in B1 class, element with thickness > 15,88mm and length > 381mm, in class B2, element with thickness < 15,88mm and length > 381mm, finally enter in class B3 element with any thickness and length < 381mm.

(AASTHO, Standard Specification for Zinc Coating (Hot-Dip) on Iron and Steel Hardware, 2016) specifies even the methods for testing, that shall be performed in order to ensure that the zinc coating is well done, in terms of its thickness and mass (Table 28), finish and appearance, embrittlement and adherence.

Mechanically zinc deposit is a cold coating process that uses kinetical energy to apply zinc coating on the metal surface. It is provided in several thicknesses. (AASTHO, Standard Specification Coatings of Zinc Mechanically Deposited on Iron and Steel, 2021) gives the classification of this coating in function of the thickness (Table 29):

Class	Minimum Thickness, [ $\mu\text{m}$ ]
110	107
80	81
70	69
65	66
55	53
40	40
25	25
12	12
8	8
5	5

Table 29: Mechanical Zinc coating classification based on thickness (AASTHO, Standard Specification Coatings of Zinc Mechanically Deposited on Iron and Steel, 2021)

#### 5.4.1 Zinc coating reduction due to environmental parameters

Existing approaches for estimating long-term corrosion loss are typically time-based, with distinct models developed for various atmospheric environments (e.g., industrial, urban, rural, and marine). However, these models generally fail to account for fluctuations in environmental conditions, despite the well-established fact that corrosion loss can vary substantially with changes in such factors. Klinesmith, McCuen, & Abrecht, (2007) formulate and validate models that show the effects of the environment on corrosion for four materials (carbon steel, zinc, copper, and aluminum). The models were formulated with a structure that yields rational effects for four environmental variables: time-of-wetness, sulfur dioxide, salinity, and temperature.

Almost all the models for the prediction of corrosion loss are based on time only, with Eq (46) formulation:

$$M = K t^n \quad (46)$$

Where: M = mass loss caused by corrosion per unit of the exposed area; t = exposure time; K = proportionality constant; and n= mass loss exponent.

Since this equation is calibrated on time only, the constant K and n contain the information regarding the environmental parameter, (i.e. K will be greater in marine environments). Eq (46) is calibrated on rural environments, so when the model is used in different environments, it yields to inaccurate predictions. During

analysis of existing models, (Klinesmith, McCuen, & Abrecht, 2007) noted that there was the need of a model capable to incorporate multiple environmental factors, has physical rational structure, allows variation of calendar time, and is sufficiently flexible that it can be transferred to other location. The proposed model is reported in Eq (47)

$$y = At^B \left( \frac{TOW}{C} \right)^D \left( 1 + \frac{SO_2}{E} \right)^F \left( 1 + \frac{Cl}{G} \right)^H e^{J(T+T_0)} \quad (47)$$

Where:

- $y$  = corrosion loss [ $\mu\text{m}$ ]
- $t$  = exposure time (years)
- TOW = time-of-wetness (h/years)
- $SO_2$  = sulfur dioxide concentration [ $\mu\text{g}/\text{m}^3$ ]
- $Cl$  = chloride deposition rate [ $\text{mg}/\text{m}^2/\text{day}$ ]
- $T$  = air temperature
- $A, B, C, D, E, F, G, H, J, T_0$  are empirical coefficients.

First part of the model is the time function, considering even long term, the second part of the model is a series of four environmental adjustment factors: TOW, sulfur dioxide, salinity, and temperature. Model than was calibrated using test comings from thirteen countries with different environmental parameters (Figure 93). This calibration program was called ISO CORRAG.

Country	sites	Atmosphere
Canada	1	I
Czechoslovakia	3	U, I, R
Germany	1	I
Finland	3	U, R
France	9	M, R, I, U
Japan	3	U
Norway	6	U, I, M
Spain	4	U, R, I, M
Sweden	3	U, M
United Kingdom	4	U, M, R, I
United States	5	R, U, M, I
Soviet Union	4	M, U, R

Note: I=Industrial; U=Urban; R=Rural; and M=Marine.

Figure 93: Test sites atmosphere for (Klinesmith, McCuen, & Abrecht, 2007) model.

Four different materials were tested: carbon steel, zinc, copper and aluminum, each of these with two different shapes. (Figure 94) Report the values of the coefficient for all the analyzed cases.

Materials	Types of specimens	Equation coefficients					
		A	B	D	F	H	J
CS	Flat	13.4	0.98	0.46	0.62	0.34	0.016
CS	Helix	19.7	0.05	0.46	0.62	0.34	0.016
Z	Flat	0.16	0.36	0.24	0.82	0.44	0.05
Z	Helix	0.26	0.05	0.24	0.82	0.44	0.05
C	Flat	0.46	0.15	0.02	0.38	0.46	0.02
C	Helix	0.78	0.22	0.02	0.38	0.46	0.02
A	Flat	0.094	0.05	0.23	1.14	0.42	0.01
A	Helix	0.27	0.05	0.23	1.14	0.42	0.01

Note: CS=carbon steel; Z=zinc; C=copper; and A=aluminum.

Figure 94: Coefficients of the model (with  $C=3800$ ,  $E=25$ ,  $T_0 = 20$ ) (Klinesmith, McCuen, & Abrecht, 2007)

The effect of the single parameter was than analyzed and plotted by (Klinesmith, McCuen, & Abrecht, 2007) for different materials and specimens shape, specifying that the same trend is shown in the other specimens (changing material and/or shape). These results are reported in (Figure 95, Figure 96, Figure 97 and Figure 98).

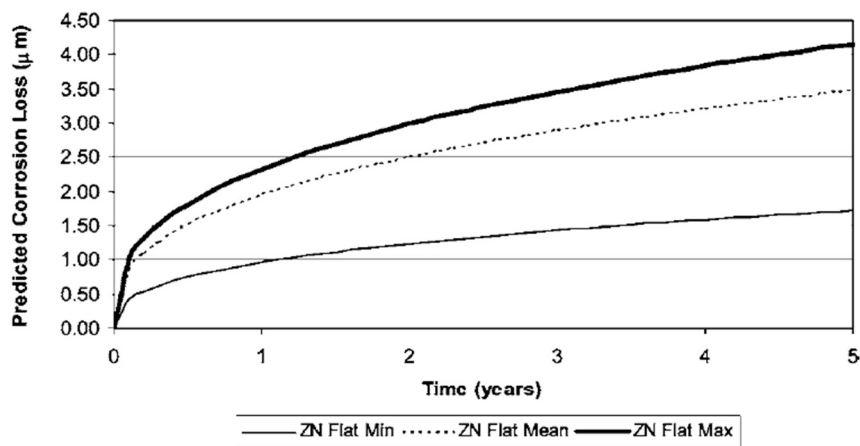


Figure 95: Effect of time-of-wetness on predicted corrosion loss as function of time for flat zinc specimens (Klinesmith, McCuen, & Abrecht, 2007)

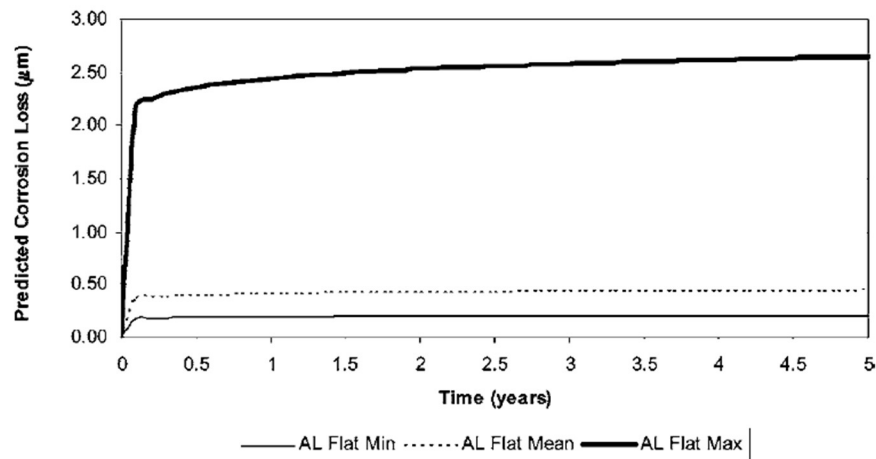


Figure 96: Effect of sulfur dioxide on predicted corrosion loss as a function of time for flat aluminum specimens (Klinesmith, McCuen, & Abrecht, 2007)

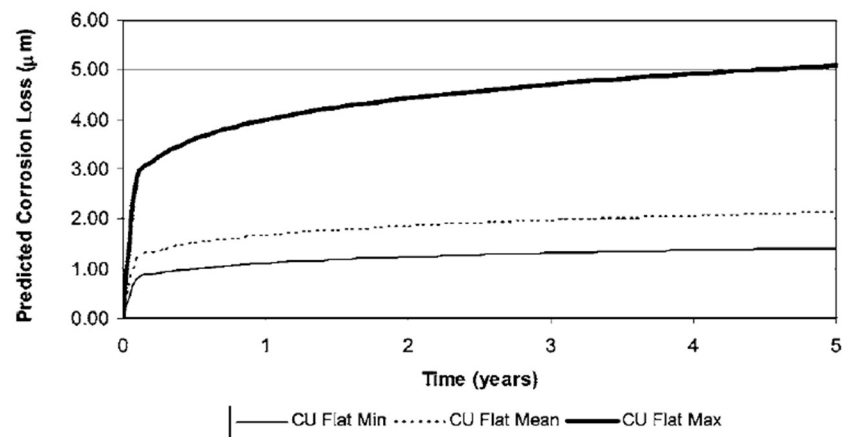


Figure 97: Effect of salinity on predicted corrosion loss as a function of time for flat copper specimens (Klinesmith, McCuen, & Abrecht, 2007)

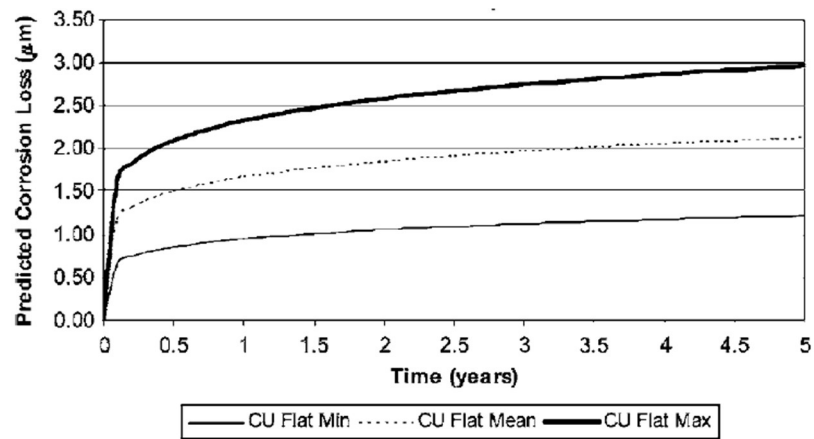


Figure 98: Effect of temperature on predicted corrosion loss as a function of time for flat copper specimens (Klinesmith, McCuen, & Abrecht, 2007)





## 6 STUDY CASES

This chapter aims to highlight corrosion processes present on safety nets installed in the municipality of Tricase in the province of Lecce. These nets are designed to protect pedestrians and vehicles from falling rocks, which threaten the roads running through these rock formations. As can be seen from the photographic documentation, the rock masses are not very large, but they are in close contact with the provincial road, so the danger has an inherently high value. The objective is to analyze the environmental class of the surrounding area, in accordance with ISO 9223:2012, to highlight the relationship between the properties defined by the environmental scenario and the corrosive processes that occur. The environment where these nets are present is characterized by a strong presence of saltwater, highly variable relative humidity, and windy cycles with speeds reaching 30 km/h.

### 6.1 GEOGRAFICAL IDENTIFICATION OF THE CASE STUDY

The photographic documentation refers to four different cases in the province of Lecce (Puglia), one inland, on the SP76, near the municipality of Specchia, right at the first hairpin bend (see Figure 99); the other three along the Adriatic coast along the SP 358, below the municipality of Marina Serra (see Figure 100).

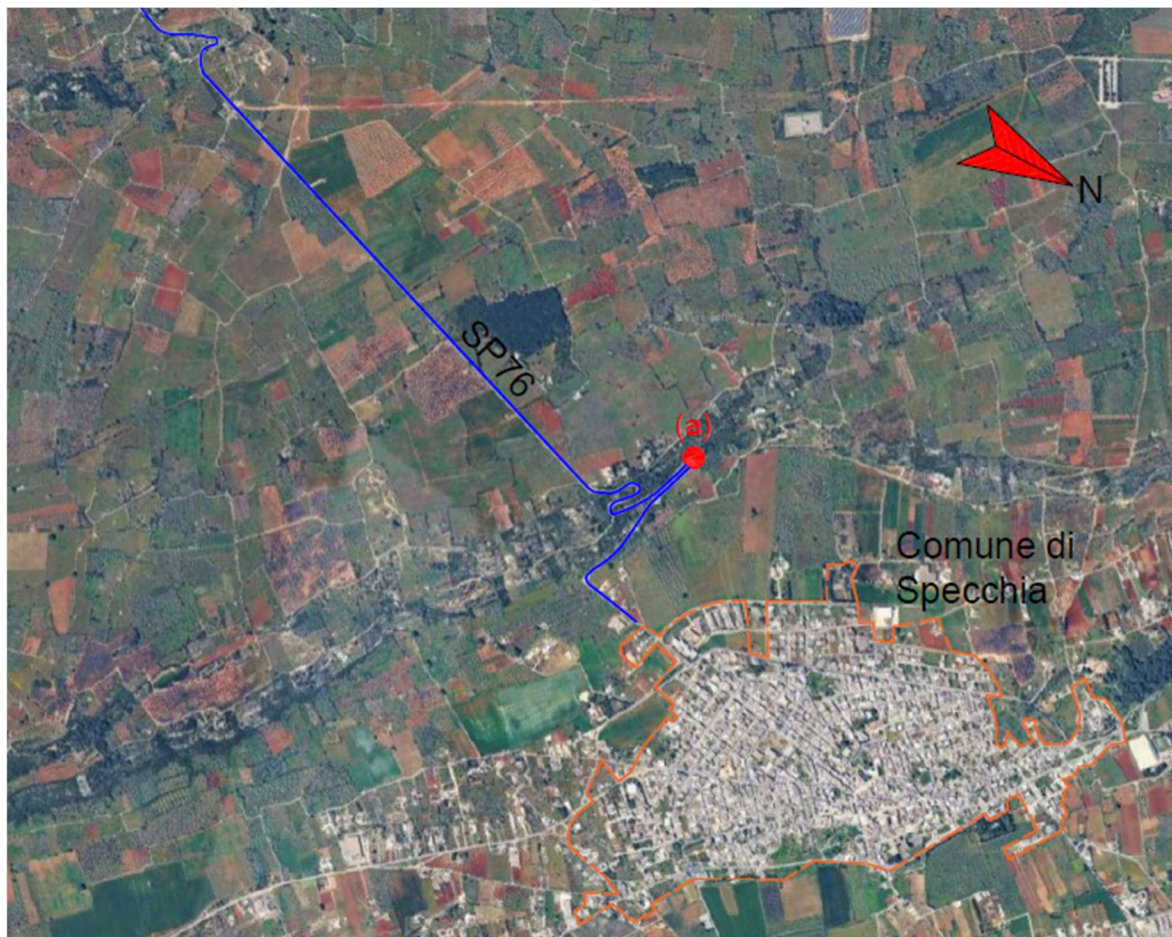


Figure 99: Geolocation of photographic documentation: (a) inland case.



Figure 100: Geolocation of photographic documentation: (b) - (c) - (d) seaside cases.

(Table 30) gives information about geo-localization, altitude, distance from the sea and municipality of the four sites taken from google earth.

	Altitude above the sea [m]	Latitude	Longitude	Distance from see [m]	Municipality
Figure 99 case (a)	155,66	39° 56' 02" N	18° 17' 14" E	9100	Specchia
Figure 100 case (b)	118,52	39° 54' 14" N	18° 23' 22" E	120	Tricase
Figure 100 case (c)	124,77	39° 53' 46" N	18° 23' 36" E	310	Tricase
Figure 100 case (d)	84,61	39° 52' 51" N	18' 23' 45" E	250	Corsano

Table 30 Geo-localization, altitude, distance from the sea and municipality of the study cases (a), (b), (c) and (d).



## 6.2 PHOTOGRAPHIC DOCUMENTATION

In this chapter, photographic documentation is provided of the four case studies introduced in chapter **Errore. L'origine riferimento non è stata trovata.**, The documentation start with an image framing the site of the element followed by a series of images highlighting the corrosion condition of the individual components of the safety device

The first case presented is the inland case study, named (a) in Figure 99:



*Figure 101: framing of the element (a)*





*Figure 102: Zinc coating corrosion of steel bar and anchor system.*

The next cases reported concern the corrosion process of the along seaside protective devices: Study case (b) in (Figure 100), is the first analyzed case, positioned along the seaside on the provincial road 358, the framing (Figure 103) shows that the rock wall that generates the danger does not have significant development, however it is located right next to the lane, which in addition lacks a shoulder.



*Figure 103: framing of the element (b)*

From Figure 104 the typology of the net can be highlighted, resulting in a hexagonal mesh. From Figure 105 the coatings used can be detached, resulting in a cover paint that is almost consumed, under which a zinc coating is placed, it is recognizable from the typical white rust that affect zinc at the beginning of its natural corrosion process. This aspect is detached only at the end of the net, probably due to the free movement that causes the net to come into contact with the surrounding vegetation.



*Figure 104: Wire mesh used for the element (b)*



*Figure 105: Used coatings for the element (b)*



Unlike the previous case the rope does not present any corrosion process (Figure 106); while the anchor, embedded in a concrete curb, shows, like the previous case, a strong process of degradation



*Figure 106: State of the rope of the case (b)*



*Figure 107: State of the anchor of the case (b)*

Study case (c) in (Figure 100) is quite like the case (b), with two strong important differences, it is nearer to the sea, and it is more exposed. Figure 108 of the framing of the element clearly shows that the other side, with respect to the protection device, is quite open.



*Figure 108: framing of the element (c)*

These two aspects have led to a greater deposition of  $\text{Cl}^-$ , which has accelerated the corrosion process as can be seen from the fact that both the mesh and the anchors show signs of corrosion (Figure 109 and Figure 110).



In addition, even the mesh connected to the anchor has lost its paint coating, and the protective zinc layer has begun to corrode.



*Figure 109: State of the wire mesh of element (c)*



*Figure 110: State of the anchor of the element (c)*

Study case (d) in (Figure 100) presents a different configuration, respect the previous two. The exposition and the distance from sea is like the case (c), probably due to the orientation of the barrier that faces the Sud-est direction (main direction of the wind blowing), while the case (c) faces the Nord-est direction. Framing is shown in Figure 111.



*Figure 111: Framing of the element (d)*



The configuration of this case is composed by ropes that run along the nets, consolidated to the rock through the use of steel plates, on which anchors are installed, this result in a grader area of deposition for Cl<sup>-</sup> and so in a greater corrosion of the elements, as can be seen from Figure 112.



*Figure 112: Anchor plate and anchor system of the element (d)*

### **6.3 ENVIRONMENTAL CLASS OF THE STUDY CASES IN ACCORDANCE WITH ISO 9223:2012**

(BSI, 2012) establishes a classification system for the corrosivity of atmospheric environments. It was introduced in chapter 5.1, providing all the information needed for understanding, the possible methodology for the evaluation, the sign language related and the parameters computed.

In particular, (BSI, 2012) clarify that the corrosivity of atmospheric environment can be classified either by determination of the corrosivity based on corrosion rate measurement of standard specimen, or, where this is not possible, by estimation of the corrosivity based on environmental information; since no studies have been performed in specimens corrosion and no information are present, the evaluation will be lead using the second approach.

(BSI, 2012) gives equations for steel Eq. (24-26), zinc Eq. (27-29), copper Eq. (30-32) and aluminum. For the scope of this chapter, the interesting ones are only the ones related to steel and zinc, which are reported in Eq (48) and (49).

$$r_{corr} = 1,77 \cdot P_d^{0,52} \cdot \exp(0,020 \cdot RH + f_{St}) + 0,102 \cdot S_d^{0,62} \cdot \exp(0,033 \cdot RH + 0,040 \cdot T) \quad (48)$$

$$r_{corr} = 0,0129 \cdot P_d^{0,44} \cdot \exp(0,046 \cdot RH + f_{Zn}) + 0,0175 \cdot S_d^{0,57} \cdot \exp(0,008 \cdot RH + 0,085 \cdot T) \quad (49)$$

Where:

- $r_{corr}$  is first year corrosion rate of metal, expressed in micrometers per year ( $\mu\text{m/a}$ )
- $T$  is the annual average temperature, expressed in degrees Celsius ( $^{\circ}\text{C}$ );
- $RH$  is the annual average relative humidity, expressed as a percentage (%);
- $P_d$  is the annual average  $\text{SO}_2$  deposition, expressed in milligrams per square meter per day [ $\text{mg}/(\text{m}^2\text{d})$ ];
- $S_d$  is the annual average  $\text{Cl}^-$  deposition, expressed in milligrams per square meter per day [ $\text{mg}/(\text{m}^2\text{d})$ ].

### 6.3.1 Relative Humidity

Values of relative humidity are taken from the weather archive of (ilmeteo, 2025), related to the municipality of Specchia and coming from the meteorological station located in Ruffano at the coordinates  $39^{\circ} 58' 34'' \text{ N}$ ;  $18^{\circ} 16' 7'' \text{ E}$  with a distance from the point (a) of 4,6km. To detect the temperatures the company uses a numerical model called Zeus, which gives reasonable values, even for location sited far from stations with a range from 5 to 15km.

This parameter is strongly influenced by the presence of sea near to the location, for this reason two values of this parameter are researched, one for the inland case and the other for the seaside case.

First value, related to the inland case, comes from the station sited in the municipality of Specchia, that provides values of relative humidity each month (Table 31), from which an average value is extracted:

Month	RH [%]
January	87
February	84
March	81
April	75
May	68
June	52
July	58
August	64
September	69
October	79
November	85
December	86

Table 31: Relative Humidity of the inland case

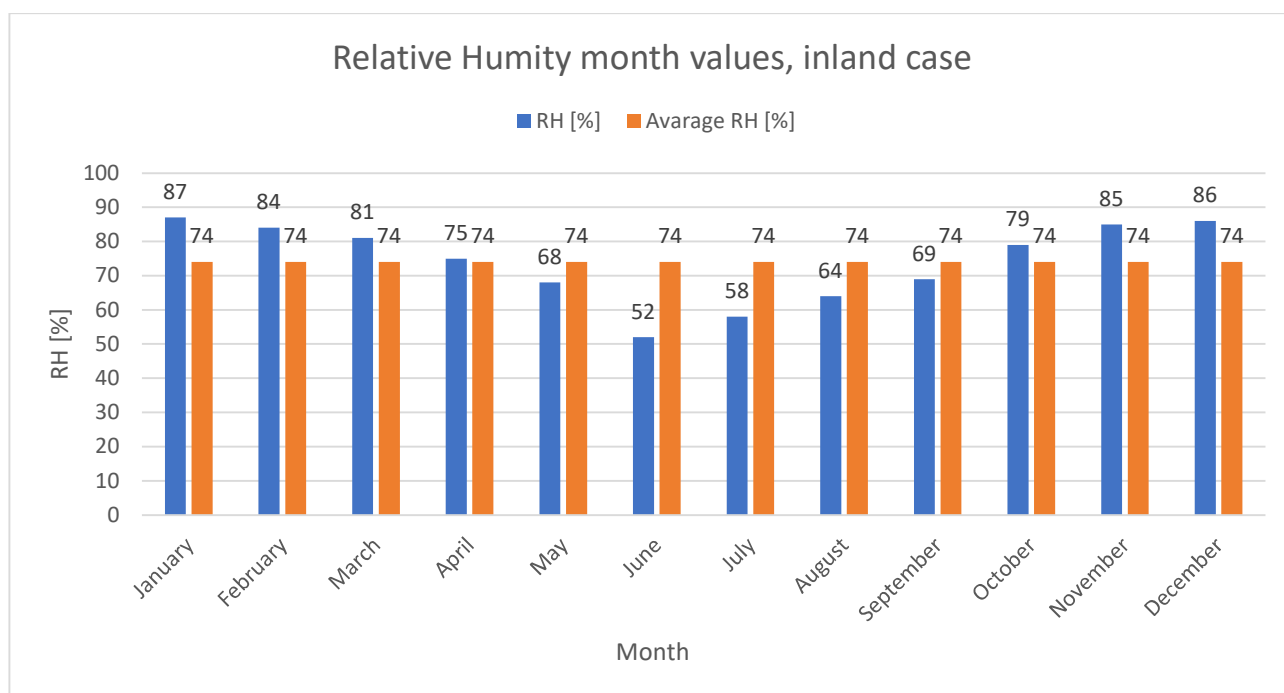


Figure 113: Histogram of Relative Humidity for the inland case, plotting month values and average.

The average computed value is equal to 73,66%, roundable to 74%.

Second value of relative humidity, associated to the seaside cases, is taken from the same archive of (ilmeteo, 2025) for the municipality of Marina Serra. This value comes from the meteorological station sited in the municipality of Alessano, at the coordinates 39° 52' 59" N; 18° 20' 19" E with a distance of 4,9km from the site (b), 4,8km from point (c) and 4,8km from point (d), considering the similarity of the distances a single value representative value of the three sites is taken.

Meteorological station provides values of relative humidity each month (Table 32), from which an average value is extracted:

Month	RH [%]
January	83
February	82
March	78
April	71
May	69
June	59
July	58
August	59
September	62
October	63
November	76
December	82

Table 32: Relative Humidity of the seaside case

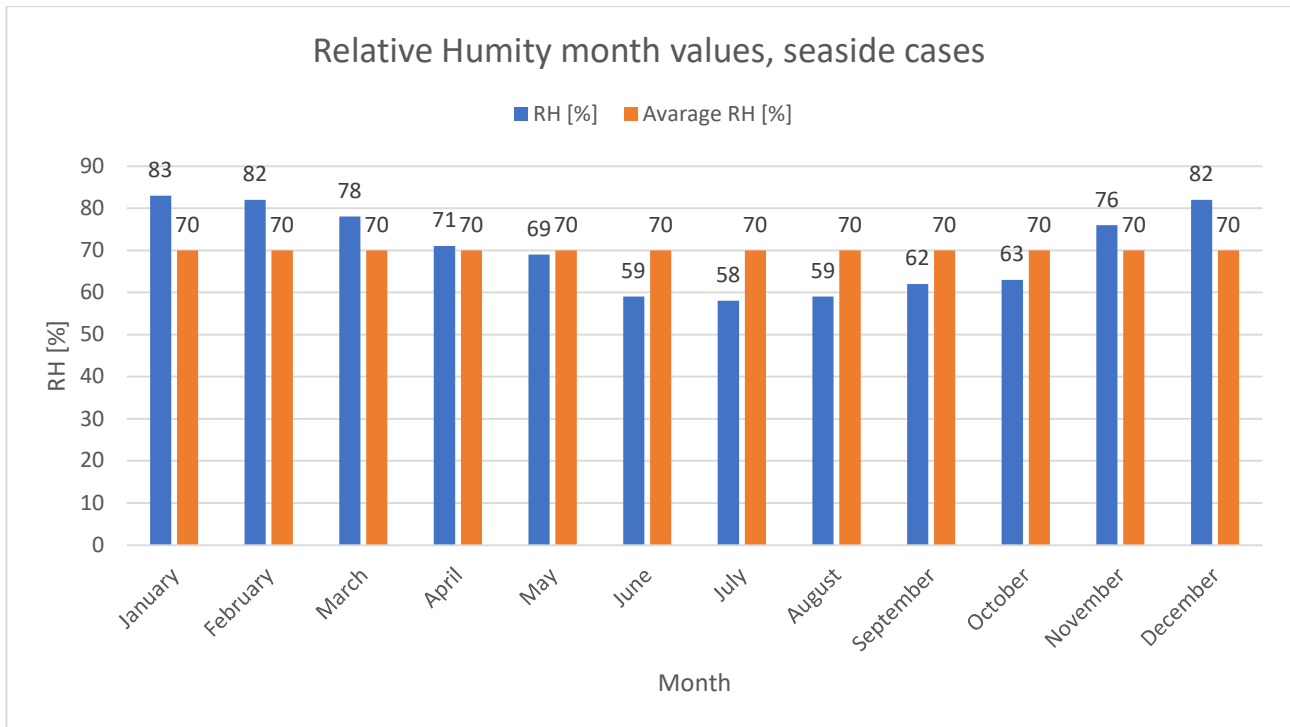


Figure 114: Histogram of Relative Humidity for the seaside case, plotting month values and average.

The average value is computed equal to 69,91%, roundable to 70%.

### 6.3.2 Average temperature

Data related to the average temperature are taken from the same station of relative humidity, (ilmeteo, 2025). Similarly to relative humidity the values researched are two for the two different locations of the cases. The found values are reported in Table 33 and Table 34

Month	T [°C]
January	11
February	10,1
March	13,1
April	15,4
May	19
June	25,9
July	27,9
August	26,5
September	23,5
October	17
November	12,4
December	9,4

Table 33: Average Temperature for the inland case

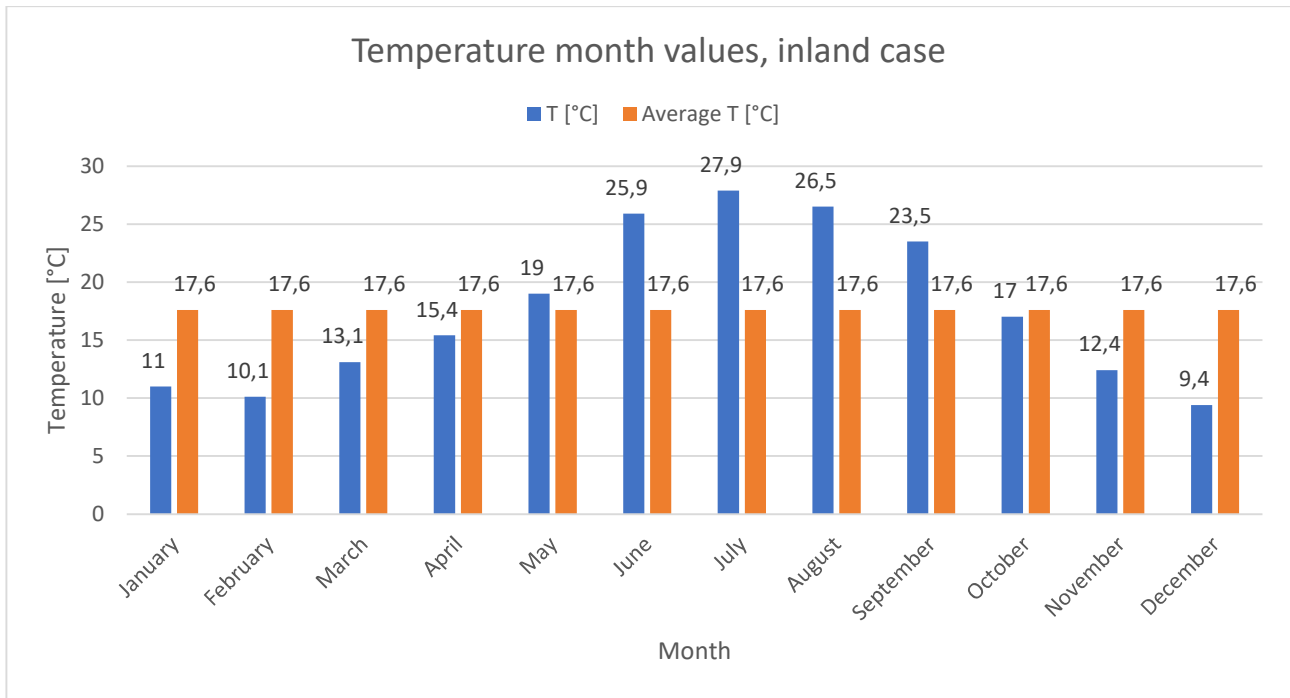


Figure 115: Histogram of Temperature for the inland case, plotting month values and average.

The average value is computed equal to 17,6 °C.

Month	T [°C]
January	13
February	10
March	12,3
April	16
May	18
June	24
July	26,2
August	29,4
September	27
October	20,1
November	17,2
December	12,8

Table 34: Average Temperature of the seaside case

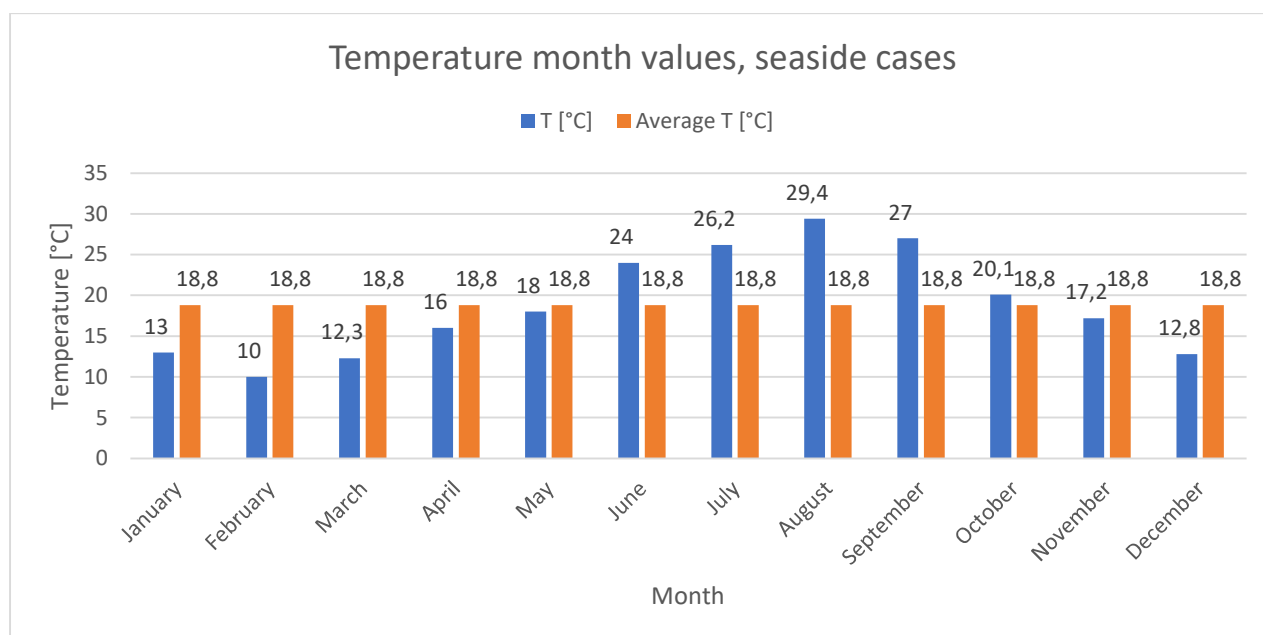


Figure 116: Histogram of Temperature for the seaside case, plotting month values and average.

The average value is computed equal to 18,9 °C.

### 6.3.3 SO<sub>2</sub> deposition

To determine this value, the data published from (ARPA Puglia, 2023) were analyzed. In particular the regional authority, published data related to 2023, so these values are taken to estimate the SO<sub>2</sub> parameter. The data acquired refers to the municipality of Maglie (ARPA Puglia, 2023), the nearest one, among the station present, to the analyzed cases; it is sited in “Via Don. L. Sturzo, 4” at the coordinates 40° 07' 23" N; 18° 17' 38" E. The distance from the site of case (a) is 21km while from cases (b), (c) and (d) is respectively 26, 26 and 28 km.

Data on ARPA website refers to a value per single day, (Table 35) reports yet the monthly average.

Month	SO <sub>2</sub> deposition [mg/(m <sup>2</sup> d)]	SO <sub>2</sub> volumetric concentration [μg/(m <sup>3</sup> )]
January	2,656	3,32
February	2,464	3,08
March	1,776	2,22
April	1,744	2,18
May	1,368	1,71
June	1,752	2,19
July	2,712	3,39
August	2,352	2,94
September	2,64	3,3
October	1,2	1,5
November	1,008	1,26
December	1,544	1,93

Table 35: SO<sub>2</sub> volumetric concentration and deposition on the meteorological station of Maglie

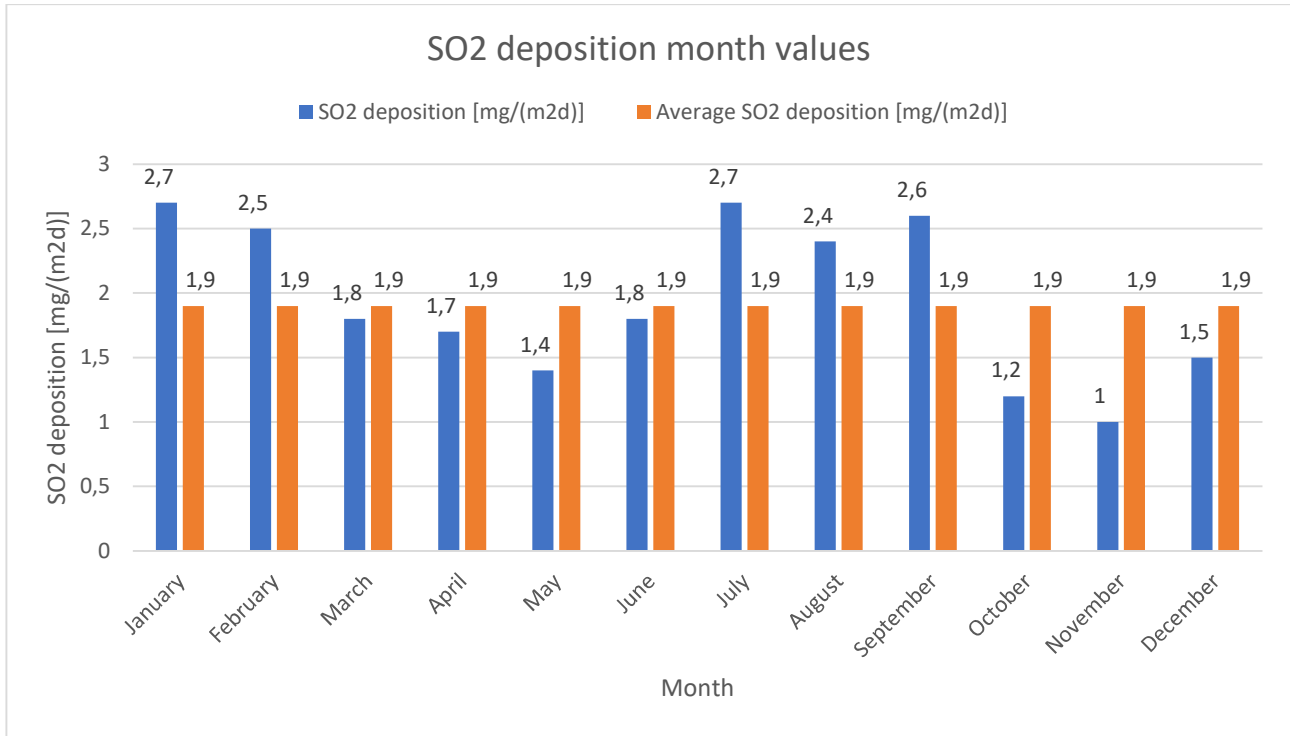


Figure 117: Histogram of SO<sub>2</sub> deposition, plotting month values and average.

The values that (ARPA Puglia, 2023) gives are volumetric concentration, (BSI, 2012) gives a relation between volumetric concentration and deposition rate, expressed in Eq. 50

$$P_d = 0,8 P_c \quad (50)$$

Where  $P_d$  is the deposition rate and  $P_c$  is the volumetric concentration. SO<sub>2</sub> deposition average value, based on a year is equal to 1,928mg/(m<sup>2</sup>d).

#### 6.3.4 Cl- deposition

To measure the Cl<sup>-</sup> deposition, specific surveys are needed, with normalized procedures (such as wet-candle). Cl<sup>-</sup> deposition is not a standard parameter computed for the quality air studies carried out by regional authorities such as ARPA, it neither is computed from the meteorological station. For these reasons to estimate the deposition rate an empirical model, based on the distance from the sea, is used.

It must be specified that this parameter refers only to the seaside case, considering that the inland case presents no chloride deposition.

The model used for this computation is the one proposed by (Guerra, Castaneda, Corvo, Howland, & Rodriguez, 2019). According to this study, the chloride deposition rate can be roughly computed. With the Eq 51

$$[Cl] = -1,99 - 1,08 \times (RH) + 5,53 \times (T) + 15,25 (WS) \quad (51)$$

Where: RH is the average value of the relative humidity, T is the average value of the temperature and WS is the average value of the wind speed.

Relative humidity and temperature are taken respectively from chapters 6.2.1 and 6.2.2. taking values equal to: RH = 70% and T = 18,9 °C



Data related to wind speed, in the year 2025 are taken from the historical archive of the website (ilmeteo, 2025). Information are detected every month, and are reported below in Table 36 within other parameters and results of Eq. 51 for Cl<sup>-</sup> deposition value monthly:

Month	Wind Speed [km/h]	T [°C]	RH [%]	[Cl <sup>-</sup> ] [mg/m <sup>2</sup> d]
January	20,4	13	83	66,7
February	18,5	10	82	43,12
March	18	12,3	78	58,04
April	26,5	16	71	122,06
May	26,5	18	69	135,29
June	33	24	59	206,80
July	21,66	26,2	58	172,01
August	30	29,4	59	223,96
September	32,75	27	62	219,09
October	32,8	20,1	63	180,07
November	40	17,2	76	180,49
December	33	12,8	82	120,03

Table 36: Average value for the Wind Speed for the seaside case

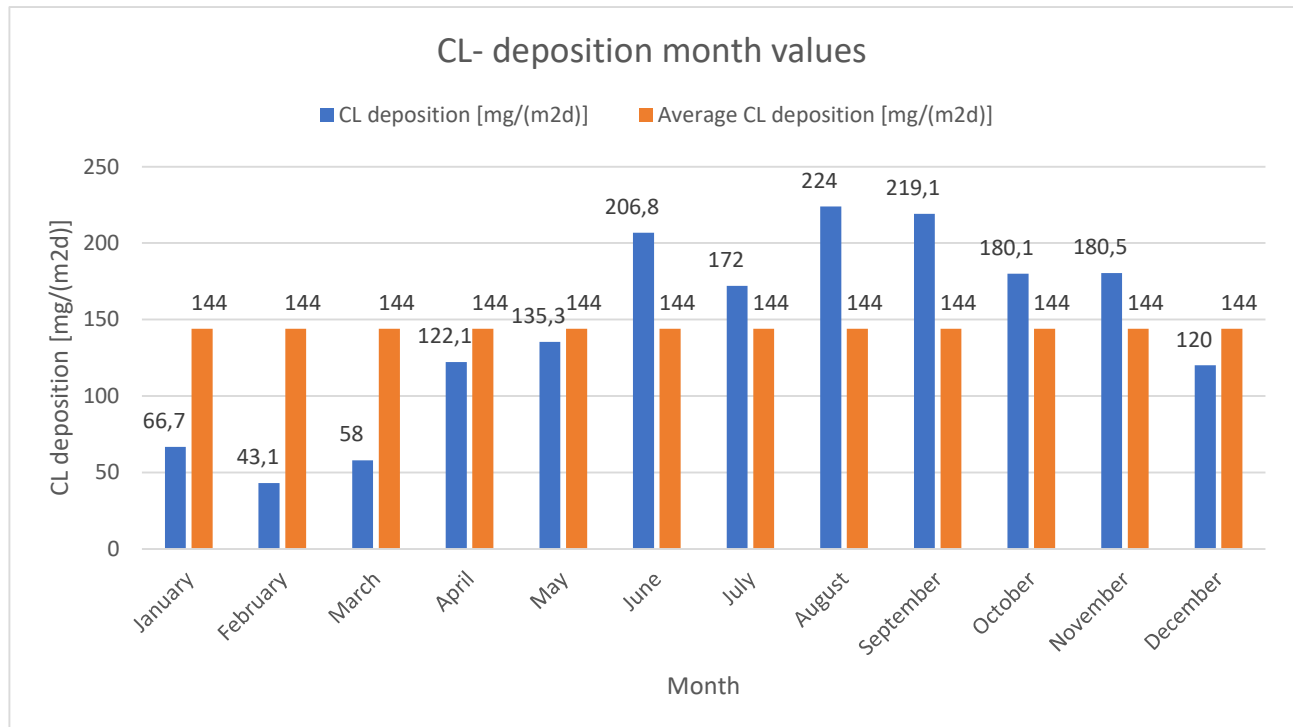


Figure 118: Histogram of CL- deposition, plotting month values and average.

The average value of the wind velocity is: 27,75 km/h = 7,7 m/s

The average value of Cl<sup>-</sup> computed with (Eq. 51) is equal to: 144,352 mg/(m<sup>2</sup>d)

Needed values of temperature, relative humidity, annual average SO<sub>2</sub> deposition and Cl<sup>-</sup> deposition, to be used into (Eq. 48 and 49), are summarized and reported in (Table 37)

	T expressed in [°C]	RH expressed as %	SO <sub>2</sub> deposition expressed in [mg/m <sup>2</sup> d]	Cl <sup>-</sup> deposition expressed in [mg/m <sup>2</sup> d]
Inland environment (case a)	17,6	74	1,928	-
Seaside environment (case b-c-d)	18,9	70	1,928	144,352

Table 37: Summary values of the needed parameter for the corrosion rate computation

To perform the computation using dose-response function, values boundaries reported in (Table 28) must be respected; verifications on the obtained data brings to a fulfillment of the request.

### 6.3.5 Corrosivity category computation

To assess the verification of the corrosivity category, the corrosion rate of steel and zinc are needed Eq. (44) and (45). To compute this value, the parameter  $f_{St}$  and  $f_{Zn}$  must be computed, these are factors associated with steel and zinc in function of the temperature. These factors can be computed using Eq. (52) and (53)

$$f_{St} = 0,150 \cdot (T - 10) \text{ for } T \leq 10^{\circ}C \quad (52)$$

$$f_{St} = -0,054 \cdot (T - 10) \text{ for } T \geq 10^{\circ}C$$

$$f_{Zn} = 0,038 \cdot (T - 10) \text{ for } T \leq 10^{\circ}C \quad (53)$$

$$f_{Zn} = -0,071 \cdot (T - 10) \text{ for } T \geq 10^{\circ}C$$

Leading to:

- $f_{St}$  inland case = -0,4104
- $f_{Zn}$  inland case = -0,5396
- $f_{St}$  seaside case = -0,4806
- $f_{Zn}$  seaside case = -0,6319

Using now Eq (48 and 49) the corrosion rate of steel and zinc can be computed:

- $r_{corr}$  steel inland case = 7,25  $\mu\text{m/a}$
- $r_{corr}$  zinc inland case = 0,30  $\mu\text{m/a}$
- $r_{corr}$  steel seaside case = 53,92  $\mu\text{m/a}$
- $r_{corr}$  zinc seaside case = 2,82  $\mu\text{m/a}$

Using Table 21 from (BSI, 2012) evaluation, it can be highlight that the corrosion category for the site far from seaside preset a low level of corrosivity, classified as a C2 category; while for the three cases along the sea side the corrosivity level increase to high, classified as C4, this because into the evaluation of the  $r_{corr}$  for the seaside elements the parameter related to chloride deposition is present, and is even huge; while in the inland case no chloride deposition is present. Further comments are offered in the conclusions at chapter 6.5.

### 6.3.6 Maximum and minimum values of zinc corrosion: SO<sub>2</sub> statistical analysis

In this paragraph, the variation of SO<sub>2</sub> value is reported. Considering that the value reported in the previous chapter, it comes from an average on monthly value, and this monthly value comes from the values of the single days (ARPA Puglia, 2023), a standard deviation of the parameter can be computed using the Eq (54).

$$\sigma = \sqrt{\sum_{i=1}^N \frac{(xi - \mu)^2}{N}} \quad (54)$$

Where  $\mu$  is the average value and N is the number of elements composing the statistical analysis

This analysis aims to define the variation of the corrosion rate of zinc in the marine environment, since it is the most aggressive environment. The results in terms of average and standard deviation per each month, related to the SO<sub>2</sub> deposition, are reported in Table 38

Month	Average [mg/m <sup>2</sup> d]	Standard deviation
January	2,656	0,886
February	2,467	0,523
March	1,781	0,494
April	1,745	0,401
May	1,368	0,369
June	1,754	0,322
July	2,714	1,348
August	2,348	0,410
September	2,64	0,428
October	1,2	0,472
November	1,01	0,360
December	1,54	0,896

*Table 38: Average values and standard deviation of SO<sub>2</sub> deposition*

It should be noted that performing the average of month values is equal to the value obtained in 6.3.3.

From Table 38 two values of SO<sub>2</sub> deposition can be obtained, that are computed by adding and subtracting the standard deviation to the average. This brings to SO<sub>2</sub>max and SO<sub>2</sub>min each month, reported in Table 39.

Month	SO <sub>2</sub> min [mg/m <sup>2</sup> d]	SO <sub>2</sub> max [mg/m <sup>2</sup> d]	$r_{corr\ min}$ [μm/a]	$r_{corr\ max}$ [μm/a]
January	2,13	3,54	2,83	2,89
February	1,94	2,99	2,83	2,87
March	1,26	2,27	2,79	2,84
April	1,22	2,15	2,78	2,84
May	0,84	1,74	2,75	2,81
June	2,19	3,03	2,84	2,88
July	1,83	3,70	2,82	2,90
August	2,12	3,05	2,83	2,88
September	0,68	1,63	2,74	2,81
October	0,49	1,49	2,72	2,80
November	1,02	1,90	2,77	2,82
December	1,41	2,83	2,80	2,87

*Table 39: monthly values of SO<sub>2</sub>min and SO<sub>2</sub>max deposition and corrosion rate max and min*

Using these values, it is possible to calculate the maximum and minimum corrosion rate; this is measured in micrometers per year, so it will be an annual value based on monthly data.  $r_{corr\ min}$  and  $r_{corr\ max}$ , which are reported in Table 39.

## 6.4 CORROSION RATE OF THE ZINC COATING WITH A LIFE PREDICTOR PROGRAM

The program used for this evaluation is the one proposed by (Zhang, s.d.), it is a prediction model that needs in input six weather and air pollution parameters, in order to evaluate life and corrosion rate of the zinc coating.

The required parameters (Figure 119) are: rain in [inches/year], sulfur dioxide in [ $\text{mg}/\text{m}^2\text{d}$ ], relative humidity in [%], Salinity in [ $\text{mg}/\text{m}^2\text{d}$ ], temperature in [ $^{\circ}\text{F}$ ] and sheltering conditions: open air, rain sheltered or indoor.

<b>Rain</b> (4.0 - 117.0 in/year) ?	<b>Sulfur Dioxide</b> (0.0 - 100.0 $\text{mg}/\text{m}^2\text{.day}$ ) ?	<b>Relative Humidity</b> (35.0 - 95.0%) ?
<input type="text"/> in/year	<input type="text"/> $\text{mg}/\text{m}^2\text{.day}$	<input type="text"/> %
<b>Salinity</b> (0.0 - 150.0 $\text{mg}/\text{m}^2\text{.day}$ ) ?	<b>Temperature</b> (32.0 - 81.0 $^{\circ}\text{F}$ ) ?	<b>Sheltering Condition</b> ?
<input type="text"/> $\text{mg}/\text{m}^2\text{.day}$	<input type="text"/> $^{\circ}\text{F}$	-Select-

Figure 119: Table of needed parameters for the program (Zhang, s.d.)

All the data needed are yet computed in previous chapter except for the rain; this parameter is taken from (meteoatlas, s.d.) that reports an average value of the annual rain equal to 688mm, that are equal to 27,08 inches/year.

The resulting corrosion rate of the zinc coating is equal to 3,9  $\mu\text{m}/\text{year}$ . Summary table of the inserted parameters and corrosion rate result is shown in (Figure 120)

Calculation of Corrosion Rate	
Rain	27.08 in/year
Salinity (Chlorides)	144.352 $\text{mg}/\text{m}^2\text{.day}$
Sulfur Dioxide	1.928 $\text{mg}/\text{m}^2\text{.day}$
Relative Humidity	70%
Temperature	66.02 $^{\circ}\text{F}$
Sheltering Condition	Open Air
<b>Corrosion Rate</b>	<b>3.9 <math>\mu\text{m}/\text{year}</math></b>

Figure 120: Corrosion rate of zinc and inserted parameter on the program of (Zhang, s.d.)

The results produced with this computation are perfectly in line with the ones produced with the dose response function. To be precise, a difference of 1  $\mu\text{m}/\text{year}$  is present, this difference is irrelevant considering that this

brings to a corrosion dimension greater of 1mm in 1000years. In fact, this little difference causes no variation in the evaluation of the corrosivity classification, resulting, even with this analysis, in a C4 class.

## 6.5 DISCUSSION ON THE OBSERVED DEGRADATIONS

A first comparison can be made on the Relative Humidity of the two environments analyzed: Figure 121

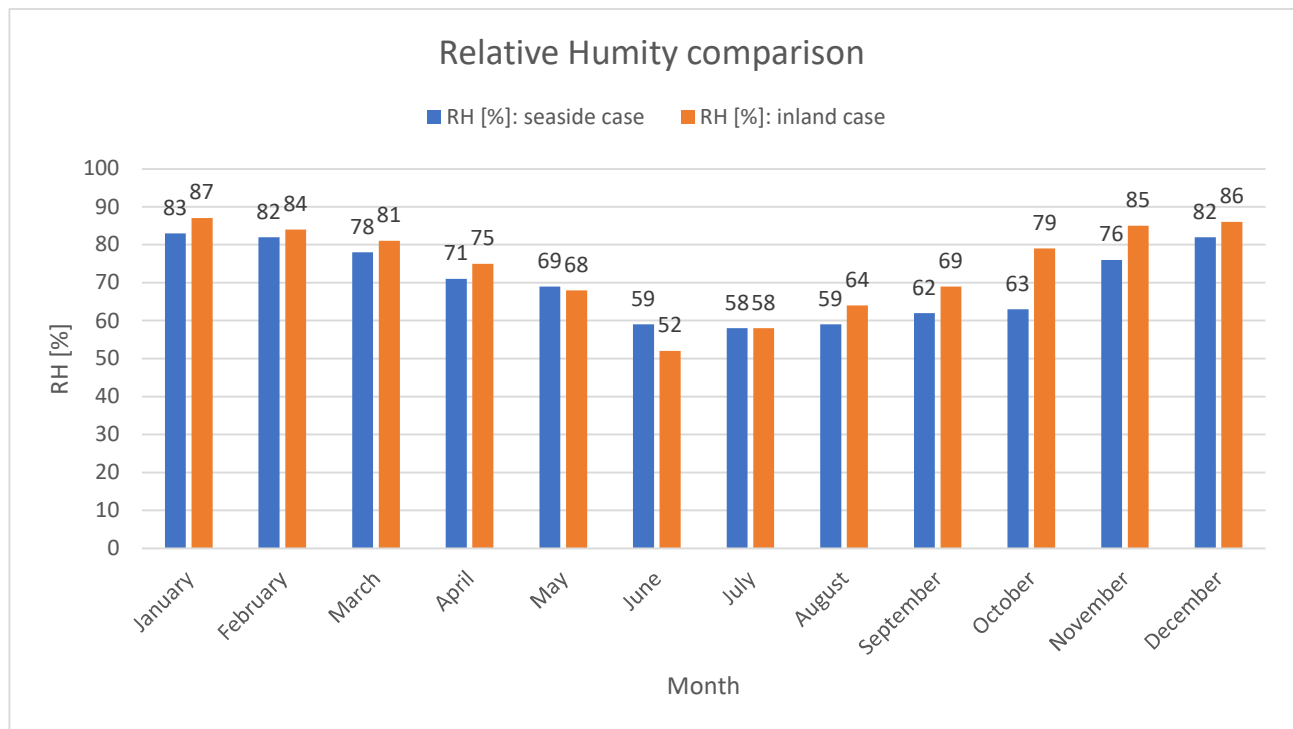


Figure 121: Relative Humidity comparison.

It can be noted that during the winter months, the relative humidity of coastal environments tends to be lower compared to that of urbanized inland areas due to a combination of thermodynamic and microclimatic factors. Near the sea, the air temperature is generally higher (assumption confirmed in Figure 122) and more stable than inland, thanks to the high thermal capacity of water, which dampens daily and seasonal temperature fluctuations. Since relative humidity (RH) depends on the ratio between the actual amount of water vapor present and the maximum amount the air can hold at a certain temperature (saturation point), an increase in temperature reduces the RH value, even if the vapor content remains the same. In contrast, in urbanized inland areas, during the winter the air is colder and therefore more likely to reach saturation, resulting in higher relative humidity values. Additionally, cities generate a particular microclimate, the urban heat island, which promotes local condensation of vapor (for example in the presence of pollutants or particulate matter), further increasing the perceived relative humidity.

During the summer months, relative humidity tends to be higher along the coasts and lower in urbanized inland areas, due to a different balance between temperature, evaporation, and atmospheric circulation. Near the sea, the ocean surface provides a continuous source of water vapor: the high surface temperatures of the water intensify evaporation, enriching the coastal air with absolute humidity (that is, the actual water vapor present). Even if the air temperature is high, and therefore the air's capacity to hold water vapor is greater, the strong evaporation keeps relative humidity at high levels. In addition, sea breezes and constant ventilation limit heat buildup and promote a more humid microclimate.

As reported above, the expected trend on temperature is inverted respect to the one of relative humidity, this is exposed in Figure 122

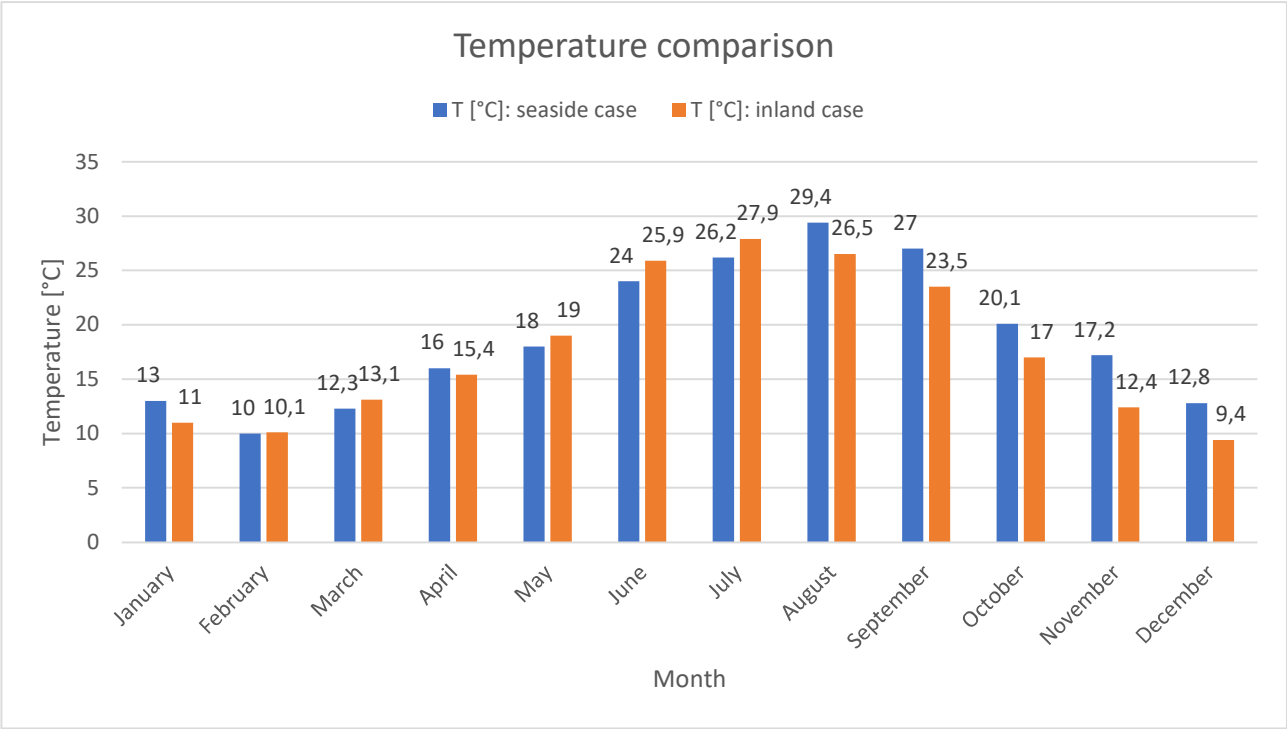


Figure 122: Temperature comparison.

Regarding the SO2 deposition, its value is low as reported in Figure 123

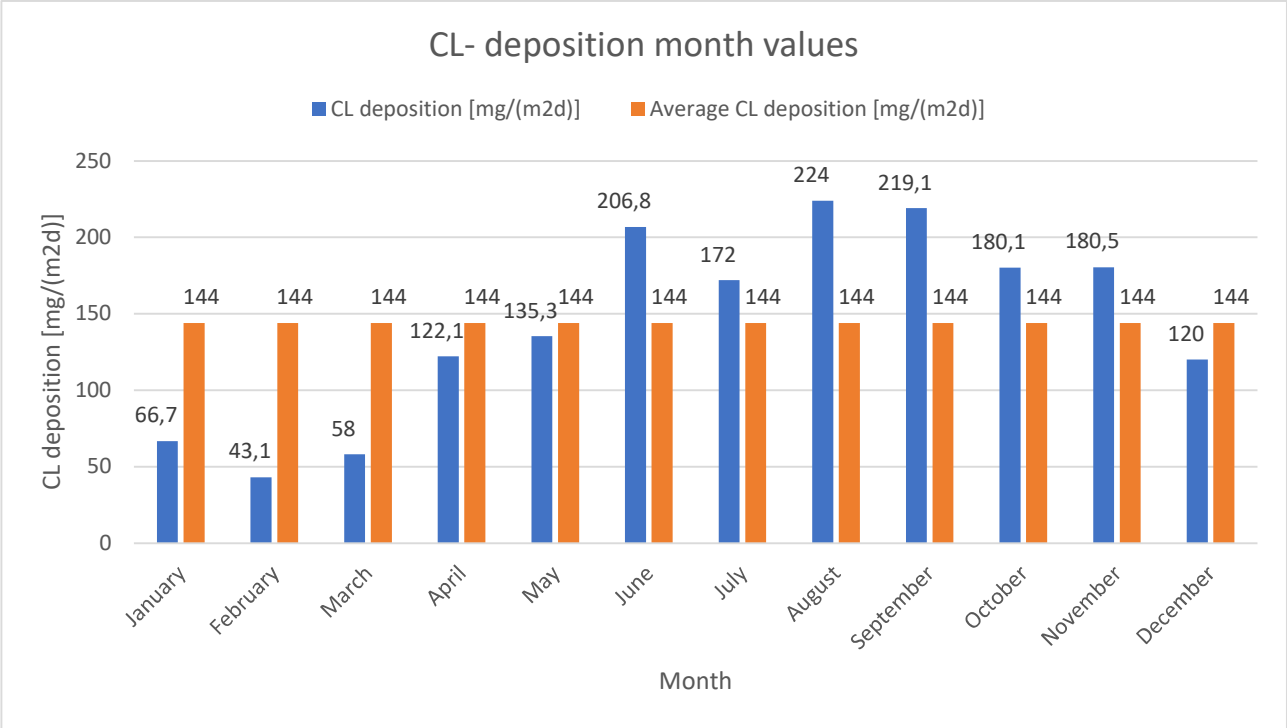


Figure 123: SO2 deposition: monthly values.

This is because the environment analyzed is a rural environment where no industries or intense traffic are present, and the value of SO2 deposition is associated to the car pollution, as can be seen, month with highest



values are the summer month and December, that are the month in which citizens move around the most. For this reason, the statistical analysis carried on variation of corrosion rate of zinc (chapter 6.3.6), bring to a gradient of the value irrelevant in terms of degradation velocity. The results of the analysis are reported in the chart presented in Figure 124.

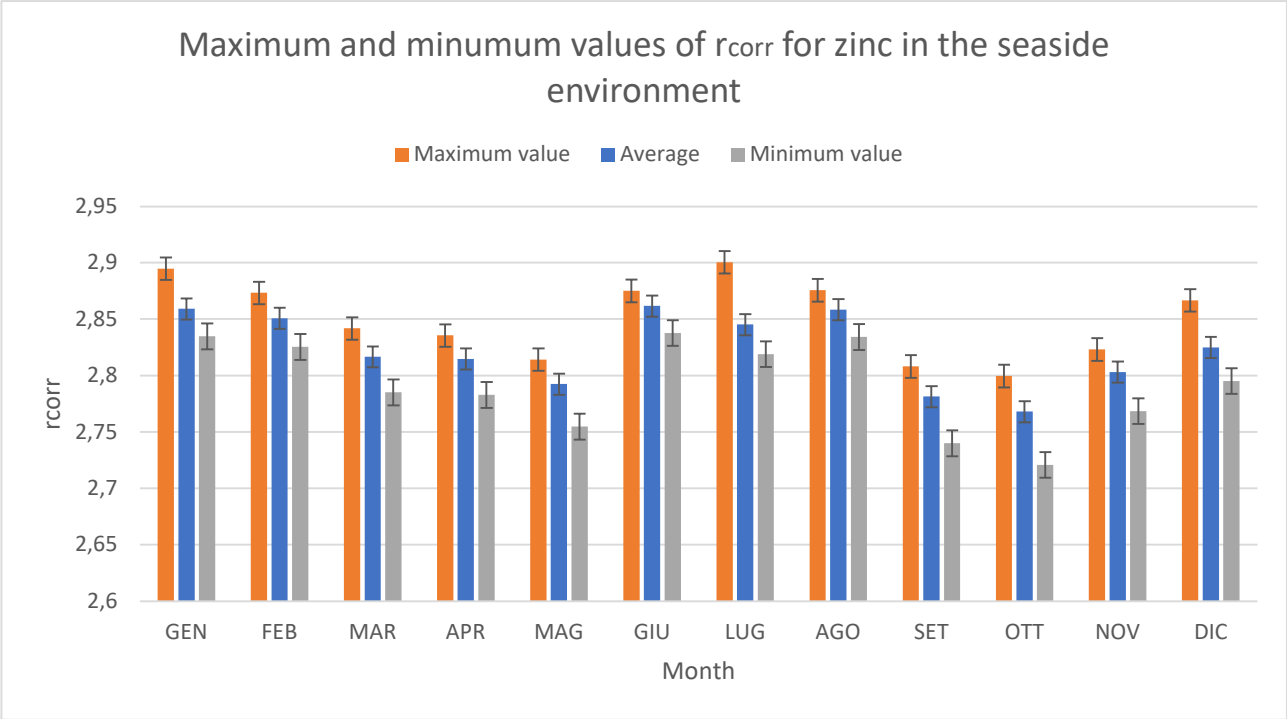


Figure 124: Maximum and minimum values of  $R_{corr}$  for zinc in the seaside environment.

More interesting aspect can be highlighted by analyzing the fraction related to SO<sub>2</sub> and to CL<sup>-</sup>, of corrosion rate computed. To this the produced charts are reported in Figure 125 and Figure 126

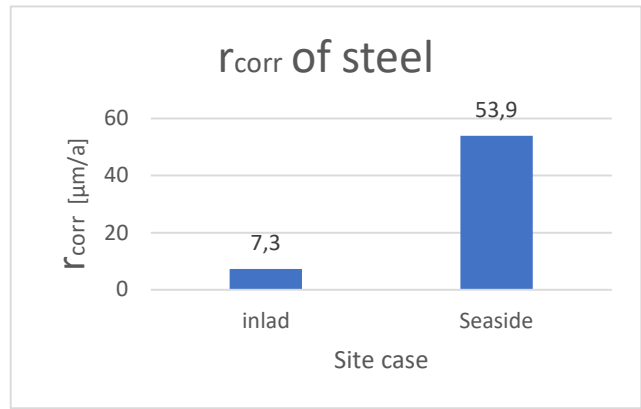


Figure 125: corrosion rate of steel

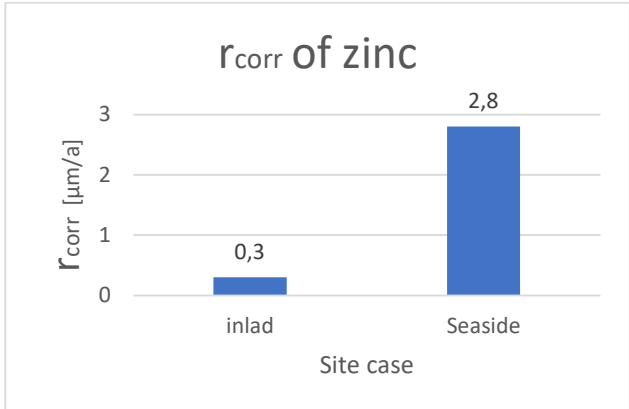


Figure 126: corrosion rate of zinc

A first consideration can be made on the difference between the value of corrosion rate for the inland case and for the seaside case, introduction of chlorides (CL<sup>-</sup>) brings to an increment of corrosion rate of about 10 times.

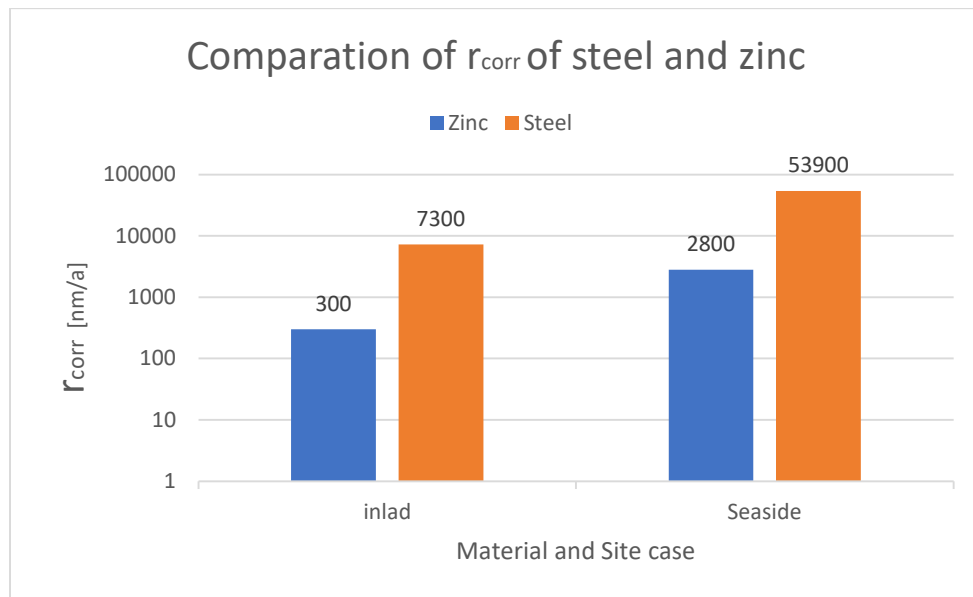


Figure 127: corrosion rate comparison between steel and zinc.

Figure 127 shows the difference between the corrosion rate of steel and zinc. To better appreciate the graph, the corrosion rate was converted to nanometers per year [nm/a], and a logarithmic scale was adopted. The analysis highlights a difference of one order of magnitude, as expected zinc is one of the best materials for coatings thanks to its high resistance to corrosion.

To conclude, Figure 128 and Figure 129 show the impact of SO<sub>2</sub> and Cl<sup>-</sup> in the corrosion rate calculation for both inland and seaside cases. As expected, the chloride component for the inland case is null, and so the totality of the corrosion rate is due to the SO<sub>2</sub>. When the case moves to the seaside, the corrosion rate shows a huge increment, and almost 90% of the corrosion rate is due to the chloride presence.

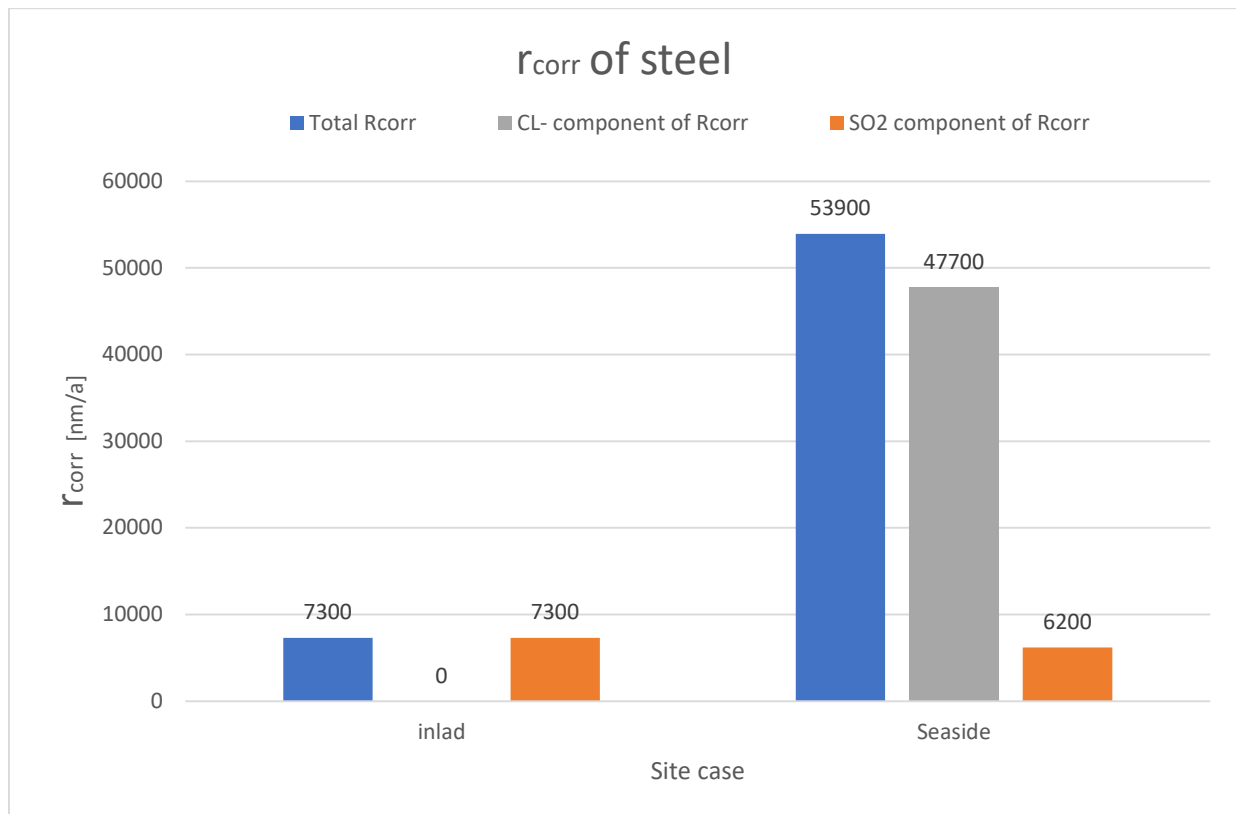


Figure 128: Impact of SO<sub>2</sub> and Cl<sup>-</sup> on the calculation of corrosion rate of steel.

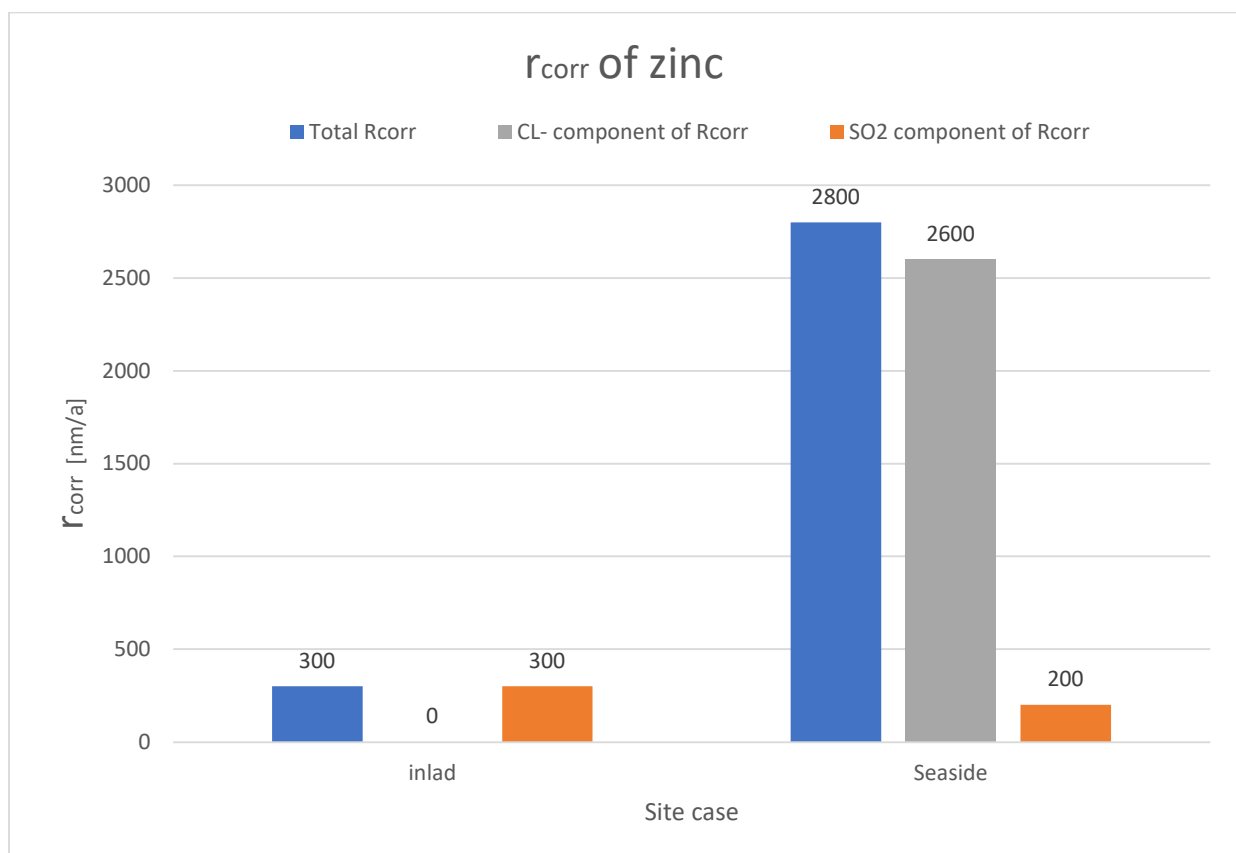


Figure 129: Impact of SO<sub>2</sub> and Cl<sup>-</sup> on the calculation of corrosion rate of zinc.

Further considerations can be made regarding the vegetation present around the devices, which can generally generate benefits or drawbacks on the corrosive processes affecting the networks. Vegetation can act as a windbreak, resulting in a lower rate of chlorine deposition, which, as reported in the calculation in Chapter 7, represents the main component of severe corrosion for devices installed along the coast, approximately 90%. Particular attention must also be paid to the negative aspects of vegetation, which could retain moisture near the devices or produce acidic organic substances, such as resins.

In conclusion, if the zinc coating thickness of the case studies and the exact installation date of the grids were known precisely, it would be possible, through the program of (Zhang, s.d.), to calculate the service life of the coating, thus obtaining a deadline by which to arrange for a replacement of the coating, so as not to compromise the mechanical properties of the structural elements and therefore safeguard against the hazard posed by rock masses along the coast.



## 7 CONCLUSION AND FINAL CONSIDERATIONS

This work focuses on the analysis of the degradation phenomenon affecting rockfall barriers, with particular attention to the corrosive process that compromises their service life. After describing the rockfall phenomenon, through the general definition of landslide and subsequently the detailed characterization of the phenomenon, followed by the classification of landslide events, the procedure used to evaluate rockfall risk was provided. The latter is calculated following the identification of the danger and, therefore, of the scenarios that may develop depending on the trajectory followed by the rock. To address the risk arising from these phenomena, an introduction to possible protection and prevention systems was given, specifying the details of the object of this thesis work: rockfall barriers.

An overview of the composition of rockfall barriers is provided, analyzing all its components from net fences to energy dissipation devices, in addition the design procedure related to the ONR 24810, and EUROCODE 7 is described in order to have a broad overview of the mechanical principles of barrier resistance, and how there can be affected by corrosive processes.

The research conducted on the degradation of rockfall barriers started with the analysis of the current ISO standards, which define the corrosiveness of the environment and its classification based on the rate of corrosion that metal material samples develop over time, generally within a year. This parameter can be measured through specific on-site tests, but if these cannot be applied, ISO 9223:2018 provides a function called the "dose-response" method, through which it is possible, using site environmental parameters, to evaluate the corrosion rate of the main metallic materials.

The approach used to calculate the corrosion class of the environments surrounding the case studies is precisely the dose-response method. This led to the evaluation of two different corrosive classes: C2 for the case located far from the sea and C4 for the cases a few dozen meters from the sea.

The results obtained are in line with the case studies presented, considering that (BSI, 2012) gives this definition for C2 class: "Temperate zone, atmospheric environment with low pollution ( $\text{SO}_2 < 5 \mu\text{g}/\text{m}^3$ ), e.g. rural areas, small towns. Dry or cold zone, atmospheric environment with short time of wetness, e.g. deserts, subarctic areas." and for C4 class: "Temperate zone, atmospheric environment with high pollution ( $\text{SO}_2$ :  $30 \mu\text{g}/\text{m}^3$  to  $90 \mu\text{g}/\text{m}^3$ ) or substantial effect of chlorides, e.g. polluted urban areas, industrial areas, coastal areas without spray of salt water or, exposure to strong effect of de-icing salts. Subtropical and tropical zone, atmosphere with medium pollution".

The study cases presented are not strictly rockfall barriers, have similar components such as ropes and net fences, and are therefore subject to very similar corrosion processes, on which it is possible to base an analysis of rockfall barriers. As shown by the photographic documentation collected, the corrosive phenomena are much more intense on the elements installed along the coast, even reaching the point of damaging the nets. The corrosive aspect of the two cases is similar, which is due to a time delay of about 10 years in installation, thus highlighting how much more aggressive the coastal environment is, belonging to the C4 corrosion class.

Microsoft Excel proved to be a highly valuable tool for data visualization in this study. Its graphing and plotting functions allowed for a clear and efficient representation of the results obtained from the analyses conducted on the proposed case study. By generating detailed charts and comparative plots, Excel facilitated the interpretation of key parameters and trends, thereby enhancing the understanding of the system's performance and supporting the discussion of the thesis find.





# REFERENCES

- AASTHO, A. A. (2016). *Standard Specification for Zinc Coating (Hot-Dip) on Iron and Steel Hardware*.
- AASTHO, A. A. (2021). *Standard Specification Coatings of Zinc Mechanically Deposited on Iron and Steel*.
- Agliardi, F., & Crosta, G. B. (2003). A methodology for physically based rockfall hazard assessment. *Natural Hazards and Earth System Sciences*.
- Alejano, L. R., Veiga, M. P.-R., Castro-Filgueira, U., Arzua, J., & Castro-Caicedo, A. J. (2017). Analysis of a complex slope failure in a granodiorite quarry bench. *Bullettin of Engineering Geology and the Environment*, 78(2), 1209-1224.
- ARPA Puglia. (2023). *Dati qualità aria*. Retrieved from ARPA Puglia: <https://dati.puglia.it/ckan/dataset/dati-qualita-aria-2023/resource/0e63c4c7-79d4-4dc5-9443-76b6c650f124>
- Aven, T. (2015). *Risk analysis*. John Wiley & Sons.
- BSI. (2012, Febbraio 29). *Products*. Retrieved from BSI kknowledge: <https://knowledge.bsigroup.com/products/corrosion-of-metals-and-alloys-corrosivity-of-atmospheres-measurement-of-environmental-parameters-affecting-corrosivity-of-atmospheres>
- BSI. (2012, Febbraio 29). *Products*. Retrieved from BSI knowledge: <https://knowledge.bsigroup.com/products/corrosion-of-metals-and-alloys-corrosivity-of-atmospheres-guiding-values-for-the-corrosivity-categories>
- BSI. (2012, Febbraio 29). *Products*. Retrieved from BSI knowledge: <https://knowledge.bsigroup.com/products/corrosion-of-metals-and-alloys-corrosivity-of-atmospheres-classification-determination-and-estimation>
- BSI. (2012, Febbraio 29). *Products*. Retrieved from BSI knowledge: <https://knowledge.bsigroup.com/products/corrosion-of-metals-and-alloys-corrosivity-of-atmospheres-determination-of-corrosion-rate-of-standard-specimens-for-the-evaluation-of-corrosivity>
- BSI. (2015, May 31). *Products*. Retrieved from BSI Knowledge: <https://knowledge.bsigroup.com/products/corrosion-of-metals-and-alloys-corrosion-in-artificial-atmosphere-accelerated-corrosion-test-involving-exposure-under-controlled-conditions-of-humidity-cycling-and-intermittent-spraying-of-a-salt-solution>
- BSI. (2017, June 30). *Products*. Retrieved from BSI Knowledge: <https://knowledge.bsigroup.com/products/corrosion-tests-in-artificial-atmospheres-salt-spray-tests>
- Castanon-Jano, L., Blanco-Fernandez, E., Castro-Fresno, D., & Ballester-Munoz, F. (2017). Energy Dissipating Devices in Falling Rock Protection Barriers. *Rock Mechanics and Rock Engineering*, 50(3), 603-619.

- Catanzariti, F. (2016, 03 21). *Opere di difesa della caduta massi*. Retrieved from GeoStru: <https://www.geostru.eu/blog/2016/03/21/opere-di-difesa-della-caduta-massi-uni-11211-42012/?srsltid=AfmBOoqmT24kzkEPKON-0136mW2F6vkveN1jZW9lg9yDP5DGLndKILQu>
- Chuka, C., Odio, B., Chukwuneke, J., & Sinebe, J. (2014). Investigation of the effect of corrosion on mild steel in five different environments. *International journal of Scientific & Technology Research*, 3(7), 306-310.
- Chunlan, X., Zhiyong, Z., Chengqing, L., Huaxin, Z., & Shuai, T. (2022). Study on Numerical Model and Dynamic Response of Ring Net in Flexible Rockfall Barriers. *Sustainability*, 14(8), 4406.
- Corominas, J., Van Westen, C., Frattini, P., Fotopoulou, S., Catani, F., Van Den Eeckhaut, M., . . . Smith, J. (2014). Recommendations for the quantitative analysis of landslide risk. *Bulletin of engineering geology and the environment*, 73(2), 209-263.
- Cruden, D., & Varnes, D. (1996). Landslide types and processes. In D. Cruden, & D. Varnes, *Landslide, investigation and mitigation* (pp. 36-75).
- Deflorian, F., Rossi, S., Tancon, B., & Bonora, P. L. (2004). Corrosion behaviour of steel ropes for snow and rockfall barriers. *Corrosion engineering, science and technology*, 250-254.
- Di Sarno, L., Majidian, A., & Karagiannakis, G. (2021). The effect of atmospheric corrosion on steel structures: A state-of-the-art and case-study. *Builfings*, 11(12), 571.
- Dorren, L. (2003). A review of rockfall mechanics and modelling approaches. *Progress in Physical Geography. Progress in Physical Geography*, 27(1), 69-87.
- DYWIDAG. (2025, Gennatio 16). *Geotechnical Product Range*. Retrieved from DYWIDAG: <https://dywidag.com/downloads/geotechnical-product-range-us/en>
- EOTA. (n.d.). Retrieved from EOTA: <https://www.eota.eu/>
- EOTA. (2018). *EAD 340059-00-01106*. Brussels: European Organisation for Technical Assessment.
- Fanti, R. (2015). *I fenomeni franosi: descrizione e monitoraggio*. Appignano.
- Geobrugg. (n.d.). *Geobrugg*. Retrieved from Geobrugg: <https://www.geobrugg.com/>
- GEOPRODOTTI. (n.d.). *Caduta Massi*. Retrieved from GEOPRODOTTI: <https://www.geoprodotti.eu/categoria-campi-applicazione/protezione-caduta-massi/>
- Guerra, J., Castaneda, A., Corvo, F., Howland, J., & Rodriguez, j. (2019). Atmospheric corrosion of low carbon steel in a coastal zone of Ecuador: Anomalous behavior of chloride deposition versus distance from the sea. *Material and corrosion*, 70(3), 440-460.
- Güntel, B., & Acar, A. (2016, Ottobre 19). Rockfall Modelling with Remedial Design and Measures along Part of a Mountainous Settlement Area, Southern Turkey. *IOP Publishing*, 5. Retrieved from ResearchGate.
- Hoek, E., & Bray, J. (1981). *Rock Slope Engineering*. CRC press.

- Hungr, O., Leroueil, S., & Picarelli, L. (2014). The Varnes classification of landslide types, an update. *Landslides*, 11(2), 167-194.
- ilmeteo. (2025). *ilmeteo*. Retrieved from Archivio meteo: <https://www.ilmeteo.it/portale/archivio-meteo/Tricase/2024/Gennaio>
- Ingram, C. G., & Wagner, D. (2012). Cable Anchors versus Solid Bar Anchors in Rockfall Mitigation Systems. *63rd ANNUAL HIGHWAY GEOLOGY SYMPOSIUM*, (p. 10). California.
- Klinesmith, D. E., McCuen, R. H., & Abrecht, P. (2007). Effect of environmental conditions on corrosion rates. *Journal of Materials in Civil Engineering*, 19(2), 121-129.
- Koo, R., & J.S.H., K. (2014). A Numerical Study of Dynamic Responses of Two Selected Flexible Rockfall Barriers Subject to Punching and Areal Loads. *Technical Note No. TN*, 4, 15-30.
- Lecce, A. (2019). *Studio delle problematiche di caduta massi su una strada ad alta percorrenza e della durabilità delle opere di protezione*. Torino: Politecnico di Torino.
- Marchelli, M. (2000). Rockfall risk assessment. *Politecnico di Torino*, 15-60.
- Marchelli, M. (2000). Trajectory analysis. *Politecnico di Torino*, 46-130.
- Marchelli, M. (2020). *Net Fences: Technologies and design*. Torino: Politecnico di Torino.
- Matsuoka, N., & Sakai, H. (1998). Rockfall activity from an alpine cliff during thawing periods. *Geomorphology*, 28(3-4), 309-328.
- Meccaferri. (n.d.). *Rockfall Barrier*. Retrieved from Meccaferri: <https://www.maccaferri.com/products/rockfall-barriers/>
- meteoatlas. (n.d.). *Meteo Atlas Marina Serra*. Retrieved from Meteoatlas: [https://meteoatlas.it/italia/marina-serra-40886?utm\\_source=chatgpt.com](https://meteoatlas.it/italia/marina-serra-40886?utm_source=chatgpt.com)
- Meteoblue. (2025). *Meteoblue A Windy Company*. Retrieved from weatherarchive: [https://www.meteoblue.com/it/tempo/historyclimate/weatherarchive/marina-porto\\_italia\\_2524259](https://www.meteoblue.com/it/tempo/historyclimate/weatherarchive/marina-porto_italia_2524259)
- Panchenko, Y. M., Mashakov, A. I., Kundryavtseva, L. A., Kovtanyuk, V. V., & Nenasheva, T. A. (2025). A chloride deposition model for predicting the categories of atmospheric corrosivity in coastal areas. *Corrosion Engineering, Science and Technology*, 60(5), 376-389.
- Peila, D., & Ronco, C. (2009). Technical Note: Design of rockfall net fences and the new ETAG 027 European guideline. *Natural Hazards and Earth System Sciences*, 9(4), 1291-1298.
- Scavia, C., Barbero, M., Castelli, M., Marchelli, M., Peila, D., Torsello, G., & Vallero, G. (2020). Evaluating rockfall risk: Some critical aspects. *Geosciences*, 10(3), 98.
- Servizio Studi. (2025, Luglio 05). *Documentazione*. Retrieved from Camera dei deputati: [https://www.camera.it/temi/documentazione/temi/pdf/1385280.pdf?\\_1756111572822](https://www.camera.it/temi/documentazione/temi/pdf/1385280.pdf?_1756111572822)
- Suzumura, K., & Nakamura, S. I. (2004). Environmental factors affecting corrosion of galvanized steel wires. *Journal of materials in civil engineering*, 16(1), 1-7.

- Trumer Schutzbauten. (n.d.). *Rockfall standards ONR 24810*. Retrieved from Trumer Schutzbauten: <https://trumerschutzbauten.com/standards/rockfall-standards/onr-24810/>
- Ugazio, E. (2023). *Studio di sistemi di protezione contro la caduta massi e loro degrado durante la vita utile*.
- Unirock. (n.d.). *Opere di difesa caduta massi*. Retrieved from Unirock: <https://www.unirock.it/opera-di-difesa-caduta-massi>
- uu lifting. (n.d.). *how to use wire rope*. Retrieved from uu lifting: <https://www.uulifting.com/how-to-use-wire-rope-clips/>
- Vagnon, F., Bonetto, S., Ferrero, A. M., Harrison, J. P., & Umili, G. (2020). Eurocode 7 and Rock Engineering Design: The Case of Rockfall Protection Barriers. *Geosciences*, 10(8), 305.
- Varnes, D. (1978). Slope Movement Types and Processes. In D. Varnes, *Landslides: Analysis and Control* (p. 242). Transportation Research Board nel 1978.
- Varnes, D. (1984). *Landslide hazard zonation: a review of principles and practice*. United Nations Educational, Scientific and Cultural Organization.
- Volkwein, A., Roth, A., Gerber, W., & Aron, V. (2009). Flexible Rockfall Barrier Subjected to Extrem Loads. *Structural engineering international*, 19(3), 327-332.
- Volta, F. (2011). *Il ruolo delle barriere paramassi nella mitigazione del rischio da frana nella provincia autonoma di bolzano*.
- Xu, H., Cheng, Y., Zhao, L., Liu, Y., & Yu, Z. (2024). Experimental Study on Bearing Capacity Reduction of the Steel Wire-Rings in flexible barriers due to corrosion. *Construction and Building Materials*, 439.
- Zhang, D. X. (n.d.). *Zinc Coating Life Predictor*. Retrieved from American Galvanizers Association: <https://zclp.galvanizeit.org/>